Stony Brook University

Atomic substitutions in synthetic apatite;

insights from solid-state NMR spectroscopy

A Dissertation Presented

by

John S. Vaughn

to

The Graduate School

in Partial Fulfillment of the

Requirements

for the Degree of

Doctor of Philosophy

in

Geosciences

Stony Brook University

December 2016

Stony Brook University

The Graduate School

John S. Vaughn

We, the dissertation committee for the above candidate for the

Doctor of Philosophy degree, hereby recommend

acceptance of this dissertation.

Brian L. Phillips – Dissertation Advisor
Professor, Department of Geosciences

Hanna Nekvasil – Dissertation Advisor
Professor, Department of Geosciences

Joel Hurowitz – Chairperson of Defense
Assistant Professor, Department of Geosciences

John B. Parise
Distinguished Professor, Department of Geosciences

John Rakovan
Professor, Department of Geology & Environmental Earth Science, Miami University

This dissertation is accepted by the Graduate School

Nancy Goroff
Interim Dean of the Graduate School

Abstract of the Dissertation

Atomic substitutions in synthetic apatite;

insights from solid-state NMR spectroscopy

by

John S. Vaughn

Doctor of Philosophy

in

Geosciences

Stony Brook University

2016

Apatite, $Ca_5(PO_4)_3X$ (where X = F, Cl, or OH), is a unique mineral group capable of atomic substitutions for cations and anions of varied size and charge. Accommodation of differing substituents requires some kind of structural adaptation, e.g. new atomic positions, vacancies, or coupled substitutions. These structural adaptations often give rise to important physicochemical properties relevant to a range of scientific disciplines. Examples include volatile trapping during apatite crystallization, substitution for large radionuclides for long-term storage of nuclear fission waste, substitution for fluoride to improve acid resistivity in dental enamel composed dominantly of hydroxylapatite, and the development of novel biomaterials with enhanced biocompatibility. Despite the importance and ubiquity of atomic substitutions in apatite materials, many of the mechanisms by which these reactions occur are poorly understood. Presence of substituents at dilute concentration and occupancy of disordered atomic positions hinder

detection by bulk characterization methods such as X-ray diffraction (XRD) and infrared (IR) spectroscopy.

Solid-state nuclear magnetic resonance (NMR) spectroscopy is an isotope-specific structural characterization technique that does not require ordered atomic arrangements, and is therefore well suited to investigate atomic substitutions and structural adaptations in apatite. In the present work, solid-state NMR is utilized to investigate structural adaptations in three different types of apatite materials; a series of near-binary F,Cl apatite, carbonate-hydroxylapatite compositions prepared under various synthesis conditions, and a heat-treated hydroxylapatite enriched in ^{17}O. The results indicate that hydroxyl groups in low-H, near binary F,Cl apatite facilitate solid-solution between F and Cl via column reversals, which result in average hexagonal symmetry despite very dilute OH concentration (~2 mol percent). In addition, ^{19}F NMR spectra indicate that fluorine occupies a complex distribution of atomic positions, which give rise to complex ^{19}F peak shapes owing to varied F-Ca distance. ^{13}C NMR analysis of carbonate-hydroxylapatite indicates that AB-type carbonate hydroxylapatite can be prepared without the presence of sodium or heat treatment. Isotopic ^{17}O enrichment of hydroxylapatite and ^{17}O NMR analysis reveals distinct signals corresponding to phosphate and hydroxyl oxygens, and heat treatment under vacuum results in loss of hydroxyl signal due to decomposition to tricalcium phosphate, which was observed by powder X-Ray diffraction (PXRD).

Table of Contents

Chapter 1: Introduction 1
1.1 Motivation 1
1.2 NMR Interactions 2
1.2.1 Zeeman Interaction 2
1.2.2 Chemical Shielding 5
1.2.3 Heteronuclear Dipolar Coupling 8
1.2.4 Homonuclear Dipolar Coupling 10
1.2.5 The Quadrupolar Interaction 11
1.3 Experimental Aspects 15
1.3.1 Pulsed-Fourier Transform NMR 15
1.3.2 Vector Model and Single-Pulse (SP) NMR Experiments 15
1.3.3 Magic-Angle Spinning (MAS) 20
1.3.4 Cross-Polarization 21
1.3.5 Heteronuclear Correlation (HETCOR) 23
1.3.6 Rotational Echo Double Resonance (REDOR) 24

Chapter 2: Variation of carbonate substitution with synthesis conditions in Na-free carbonate hydroxylapatite 27
2.1 Abstract 27
2.2 Introduction 27
2.3 Materials and Methods 29
2.3.1 Apatite Synthesis 29
2.3.2 Chemical Analysis 30
2.3.3 Powder X-Ray Diffraction (PXRD) 31
2.3.4 Vibrational Spectroscopy 31
2.3.5 ^{1}H Single Pulse NMR 32
2.3.6 ^{31}P Single Pulse NMR 32
2.3.7 $^{13}C\{^{1}H\}$ Cross Polarization NMR 32
2.3.8 $^{1}H\{^{13}C\}$ REDOR NMR 33
2.3.9 $^{1}H\{^{31}P\}$ REDOR NMR 33
2.3 Results 34
2.4.1 Elemental Analysis 34
2.4.2 Powder X-Ray Diffraction (PXRD) 34
2.4.3 Vibrational Spectroscopy 37
2.4.4 ^{1}H Single Pulse NMR 41
2.4.5 ^{31}P Single Pulse NMR 43
2.4.6 $^{13}C\{^{1}H\}$ Cross Polarization NMR 47
2.4.7 $^{1}H\{^{13}C\}$ REDOR NMR 50
2.4.8 $^{1}H\{^{31}P\}$ REDOR NMR 59
2.5 Discussion 67
2.5.1 ^{1}H Assignments 67
2.5.2 A and B-type carbonate substitution 71
2.6 Conclusions 72

Chapter 3: Hydrogen Environments in Low-H, F,Cl Apatites Revealed by Double Resonance Solid-State NMR 73
3.1 Abstract 73

3.2 Introduction ... 73
3.3 Materials and Methods ... 76
3.3.1 Synthesis ... 76
3.3.2 Powder X-ray Diffraction (PXRD) ... 77
3.3.3 ^{1}H Single-Pulse (SP) MAS NMR Spectroscopy ... 77
3.3.4 $^{1}H\{^{31}P\}$ REDOR NMR Spectroscopy ... 78
3.4 Results ... 79
3.4.1 Powder X-ray Diffraction (PXRD) ... 79
3.4.2 ^{1}H Single-Pulse (SP) MAS NMR Spectroscopy ... 81
3.4.3 $^{1}H\{^{31}P\}$ REDOR NMR Spectroscopy ... 84
3.5 Discussion ... 89
3.5.1 Comparison of refined lattice parameters to previous efforts ... 89
3.5.2 Quantitative measurements of OH in apatite and the utility of ^{1}H NMR ... 90
3.5.3 OH structural environments in F,Cl Apatite ... 91
3.6 Conclusions ... 95

Chapter 4: Apatite solid-solution along the F,Cl binary investigated using multinuclear solid-state NMR methods ... 97
4.1 Abstract ... 97
4.2 Introduction ... 97
4.3 Materials and Methods ... 100
4.3.1 Apatite Synthesis ... 100
4.3.2 Solid-State NMR ... 101
4.4 Results ... 102
4.4.1 ^{31}P Single-Pulse (SP) MAS NMR Spectroscopy ... 102
4.4.2 ^{19}F SP MAS NMR Spectroscopy ... 105
4.4.3 $^{19}F\{^{35}Cl\}$ TRAPDOR NMR Spectroscopy ... 108
4.4.4 ^{35}Cl SP MAS NMR Spectroscopy ... 110
4.5 Discussion ... 113
4.5.1 Variation in phosphorus environments ... 113
4.5.2 On hydroxyl content and precautionary steps to minimize its concentration ... 114
4.5.3 Variation in fluorine environments ... 119
4.5.4 ^{35}Cl and ^{19}F Spectra of F90Cl10 ... 124
4.6 Conclusions and Future Work ... 124

Chapter 5: ^{17}O NMR spectroscopic investigation of the effect of heating hydroxylapatite ... 126
5.1 Abstract ... 126
5.2 Introduction ... 126
5.3 Materials and Methods ... 130
5.3.1 ^{17}O Enrichment ... 130
5.3.2 Heat Treatment of HAp (HAp-HT) ... 130
5.3.3 Powder X-Ray Diffraction (PXRD) ... 131
5.3.4 ^{17}O Single-Pulse (SP) MAS NMR ... 131
5.3.5 ^{31}P Single Pulse NMR ... 131
5.3.6 $^{1}H\{^{31}P\}$ REDOR NMR ... 132
5.4 Results ... 133
5.4.1 Powder X-Ray Diffraction (PXRD) ... 133
5.4.2 ^{17}O NMR Spectroscopy ... 136
5.4.3 ^{31}P NMR Spectroscopy ... 141

5.4.4 $^{1}H\{^{31}P\}$ REDOR NMR Spectroscopy *142*
5.5 Discussion 146
5.5.1 ^{17}O Enrichment *146*
5.5.2 Effect of Heat-Treatment on HAp *146*
5.5.3 Formation of Oxyapatite (OAp) *149*
5.5.4 Future work *149*
Chapter 6: Conclusions and future work 152
6.1 Concluding remarks 152
6.2 Future work 153
Chapter 8: References 155

List of Tables

Table 1: Larmor frequencies of commonly utilized nuclei 5
Table 2: Synthesis parameters and elemental analysis of 13CHAP samples 30
Table 3: Lebail refinement and fitting of the 002 reflection. [a]wt% CO_3 determined by linear correlation with *a* lattice parameter documented in LeGeros et al.[28] .. 35
Table 4: Approximation of carbonate content based on Raman spectra. (a) wt% carbonate determined using the method described by Krajewski et al.[31] 39
Table 5: Results of fitting ^{1}H single pulse NMR spectra 42
Table 6: Results of fitting ^{31}P NMR spectra 45
Table 7: Fitting results for $^{13}C\{^{1}H\}$ cross polarization NMR spectra 48
Table 8: Fiting results for $^{1}H\{^{13}C\}$ REDOR difference spectra 56
Table 9: Results of fitting $^{1}H\{^{31}P\}$ REDOR NMR spectra 64
Table 10: ^{1}H peak assignments from the current work 67
Table 11: Refined lattice parameters of F,Cl apatites. Uncertainties in parenthesis are for the last reported digit. (a) F50Cl50 composition used in Hughes et al., 2014.. 80
Table 12: Determination of OH component using ^{1}H NMR. (a) Ratio of total ^{1}H signal to sample mass in rotor. (b) Percentage of total ^{1}H signal due to apatitic ^{1}H, determined using $^{1}H\{^{31}P\}$ REDOR. Percentages are reported to the nearest integer to compensate for variation inherent to the experiment such as amplifier fluctuations and probe detuning. (c) Mole fraction OH component, determined using quantitative ^{1}H SP/MAS results and $^{1}H\{^{31}P\}$ REDOR. 85
Table 13: ^{1}H chemical shifts and peak widths for apatites determined via $^{1}H\{^{31}P\}$ REDOR difference spectroscopy 89
Table 14: ^{31}P NMR Parameters. Uncertainty in relative intensity obtained by fitting spectra thrice with minor adjustments to phasing. 103
Table 15: Results of fitting ^{19}F MAS NMR Spectra 106
Table 16: ^{35}Cl Chemical Shifts 110
Table 17: Simulated ^{35}Cl NMR parameters. 112
Table 18: ^{19}F Chemical shifts in the present work compared to a previous work 118
Table 19: M-F interatomic distances and ^{19}F chemical shifts of halite and fluorite-type metal fluorides. ^{19}F chemical shifts obtained from Kiczenski and Stebbins[70] and refs therein. 121
Table 20: Approximation of Ca2-F distances ^{19}F NMR results. Derivation of specific parameters explained in body of text 123
Table 21: Results of Lebail refinements for HAp before and after ^{17}O enrichment, Rietveld refinement of heat-treated HAp 135
Table 22: ^{17}O NMR Parameters reported by Pourpoint et al.[88] 139
Table 23: ^{31}P NMR Parameters 141
Table 24: $^{1}H\{^{31}P\}$ REDOR Results 144
Table 25: Intensity ratio of hydroxylapatite:background signal in S_0 spectra 149

List of Figures

Figure 1: Energy diagram for spin-1/2 nuclei 4
Figure 2: Effect of chemical shift anisotropy on the chemical shift. Schematic taken from [12] 6
Figure 3: Static powder lineshape due to chemical shift anisotropy. Taken from [13]. 7
Figure 4a) Pake double lineshape; b) origin of the doublet shape due to the anisotropy of the *I*-*S* internuclear vector. Taken from [12] 10
Figure 5: Nuclear spin states in the periodic table. Taken from [15]. 11
Figure 6: Static NMR lineshapes for nuclei with $I = 1$. Taken from [16] 13
Figure 7a: Energy level diagram of splittings due to quadrupolar coupling; b) static lineshape for $I=3/2$ nucleus with axially symmetric EFG ($\eta=0$). Both taken from [16] 14
Figure 8: Bulk magnetization at equilibrium. Taken from [17] 17
Figure 9: Application of 90° RF pulse to the bulk magnetization. Taken from nmr spectroscopy explained 18
Figure 10: Free-induction decay and Fourier transform. Taken from [17] 19
Figure 11: Illustration of the magic angle. Taken from [12] 20
Figure 12: The Cross-polarization (CP) experiment taken from the solid-state NMR page of Wikipedia 23
Figure 13: a) Acquisition of a typical 2D NMR experiment b) Indirect detection and FT to generate a contour plot. Taken from [12] 24
Figure 14: The REDOR pulse sequence 26
Figure 15: PXRD Results 35
Figure 16: Raman spectra of 13CHAP samples 38
Figure 17: FTIR Spectra of 13CHAP samples 39
Figure 18: ^{1}H single pulse (SP) NMR spectra 41
Figure 19: ^{31}P single pulse (SP) NMR spectra 44
Figure 20: $^{13}C\{^{1}H\}$ Cross-polarization NMR spectra 47
Figure 21: $^{1}H\{^{13}C\}$ REDOR spectral sets for 13CHAP-1.67 showing the spin echo (S_0), dephased (S) and difference spectra for dephasing times of a. τ = 1.5ms b. τ = 8ms and c. τ = 32ms 50
Figure 22: $^{1}H\{^{13}C\}$ REDOR spectral sets for 13CHAP-2.0 showing the spin echo (S_0), dephased (S) and difference spectra for dephasing times of a. τ = 1.5ms b. τ = 8ms and c. τ = 32ms 51
Figure 23: $^{1}H\{^{13}C\}$ REDOR spectral sets for 13CHAP-1.43 showing the spin echo (S_0), dephased (S) and difference spectra for dephasing times of a. τ = 1.5ms b. τ = 8ms and c. τ = 32ms 52
Figure 24: $^{1}H\{^{13}C\}$ REDOR spectral sets for 13CHAP-1.67(2x) showing the spin echo (S_0), dephased (S) and difference spectra for dephasing times of a. τ = 1.5ms b. τ = 8ms and c. τ = 32ms 53
Figure 25: $^{1}H\{^{13}C\}$ REDOR Difference NMR spectra for the CHAP samples taken with dephasing times (τ) as indicated on the right 55
Figure 26: $^{1}H\{^{13}C\}$ REDOR fraction plots of NMR signals 58

Figure 27: $^{1}H\{^{31}P\}$ REDOR spectral sets for 13CHAP-1.67 showing the spin echo (S_0), dephased (S) and difference spectra for dephasing times of a. τ = 8ms b. τ = 16ms and c. τ = 32ms 59
Figure 28: $^{1}H\{^{31}P\}$ REDOR spectral sets for 13CHAP-2.0 showing the spin echo (S_0), dephased (S) and difference spectra for dephasing times of a. τ = 8ms b. τ = 16ms and c. τ = 32ms 60
Figure 29: 1H{31P} REDOR spectral sets for 13CHAP-1.43 showing the spin echo (S_0), dephased (S) and difference spectra for dephasing times of a. τ = 8ms b. τ = 16ms and c. τ = 32ms 61
Figure 30: 1H{31P} REDOR spectral sets for 13CHAP-1.67(2x) showing the spin echo (S_0), dephased (S) and difference spectra for dephasing times of a. τ = 8ms b. τ = 16ms and c. τ = 32ms 62
Figure 31: $^{1}H\{^{31}P\}$ REDOR difference NMR spectra. Spectra are the same as those labeled S_0-S in figs. 27-30 63
Figure 32: $^{1}H\{^{31}P\}$ REDOR fraction plots of NMR signals 66
Figure 33: Variation in lattice parameters a and c as a function of chlorine content. Uncertainties are smaller than symbol size. 80
Figure 34: Variation in unit cell volume as a function of chlorine content. Uncertainties are smaller than symbol size. 81
Figure 35: Variation of unit cell volume with chlorine content for binary F,Cl apatites reported previously compared to that of the present study. 81
Figure 36: Background-corrected 1H Single-Pulse (SP) Spectra of F,Cl apatites. 83
Figure 37: $^{1}H\{^{31}P\}$ REDOR Results from F50Cl50. In black: Spin echo spectrum, showing all 1H. In red: REDOR difference spectrum, showing only 1H within a few Å of 31P. Asterisks denote spinning side bands (SSBs). 84
Figure 38: $^{1}H\{^{31}P\}$ REDOR Difference Spectra of F-Cl apatite samples, as indicated. Asterisks denote spinning side bands (SSBs). 87
Figure 39(a): Anion column reversal sequence proposed by Hughes et al. [49] and (b) Anion column reversal sequence modified to comport with $^{1}H\{^{31}P\}$ REDOR NMR results 95
Figure 40: ^{31}P SP NMR spectra of F,Cl apatites; 128 scans collected with a pulse delay of 30s 102
Figure 41a: ^{19}F SP MAS/NMR spectra of F,Cl apatites: collected using 600s pulse delays. Number of acquisitions varied for samples owing to the concentration of ^{19}F; 4 scans for F100 and F90Cl10, and 8, 16, and 32 scans for F67Cl33, F50Cl50, and F33Cl67, respectively. 148 scans collected for both F10Cl90 and the rotor blank. Fig 2b: The center band region of the ^{19}F NMR spectrum of F90Cl10 at expanded scale. Asterisks denote spinning side band positions (SSBs) 106
Figure 42: Plot ^{19}F chemical shifts vs. fluorine content for broadened F,Cl apatite compositions 107
Figure 43: $^{19}F\{^{35}Cl\}$ TRAPDOR NMR of F50Cl50. Spin echo spectrum shown in the upper spectrum, TRAPDOR difference spectrum shown below, scaled to facilitate comparison with the spin echo. 345 scans were collected at a spinning rate of 20kHz, using a 120s relaxation delay. 109

Figure 44: ^{35}Cl SP NMR Spectra of F,Cl Apatites. The pulse delay was 2s for all samples, and 170,000, 80,000, 44,000, 5000, 4000, and 3700 scans were collected for F90Cl10, F67Cl33, F50Cl50, F33Cl67, F10Cl90, and Cl100, respectively.... 110
Figure 45: Simulated ^{35}Cl SP NMR Spectra approximating F90Cl10 and the four compositions between F50Cl50 and Cl100 112
Figure 46: Plot of 1st ^{31}P spectral moment vs. fluorine content. Uncertainties obtained by fitting spectra thrice and calculating the range of spectral moments for each fit. 113
Figure 47: Plot ^{19}F chemical shifts vs. fluorine content..... 119
Figure 48: ^{19}F chemical shifts vs. M-F distance for halite and fluorite type metal fluorides 120
Figure 49: PXRD patterns of reagent-grade HAp shown in red, and after ^{17}O-enrichment, shown in black. Simulated spectrum from Hughes et al.[45] shown in blue.. 133
Figure 50: PXRD patterns of hydroxylapatite after heat treatment shown in black. In blue is a simulated hydroxylapatite pattern from Hughes et al.,[45] and in red is a simulated β-Tricalcium phosphate (TCP) pattern taken from Yashima et al.[92] 134
Figure 51: ^{17}O SP MAS NMR Spectra of HAp and HAp-HT. Spinning side-bands (SSBs) denoted with an asterisk. Background due to natural ^{17}O abundance in ZrO_2 rotors was determined by running a blank rotor under identical acquisition conditions. 136
Figure 52: Simulated ^{17}O NMR spectrum of HAp from parameters published in Pourpoint et al. 139
Figure 53: ^{31}P MAS NMR Spectra of HAp, ^{17}O enriched HAp, and heat-treated ^{17}O enriched HAp 141
Figure 54: S_0, S, and S_0-S spectra from the $^{1}H\{^{31}P\}$ REDOR experiment. a. HAp b. HAp ^{17}O enriched and c. HAp-HT ^{17}O enriched 143

Acknowledgments

I am tremendously grateful to both of my advisors, Profs. Brian L. Phillips and Hanna Nekvasil. Collection and interpretation of solid-state NMR spectra is very technical and challenging to new students, and Brian served as a very capable and patient instructor, slowly giving me more and more independence so that I was sufficiently challenged, but not overwhelmed. I am also grateful to Hanna for encouraging me and offering any possible assistance in the pursuit of my interests or career goals, despite the fact that I am not an experimental petrologist! She has been particularly helpful this last year, by making sure I was doing ok and involving me in discussion of literature in Brian's absence, and serving as a tremendous resource during my postdoc search.

I am also very thankful to Profs. Don Lindsley and John Parise, who were always happy to offer advice and were never bothered when I came knocking with questions. It is very apparent that they (and indeed all the Geosciences faculty) genuinely want to help graduate students and see them succeed.

I want to thank all the geograds and geopostdocs, for welcoming a chemist into their midst with open arms, and not laughing at me for my gaps in rudimentary geology knowledge. I have to also thank Mikee, Joe, Hyuck, and Erwin for being great friends in addition to great colleagues. I don't think I would've survived without their companionship and camaraderie.

Lastly, I have to thank my fiancé, Jessica, and my family who have been a tremendous source of motivation and encouragement.

Chapter 1: Introduction

1.1 Motivation

Apatite minerals are important to a number of fields such as petrology[1], geochronology[2], [3], biomineralization[4], and materials science[5]-[8]. Much of the interest in apatite is in developing relationships between physical or chemical behavior and the underlying mineral crystal structure. Examples of this include the viscosity and explosivity of magmas as a result of apatite volatile content in melts[9], using uranium and thorium substituents in apatite to date rocks[2], and understanding how changes in carbonate-containing hydroxyapatite and amorphous calcium phosphate phases affect the kinetics of biomineralization and the resultant resistance to chemical and physical attack[4], [10].

Owing to the importance of structure in determining the properties of apatite, a number of tools have been applied to determine the atomic arrangement. X-ray diffraction (XRD) is probably the most ubiquitous method to determine the positions of atoms in crystalline solids, however many of the important structural changes that occur in apatite phases are not well suited for analysis by XRD. Examples of such structural changes include minor substitutions or defect sites, poorly ordered atomic positions, or significant concentrations of light elements, such as H, which are difficult to detect owing to weak scattering. Solid-state NMR spectroscopy is well suited to identify structural environments that cannot be resolved via XRD such as those listed above, because it is inherently focused on a specific element rather than a structural average, and does not

require ordered atomic arrangements[11]. Solid-state NMR is then a viable method for characterizing the subtle structural changes found in apatite minerals that give rise to important physicochemical properties, and provides researchers with a tool for investigating atomic scale structure needed to understand the nature of this very important mineral.

The following dissertation describes the application of solid-state NMR to apatite of various compositions. Other analytical methods are employed where necessary, as it is recognized that solid-state NMR is only one tool in a suite of many used for comprehensive structural characterization. Chapter 2 discusses the application of solid-state NMR methods to investigate apatite compositions comparable to bone and dental enamel, specifically focusing on carbonate and the mechanisms of carbonate uptake in hydroxylapatite. Chapter 3 describes the role of hydroxyl groups in a suite of low-OH, near-binary F,Cl apatite compositions, using a quantitative method to determine hydroxyl content via ^{1}H solid-state NMR, and characterizing the orientation of these hydroxyl groups using a double resonance NMR method. Chapter 4 extends NMR analysis of F,Cl apatite materials using other NMR-active nuclei, such as ^{35}Cl, ^{31}P, and ^{19}F, to give a comprehensive picture of those atomic arrangements not coupled to OH groups. In Chapter 5 the possible conversion of hydroxylapatite into a long-proposed oxyapatite phase, $Ca_{10}(PO_4)_6(O^{2-},\square)$ is investigated using ^{17}O NMR spectroscopy.

1.2 NMR Interactions

1.2.1 Zeeman Interaction

The nuclear Zeeman interaction underlies the physical basis for observation of the NMR spectral signal. The nuclei of many atoms possess an intrinsic property known as

nuclear spin angular momentum, a quantum mechanical property so named because of its resemblance to the classical vector quantity of angular momentum. The nuclear spin angular momentum operator, $\hat{I}_z$, defines (in most cases) the largest interaction in NMR spectroscopy, the Zeeman interaction, shown in Equation 1:

$$\hat{H}_Z = -\gamma B_0 \hat{I}_z \quad (1)$$

Here, γ is the gyromagnetic ratio (rad•$s^{-1}T^{-1}$), which is different for any given type of nucleus (isotope), and B_0 is the magnitude of the external static magnetic field in T. Each of the possible eigenfunctions and eigenvalues for the $\hat{I}_z$ operator defines a possible energy level, and for any given nucleus there are $(2I + 1)$ energy levels, where I is the nuclear spin angular momentum quantum number. I can be a whole integer such as in ^{14}N ($I = 1$) or ^{10}B ($I = 3$) or a half-integer such as in ^{1}H ($I = ½$), ^{7}Li ($I = 3/2$), or ^{27}Al ($I = 5/2$). It follows that spin ½ nuclei have two possible energy levels, which is the fewest number possible. For the sake of simplicity the following discussion will focus only on spin-1/2 nuclei.

In the absence of an external magnetic field, both energy levels are degenerate, and equal populations of nuclei can be found in both states. In a magnetic field, however, the levels are no longer equal, which generates a slight difference in the distribution of spin populations. Spin-1/2 nuclei are commonly visualized as ‘spin up’ or ‘spin down’ where the spin directionality represents the orientation of the spin angular momentum with respect to the external magnetic field, shown in Figure 1. Assuming the magnetic field is pointing upwards (as is the convention), nuclei oriented in a ‘spin up’ configuration are aligned with the magnetic field and will be in a lower energy state, and

nuclei oriented in a 'spin down' configuration are opposed to the magnetic field and will be in a higher energy state.

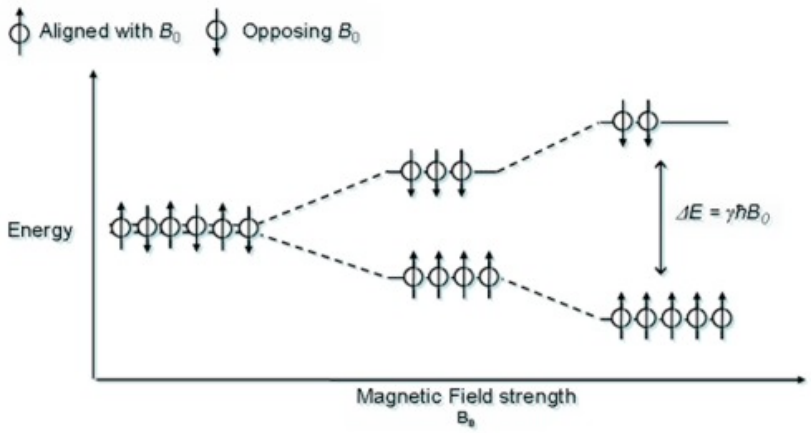

Figure 1: Energy diagram for spin-1/2 nuclei

The energy states (in Joules) for spin ½ nuclei are defined in Equation 2, γ is given in units of rad s^{-1} T^{-1}, and B_0 is in units of Tesla (T).

$$E_{+½} = -\gamma\hbar B_0(½) \qquad E_{-½} = -\gamma\hbar B_0(-½) \tag{2}$$

Nuclei in the lower energy state can absorb electromagnetic radiation of equal magnitude to the gap between the two energy levels, and enter the high-energy state. This transition and the resultant relaxation back to the equilibrium spin population distribution is the essence of NMR spectroscopy. The spin populations in both states are governed by a Boltzmann distribution, which at ambient temperature can be approximated as shown in Equation 3.

$$\Delta N = N_{total} \cdot \frac{\hbar^2 \gamma^2 B_0}{2kT} \tag{3}$$

The energy at which this transition occurs is called the Larmor frequency (ν_0 in Hz, ω_0 in rad s^{-1}), and occurs in the radio frequency (RF) range of the electromagnetic spectrum for typical commercial spectrometers. A simple derivation of the Larmor frequency is shown in Equation 4. The Larmor frequency at any given value of B_0 is

unique to every nucleus, and varies linearly with the strength of the static magnetic field. Larmor frequencies at 9.4T for several commonly studied nuclei are shown in Table 1.

$$\begin{aligned}\Delta E(J) &= \gamma\hbar B_0(\tfrac{1}{2}) - \gamma\hbar B_0(-\tfrac{1}{2}) \\ &= \gamma\hbar B_0 \\ &= \omega_0 \text{ (rad s}^{-1}\text{)} \\ &= \nu_0 \text{ (Hz)}\end{aligned} \quad (4)$$

Nucleus	Larmor Freq. (MHz) $B_0 = 9.4T$
^{1}H	399.994
^{19}F	376.376
^{31}P	161.923
^{27}Al	104.227
^{13}C	100.580

Table 1: Larmor frequencies of commonly utilized nuclei

1.2.2 Chemical Shielding

In addition to the nucleus, electrons also respond to the presence of the magnetic field B_0, generating weaker localized magnetic fields. These localized magnetic fields modify the magnitude of B_0 felt by the nucleus, which will modify the energy gap between spin populations, and the resonance frequency. Despite the fact that the magnitude of the shielding effect is only about $1/10^6$ that of the Zeeman interaction, it is probably the most important NMR interaction because it provides insight into the chemical and electronic environment of a given nucleus and resolution between distinct sites and/or structural/chemical environments.

If the electron cloud, and more specifically the magnetic field generated due to the electron cloud, were spherical in shape, then the shielding effect would be isotropic, and independent of molecular orientation relative to B_0. The magnetic fields generated from

electrons rarely exhibit such symmetrytt, however, and as a result the magnitude of the observed shielding effect is anisotropic. This anisotropic shielding is called the chemical shift anisotropy (CSA), which as a rank-2 tensor that can be represented by an ellipsoid. This is clearly illustrated in Figure 2, taken from [12]. The smallest chemical shift is observed in Figure 2a, where the smallest axis of the CSA tensor is oriented along B_0. The largest chemical shift is observed when the largest CSA tensor axis is oriented along B_0, shown in Figure 2c, and an intermediate shift is observed for any other orientation.

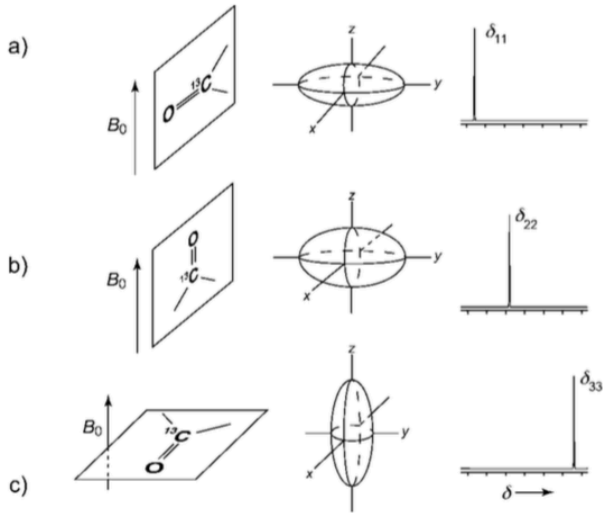

Figure 2: Effect of chemical shift anisotropy on the chemical shift. Schematic taken from [12]

Almost all solid-state NMR experiments involve the use of powdered solids, where all molecular orientations are present. The near-infinite number of molecular orientations inherent to powders gives rise not only to the three NMR peaks observed when B_0 is oriented along the three principal axes as shown in Figure 2, but an infinite number of peaks corresponding to orientations in between the three principal orientations. The observed effect is a very broad, asymmetric peak, comprised of a sum of resonances for all possible configurations and molecular orientations, shown in Figure 3.

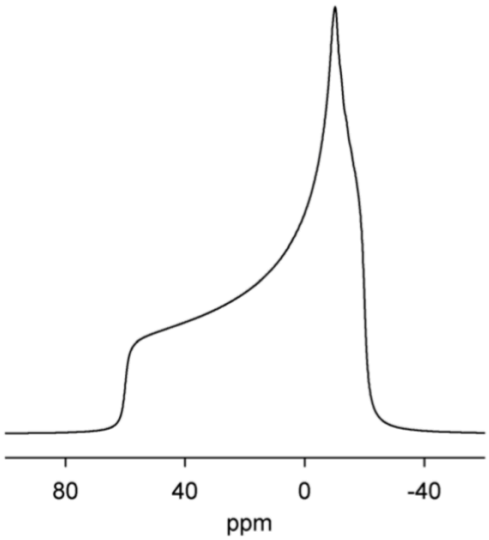

Figure 3: Static powder lineshape due to chemical shift anisotropy. Taken from [13].

The shape of the electron cloud around the nucleus, and hence the magnitude of the chemical shift anisotropy is an ellipsoid, and can be represented by a 3 X 3 matrix that is symnmetric and trace-invariant and can therefore be diagonalized, representing the principal axis frame.

$$\sigma_{CS} = \begin{bmatrix} \sigma_{11} & & \\ & \sigma_{22} & \\ & & \sigma_{33} \end{bmatrix} \quad (5)$$

Here, the matrix representation is shown where the principal components of the ellipsoid are aligned along the CSA principal coordinate axes, as depicted in Figure 2. The overall effect of the chemical shielding is shown in the expression of the Hamiltonian in Equation 6.

$$\hat{H}_{cs} = \gamma \hat{I} \bullet \sigma_{CS} \bullet B_0 \quad (6)$$

By assuming that the ellipsoid describing the chemical shift anisotropy is axially symmetric, that is $\sigma_{11} = \sigma_{22}$, the Hamiltonian describing chemical shielding can be split into an isotropic part and an anisotropic part, shown in Equation 7, where $\sigma_{iso} = 1/3(\sigma_{11} +$

$\sigma_{22} + \sigma_{33}$), $\sigma_{CSA} = \sigma_{33} - \sigma_{iso}$, and θ is the angle between the longitudinal axis of the ellipsoid and B_0.

$$\hat{H}_{cs} = \gamma \hat{I}_z B_0[\sigma_{iso} + \tfrac{1}{2}\sigma_{CSA}(3\cos^2\theta - 1)] \quad (7)$$

1.2.3 Heteronuclear Dipolar Coupling

Just as the magnetic fields of electrons can modify the frequency of the NMR transition, this transition also depends on the spin states of the nearby (< 10Å) nuclei[12]. For unlike nuclei the magnitude of this effect is expressed in the heteronuclear dipolar coupling Hamiltonian shown in Equation 8. The term *d* represents the dipolar coupling constant, shown in Equation 9. $\hat{I}_z$ is the z-component of the angular momentum operator for the *I*-spin (observed), and $\hat{S}_z$ is the z-component of the angular momentum operator for the *S*-spin.

$$\hat{H}_{IS} = -d(3\cos^2\theta - 1)\, \hat{I}_z \hat{S}_z \quad (8)$$

$$d = \left(\frac{\mu_0}{4\pi}\right)\frac{\hbar \gamma_I \gamma_S}{r_{IS}^3} \quad (9)$$

In Equation 9, μ_0 is the permittivity of free space (4π x 10^{-7} N A^{-2}), γ_I and γ_S are the gyromagnetic ratios of the *I* and *S* spins respectively and r_{IS} is the interatomic distance between the *I* and *S* nuclei. There are three important points regarding the effects of heteronuclear dipolar coupling on solid-state NMR spectroscopy: first, the magnitude of dipolar coupling is dependent on the gyromagnetic ratios of both *I* and *S* spins. This means that the dipolar coupling interaction between nuclei with large gyromagnetic ratios such as ^{1}H and ^{19}F is much greater than that between lower-γ nuclei, such as ^{17}O and ^{35}Cl. This result makes some intuitive sense, as it is expected that nuclei with stronger

magnetic moments would interact more strongly and at greater distance than nuclei with weaker magnetic moments. Second, the coupling is dependent on the inverse cube of the interatomic distance, which means that the magnitude of this effect drops off dramatically as the interatomic distance between *I* and *S* nuclei increases. Thirdly, the magnitude of the dipolar coupling interaction depends on orientation of the internuclear vector between the *I* and *S* nuclei with respect to the magnetic field B_0. This orientation dependence has important implications for the static NMR lineshape, similar to that observed as a result of chemical shielding anisotropy shown in Figure 3 in section 1.2.2. The resultant lineshape from heteronuclear dipolar coupling is called a Pake doublet, so named because it is composite of two distinct lineshapes [14]. The Pake doublet shape is shown in Figure 4a, and the lineshapes that give rise to the doublet are shown in Figure 4b. To determine the origin of the Pake doublet it is best to consider the individual contributions to the lineshape independently. The low intensity shoulder observed is due to those *I*-*S* spin pairs whose internuclear vectors are oriented parallel to the magnetic field, and the sharp peak is due to spin pairs whose internuclear vectors are oriented perpendicular to the magnetic field. This shape is due to an *I* spin coupled to an *S* spin, which is for the sake of argument, in a 'spin up' configuration. To achieve the other doublet, simply consider an isolated *I*-*S* spin pair as before, but with the *S* spin in the 'spin down' configuration. This gives rise to a mirror image of the initial lineshape, and the overlap of both lineshapes results in the doublet.

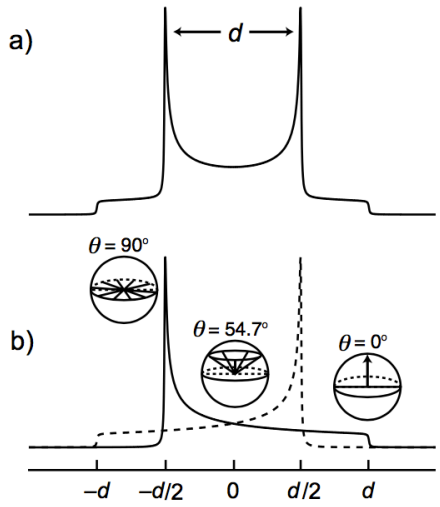

Figure 4a) Pake double lineshape; b) origin of the doublet shape due to the anisotropy of the *I-S* internuclear vector. Taken from [12]

1.2.4 Homonuclear Dipolar Coupling

In section 1.2.3 it was illustrated that localized magnetic fields produced by *different* nuclei can interact with one another, and that this has an impact on resultant NMR spectra. Similarly, identical nuclei can also experience dipolar coupling, and much of the mathematical treatment given to heteronuclear dipolar coupling applies in the homonuclear case. The main difference is the addition of the $\boldsymbol{I}_1 \bullet \boldsymbol{I}_2$ term into the dipolar coupling Hamiltonian:

$$\hat{H}_{II} = -d(1/2)(3\cos^2\theta - 1)(3\hat{I}_{1z}\hat{I}_{2z} - (I_1 \bullet I_2)) \quad (10)$$

It is clearer to write the $\boldsymbol{I}_1 \bullet \boldsymbol{I}_2$ term ($= \hat{I}_{1x}\hat{I}_{2x} + \hat{I}_{1y}\hat{I}_{2y} + \hat{I}_{1z}\hat{I}_{2z}$) in terms of raising and lowering operators, shown in Equation 11, which give Equation 12.

$$I^+ = I_x + iI_y \; ; \; I^- = I_x - iI_y \quad (11)$$

$$\hat{H}_{II} = -d(1/2)(3\cos^2\theta - 1)(2\hat{I}_{1z}\hat{I}_{2z} - \tfrac{1}{2}(I_1^+ I_2^- + I_1^- I_2^+)) \quad (12)$$

The physical significance of the raising and lowering operators in this context is that of a spin flip; a raising operator will change a spin up configuration to a spin down, and the converse is true of a lowering operator. The meaning of the $I_1^+I_2^-$ and $I_1^-I_2^+$ terms indicates that energy of coupled spin flips between the I_1 and I_2 spins occurs conservatively, giving rise to spin diffusion.

1.2.5 The Quadrupolar Interaction

This dissertation deals sparsely in solid-state NMR spectroscopy of quadrupolar nuclei (nuclei with $I > ½$), however given the ubiquity of quadrupolar nuclei across the periodic table (Figure 5) and their importance in analysis specifically of inorganic solids, a brief description is provided here.

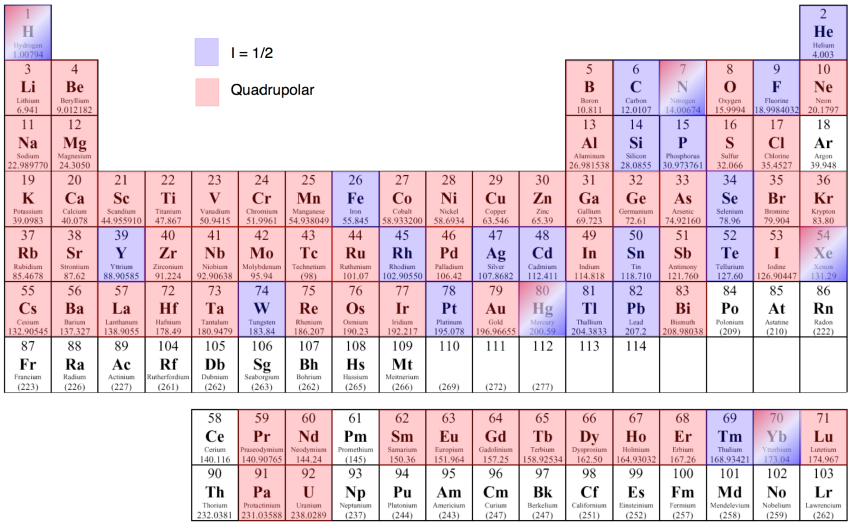

Figure 5: Nuclear spin states in the periodic table. Taken from [15].

It was mentioned in the discussion of the Zeeman interaction that for a given nucleus of spin I there are $(2I + 1)$ possible energy states, which for nuclei with $I = ½$ gives two possible energy states and a single NMR transition. For quadrupolar nuclei ($I > ½$) however, there are >2 possible energy states, and in turn multiple possible NMR

transitions. Quadrupolar nuclei posses a quadrupole moment, capable of strong interaction with the electric field gradient at the nucleus, which in addition to giving very broad NMR lineshapes also changes the way in which nuclei respond to radiofrequency (RF) radiation used in the NMR experiment. The magnitude of quadrupolar coupling is typically described using two parameters; a quadrupolar coupling constant χ, shown in Equation 13 and an asymmetry parameter η, defined in Equation 14.

$$\chi = (e^2qQ)/h \qquad (13)$$

The quadrupolar moment here is eQ, where e is the elementary charge ($1.6\text{x}10^{-19}$ C) and Q is an area term (typically in millibarn, 1mb = 10^{-31} m^2) intrinsic to each type of nucleus (isotope). To describe the interaction of the quadrupolar moment with the electric field gradient, the largest component of the EFG tensor (V_{zz}) is used, and in Equation 13 has the form eq. The h term in Equation 13 is simply Plank's constant. The resultant coupling constant has units of Hz. It is important to point out that unlike in the case of the chemical shift and dipolar coupling, the magnetic field B_0 is not a part of the coupling equation. This is because quadrupolar coupling is an *electric* coupling between the electric quadrupolar moment of the nucleus and the surrounding electric field gradient.

$$\eta = (V_{xx} - V_{yy})/V_{zz} \qquad (14)$$

The parameter η (Equation 14) describes the asymmetry of the electric field gradient around the nucleus, and can vary from $0 < \eta < 1$. Because of the significant dependence of the magnitude of quadrupolar coupling on the geometry of the electronic environment surround the nucleus, determination of χ and η can be of significant help in structure studies of materials containing quadrupolar nuclei. For example, for nuclei with

cubic point symmetry $\chi = 0$, and for nuclei with C_3 or higher rotational point symmetry, $\eta = 0$.

The static NMR lineshapes for a quadrupolar nucleus with $I = 1$ are shown in Figure 6. The top most spectrum ($\eta = 0.0$) shows a spectrum similar to a Pake doublet, and the lineshapes begin to deviate from the Pake lineshape as the asymmetry parameter is increased. The doublet shape is due in the $I = 1$ case to the two NMR transitions that are observed.

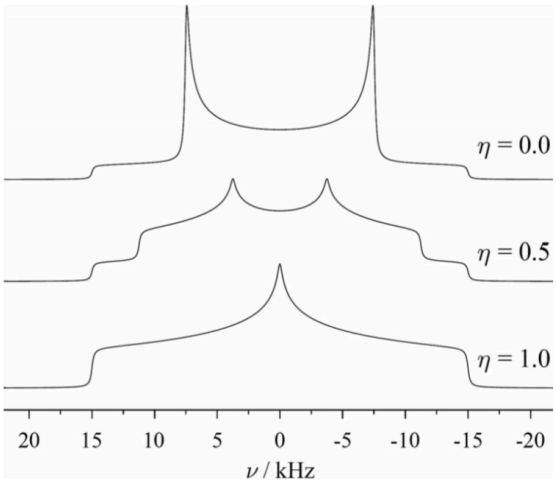

Figure 6: Static NMR lineshapes for nuclei with $I = 1$. Taken from [16]

The static powder NMR lineshape for $I = 3/2$ is similar to a Pake doublet, however because there are 3 possible NMR transitions, a third central signal is observed in the middle of the doublet pattern, shown in Figure 7b. The central (½ , -½) transition (CT) is narrow because it is not affected by the quadrupolar interaction to first order. This is shown schematically in Figure 7a: the energy level splittings above $\mathcal{H}_Z$ are those due to the normal Zeeman interaction, and those due to the quadrupolar interaction to first order are shown above $\mathcal{H}_Q^{(1)}$

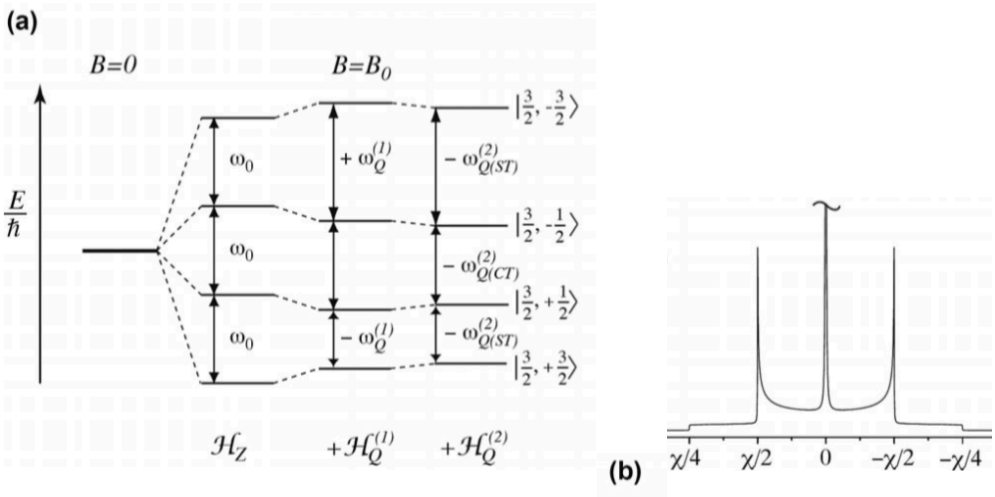

Figure 7a: Energy level diagram of splittings due to quadrupolar coupling; b) static lineshape for *I*=3/2 nucleus with axially symmetric EFG (η=0). Both taken from [16]

In most cases, the quadrupolar interaction is quite large (several MHz) and for low-γ nuclei this interaction can be comparable to the Larmor frequency. In such cases the quadrupolar interaction can no longer be treated as a first-order perturbation of the Zeeman, and second order corrections must be considered. Where first order corrections of the quadrupolar interaction do not affect the CT, second order quadrupolar coupling does effect the position of the central transition, given by Equation 15, where υ_0 is the Larmor frequency, and the coefficients *A, B* and *C* describe the dependence of the CT lineshape on θ.

$$\nu^{(2)}_{-1/2,+1/2} = -\frac{9\chi^2}{6\nu_0[2I(2I-1)]}[I(I+1)-\frac{3}{4}\bullet(A\cos^4\beta + B\cos^2\beta + C) \qquad (15)$$

The modification of the CT is demonstrated schematically in Figure 7a, in the energy diagram above $\mathcal{H}^{(2)}_Q$. In the case of 2nd order quadrupolar coupling, the CT lineshape is affected only by the 2nd order quadrupolar lineshape, and the satellite transitions are affected by both first and second-order coupling. It's worth noting that the

2^{nd} order quadrupolar effect is reduced as the Larmor frequency is increased (ν_0 in Equation 15); therefore it is advantageous to utilize high field strength NMR spectrometers when dealing with materials that exhibit strong quadrupolar coupling.

1.3 Experimental Aspects

1.3.1 Pulsed-Fourier Transform NMR

Typical collection of spectroscopic data involves applying continuous wave radiation sweeping over a specific spectral range, and indeed early NMR spectra were collected in such a fashion. However it was later realized that because of the weak nature of magnetic spin interactions, a broad range of frequencies could be excited uniformly by application of a powerful short pulse, recording the response in the time domain, followed by Fourier transform to obtain the spectrum in the frequency domain. This technique greatly reduced the time required to obtain an NMR spectrum, as a broad spectral range could be probed simultaneously, instead of a spectral sweep of frequencies.

1.3.2 Vector Model and Single-Pulse (SP) NMR Experiments

To understand the physical basis of recording NMR spectra it is helpful to visualize the behavior of large populations of spins in terms of classical phenomena. The vector model is one such visualization tool, and treats the net magnetization of an ensemble of spins as a single vector. The manipulations of this vector due to the application of RF pulses provide somewhat intuitive explanations for much of what is observed in NMR spectroscopy. Indeed the vector model is a powerful visualization technique, applicable not only to straightforward single pulse (SP) NMR experiments, but

also cross-polarization (CP) and spin-echo experiments. It should be emphasized though, that the vector model is simply a visualization tool, and that the various manipulations are not representative of actual spin behavior. It is simply a classical means to describe quantum mechanical phenomena involving a large ensemble.

If we assume that all nuclei in a sample are spinning in the classical sense, then consequently there is an angular momentum force orthogonal to the direction of spin. The static magnetic field B_0 exerts a torque on this angular momentum vector, the result of which is precession of the angular momentum vector about the static field, at a rate equal to the Larmor frequency. The classical analogy here is the motion of a gyroscope against the force of gravity. Although the population of spins is precessing at the same rate, they are out-of-phase, which is to say that coordinates in the transverse plane perpendicular to B_0 of each angular momentum vector due to each spinning nucleus are slightly offset. This is shown schematically in Figure 8a, where the arrows represent individual angular momentum vectors, and the direction of the arrows are indicative of the spin state (up or down, α or β, governed by the Boltzmann distribution shown in Equation 3).

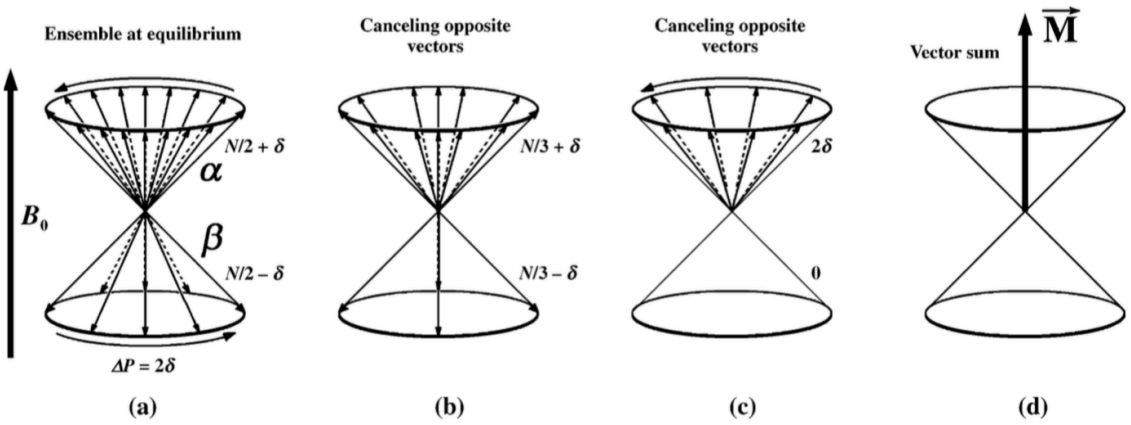

Figure 8: Bulk magnetization at equilibrium. Taken from [17]

Shown in stepwise fashion in Figure 8b and c is the vector sum of all angular momentum contributions, in which the downward pointing vectors and the *x* and *y* components of angular momentum are eliminated, leaving the positive *z*-component, shown in Figure 8d. This vector sum is considered the bulk magnetization. By applying transverse RF pulses along the *x*-axis at or near the Larmor frequency, it is possible to manipulate the orientation of the bulk magnetization vector. While the pulse (typically on the order of several μs) is applied, there is an oscillating current inside the NMR probe coil surrounding the sample, which generates a localized oscillating magnetic field. The effect of this transverse field is to apply a torque $\vec{T} = \vec{M} \times B_1$, which rotates the bulk magnetization away from the *z* direction, and into the *y* plane. The strength of this transverse field, called B_1, is typically reported in units of kHz ($\nu_1 = \gamma B_1 / 2\pi$), and is the inverse of the time required for the bulk magnetization to complete a full revolution. For example, if it takes 20 μs to complete a full revolution, then the strength of the B_1 field would be ($1 / 2 \times 10^{-5}$s) = 50,000 Hz or 50 kHz. NMR signal is only generated if a component of $\vec{M}$ lies in the *x* and *y* plane, so optimal signal is observed when the bulk magnetization is exactly in the *x y* plane, 90° away from the direction of B_0, shown in

Figure 9. In the case of the 50 kHz B_1 field, a 90° pulse (π/2 in radians) would be one-quarter of that required to complete a full revolution, which at 50 kHz would be 5 µs.

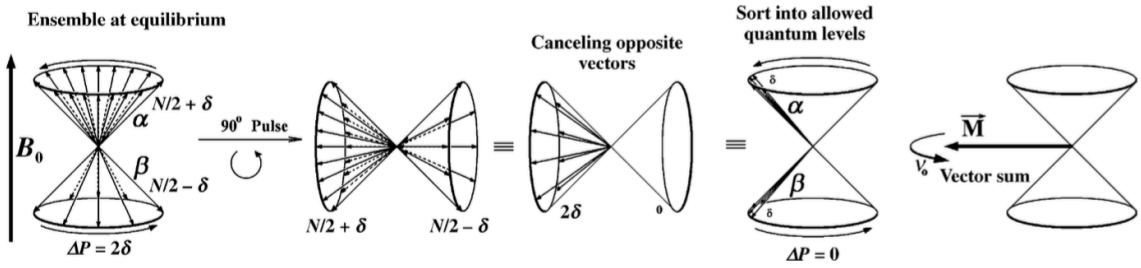

Figure 9: Application of 90° RF pulse to the bulk magnetization. Taken from nmr spectroscopy explained

The most commonly performed NMR experiment is the single pulse experiment; which involves application of a pulse (typically 90° but often shorter) and observation of the resultant free-induction decay (FID) due to the induced voltage in the sample coil as the bulk magnetization vector precesses in the *x*-*y* plane. The period of phase coherence of the bulk magnetization is finite; slowly the individual spins begin to 'fan out' as observed at equilibrium due to small frequency differences, arising from slightly varying chemical or magnetic environments. The observed result of this de-phasing is an exponential decay represented by Equation 16, where $M_{(t)}$ is the magnetization at time t, M_0 is the initial magnetization, t is time (usually in seconds), and T_2^* is the transverse relaxation time constant (also in seconds).

$$M_{(t)} = M_0 e^{-t/T_2} \qquad (16)$$

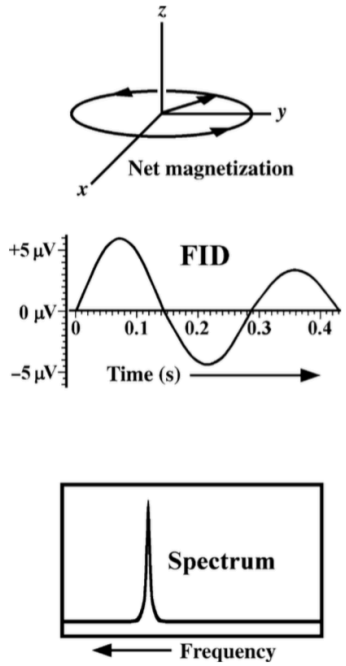

Figure 10: Free-induction decay and Fourier transform. Taken from [17]

Figure 10 demonstrates the relationship between the precession of the bulk magnetization in the *x*-*y* plane and the FID, and then how Fourier transform of the FID results in a NMR spectrum. In addition to the 'fanning out' of the bulk magnetization in the *x*-*y* plane *via* T_2 processes there is also spin-lattice (T_1) relaxation back to the equilibrium distribution of spins about B_0 governed by the Boltzmann distribution, in which a slight abundance of spins are oriented parallel to the magnetic field. Although this process is also exponential, the rate of relaxation is typically much slower in solids, owing to their reduced rotational and vibrational motion. For I= ½ nuclei in well-ordered solids T_1 can be on the order of several minutes. In Equation 17, the time constant governing this mechanism of relaxation is T_1. The magnitude of T_1 dictates delay required between successive acquisitions to allow for re-establishment of a substantial proportion of the equilibrium magnetization (M_0).

$$M_{(t)} = M_0 e^{-t/T_1} \qquad (17)$$

1.3.3 Magic-Angle Spinning (MAS)

The Hamiltonians for the 1st order quadrupolar moment, chemical shielding anisotropy in Equation 7, heteronuclear dipolar coupling in Equation 8, and the homonuclear dipolar coupling in Equation 10 all depend on the $3\cos^2\theta-1$ term, where θ is the angle between the internuclear vector (in the case of dipolar coupling) and B_0, or the angle between the long axis of the chemical shielding tensor and B_0. The term $3\cos^2\theta-1$ is zero when $\theta = 54.74°$, which is also the angle between the body diagonal and edge of a cube shown in Figure 11.

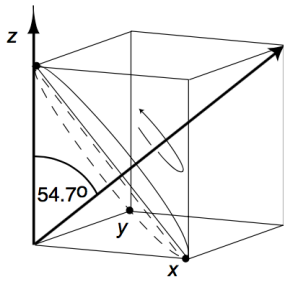

Figure 11: Illustration of the magic angle. Taken from [12]

For polycrystalline powder samples, alignment along the magic angle is insufficient to eliminate broadening due to shielding anisotropy and dipolar coupling, as only a small fraction of chemical shift tensors and internuclear vectors are aligned at the magic angle. By spinning the sample rapidly about the magic angle, the *average* angle for each internuclear vector in the powder sample over one rotor period aligns along the magic angle, and the *average* chemical shielding tensor will be axially symmetric and the long axis aligns with the magic angle. The NMR lineshapes are free from heteronuclear dipolar coupling and chemical shift anisotropy. Depending on the magnitude of these interactions, and the magic-angle spinning (MAS) rate, a series of peaks will appear on

either side of the resonance that trace out the shape of the static NMR signal, called spinning side bands (SSBs). In the case of low-γ nuclei, the homonuclear dipolar coupling can also be completely averaged by standard MAS methods. For abundant nuclei with large γ such as ^{1}H, the large magnitude of homonuclear dipolar coupling cannot be completely averaged even by very fast MAS (~60 kHz), and the central signal remains broadened.

1.3.4 Cross-Polarization

A key difference between solid-state and liquid state NMR spectroscopy is the ubiquity of ^{1}H NMR. Molecular tumbling in liquids provides complete averaging of homonuclear dipolar coupling, which gives rise to narrow, useful NMR signals. As mentioned in the previous section, typical ^{1}H homonuclear dipolar coupling cannot be completely averaged by MAS, therefore solid-state NMR spectroscopists often turn to lower--γ nuclei such as ^{13}C, or ^{31}P for spectroscopic study. Analysis of these nuclei however is plagued by poor sensitivity from the low γ, and also typically long T_1 values that greatly extend the acquisition time required in order to obtain useable signal. The cross-polarization experiment provides a means to mitigate these problems, by utilizing the high polarization and short relaxation time of high γ nuclei and the resolution afforded by low γ nuclei. The cross-polarization (CP/MAS) experiment involves the transfer of polarization from one abundant nucleus (typically ^{1}H) to a sparse nucleus, thereby enhancing the signal of the sparse nucleus. The mechanism is analogous to energy-conservative spin diffusion observed in homonuclear dipolar coupling, however in the case of the CP experiment the energy required to induce polarization transfer is provided by applied B_1 fields. Shown in Figure 12 is the CP pulse sequence; first a 90° pulse is

applied to ^{1}H, after which a phase-change aligns the ^{1}H B_1 field marallel to M_H while a spin-lock, or contact pulse is applied to the X nuclei (e.g. ^{13}C), shown in the gray boxes labeled 1 and 2. During the spin-lock period polarization is transferred from the abundant spin (^{1}H in this case) to the sparse spin (^{13}C in this case). In order for polarization transfer to occur the Hartmann Hahn match condition must be satisfied, which dictates that the precession rates of both nuclei due to their respective B_1 fields are equal, i.e. $\gamma_I B_{1,I} = \gamma_S B_{1,S}$. The irradiation applied to ^{1}H after the contact pulse (decoupling) minimizes broadening due to ^{1}H-^{13}C heteronuclear dipolar coupling during acquisition of the ^{13}C FID. Because polarization transfer in the CP experiment proceeds via heteronuclear dipolar coupling, the rate of transfer depends not only on the gyromagnetic ratios of both nuclei, but also the distance between the *I* and *S* nuclei (see Equation 9). As a result, for two isolated *I*-*S* spin pairs, the relative contributions to the NMR shape will change as a function of contact time; *I*-*S* pairs with short interatomic distances will dominate at shorter contact time, and those with greater interatomic distances will become apparent at longer contact time. Decay of the ^{1}H transverse magnetization during the contact pulse also must be considered in CP kinetics calculations, with decay constant $T_{1\rho}$.

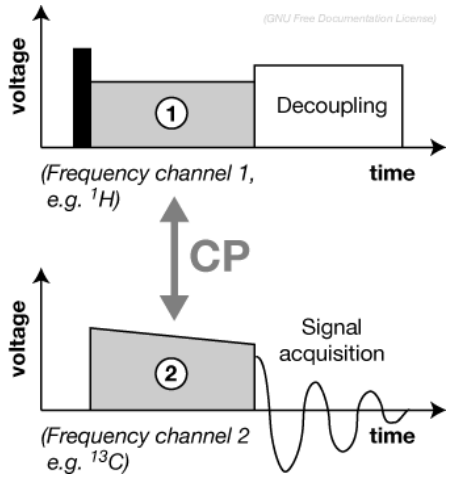

Figure 12: The Cross-polarization (CP) experiment taken from the solid-state NMR page of Wikipedia

1.3.5 Heteronuclear Correlation (HETCOR)

There are many instances in which simple modulation of the contact time in CP experiments fails to provide the requisite structural information regarding *I-S* spin pairs. In this case heteronuclear correlation spectroscopy (HETCOR) can elucidate more closely related *I-S* spin pairs *via* a two dimensional NMR method. Figure 13 illustrates some important facets of the HETCOR experiment. A 'prepare' pulse is applied to the indirectly detected spin (typically ^{1}H), after which the ^{1}H spin polarization is transferred to the directly detected spin via CP, represented by the 'mix' pulse, and lastly the signal is detected, conventionally during t_2. The next iteration of the HETCOR experiment involves incrementing an inter-pulse delay, or evolution time (t_1 in Figure 13a), in between the 'prepare' and 'mix' pulses. During the evolution time, the ^{1}H spins evolve under their own chemical shifts before polarization transfer, effectively detecting the spectrum of ^{1}H indirectly *via* another nucleus. Indirectly-detected FIDs are obtained by collecting a series of FIDs with varied incremental evolution time, and using the first point in each subsequent FID to generate another spectrum. This is illustrated in Figure 13b. By taking the Fourier transform of both the directly detected and indirectly detected

FIDs, the 2-dimensional plot can be represented as a contour plot. In this contour plot, coupled *I* and *S* resonances are indicated by the presence of cross-peaks at the characteristic chemical shifts in ν_1 and ν_2. This method illustrates the *I*-*S* interaction more clearly than the CP experiment.

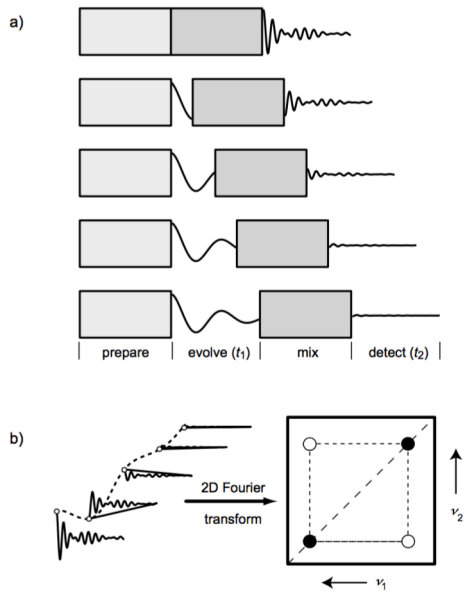

Figure 13: a) Acquisition of a typical 2D NMR experiment b) Indirect detection and FT to generate a contour plot. Taken from [12]

1.3.6 Rotational Echo Double Resonance (REDOR)

There are many instances in which it is not useful or feasible to indirectly detect *I*-*S* spin coupling using HETCOR or CP, such as in the presence of complex CP kinetics, or very dilute concentrations of the *I* (abundant) spin, which would require a prohibitively large amount of spectrometer time to obtain useable signal. Rotational echo double resonance NMR spectroscopy[18] provides an additional means of resolving internuclear distances via heteronuclear dipolar coupling. The REDOR pulse sequence is shown in Figure 14, in this case demonstrating a ^{31}P-observe ^{31}P-^{27}Al REDOR. The upper most pulse sequence is a simply spin echo for ^{31}P; application of a 180° pulse after time *t* refocuses the magnetization the de-phased due to T_2^* processes (e.g. heterogeneous

chemical shifts) and an echo of the original FID is observed at time *2t*. In the case of the REDOR experiment the echo is called a rotational echo because the spacing of the 90° and 180° pulses is synchronized with the period of rotation under MAS. After the ^{31}P rotational echo is collected, a similar pulse sequence begins, identical with regard to ^{31}P, however a series of 180° pulses are now applied to ^{27}Al, at every half rotor period. While the heteronuclear dipolar coupling is averaged under MAS over one rotor period, by applying 180° pulses every half-rotor period, the coupling is reintroduced, and interferes with the refocusing of those ^{31}P resonances coupled to ^{27}Al. As a result, the intensity of the REDOR echo is diminished relative to the rotational echo. By subtracting the REDOR echo (S) from the initial rotational echo (S_0), only those ^{31}P NMR signals that are coupled to ^{27}Al can be resolved from bulk ^{31}P signal. In addition, the kinetics of dephasing, reported typically as $((S_0 - S) / S_0)$ is a function of the magnitude of the dipolar coupling, and hence the internuclear distance between both spins. In similar fashion to the modulation of contact time under CP/MAS, modulation of the number of rotor periods (τ in Figure 14) can provide insight into the internuclear distance between *I* and *S* spins.

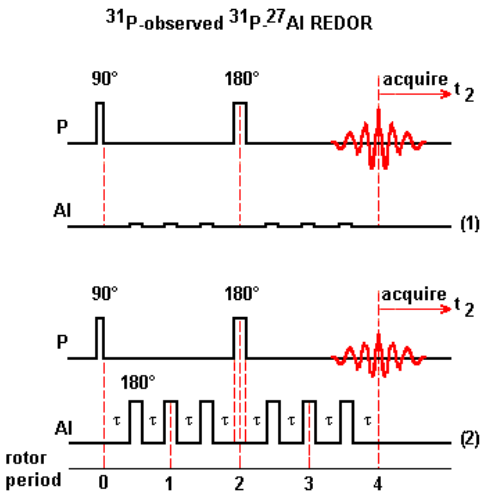

Figure 14: The REDOR pulse sequence

Chapter 2: Variation of carbonate substitution with synthesis conditions in Na-free carbonate hydroxylapatite

2.1 Abstract

A set of carbonated hydroxylapatites (CHAPs) enriched in ^{13}C was prepared by aqueous precipitation methods. The Ca:P molar ratio was varied between samples, and $^{13}C\{^{1}H\}$ cross-polarization NMR spectroscopy reveals that modification of the Ca:P ratio changes the type of carbonate substitution. For those samples with excess phosphorus, carbonate is present in both the hydroxyl (A) and phosphate (B) sites, called AB-type. To our knowledge AB-type CHAP has not yet been identified in samples prepared exclusively via aqueous precipitation methods, thus revealing a new synthetic route to AB-type CHAP. $^{1}H\{^{13}C\}$ and $^{1}H\{^{31}P\}$ REDOR NMR spectra indicate that modification of the Ca:P ratio and/or substitution of carbonate results in ^{1}H resonances at greater chemical shift than that of hydroxylapatite, which may be due to hydroxyl groups proximal to vacancies.

2.2 Introduction

The mineralized component of bone and dental enamel is composed primarily of hydroxylapatite, $Ca_5(PO_4)_3OH$ (HAp) with varying amounts (3-8%)[19] of carbonate, substituted either in place of phosphate groups or in the anion channel in place of hydroxyl groups. It was demonstrated somewhat recently that the amount of carbonate within microcalcifications in breast tissue may be linked to malignancy, and a correlation between carbonate content, specifically substitutions into the anion channel, and bone maturity, has also been established[20]-[22]. Clearly, substitutions for carbonate into the hydroxylapatite (HAp) structure are important in the body, and can provide insight into

molecular level processes related to biomineralization. In addition, much work related to hydroxylapatite has been devoted to developing novel biomaterials such as prostheses and artificial joints and limbs, most of which utilize HAp as an intermediary between the native bone and implant. Those hydroxylapatite compositions that contain carbonate experience more rapid osseointegration than their non-carbonated counterparts[23], raising further questions about carbonated apatite, its relation to biominerals, and the mechanisms of carbonate substitution.

Carbonate can substitute into the HAp for phosphate or hydroxyl groups, termed B-type and A-type carbonate, respectively. Both types of substitution introduce a local charge imbalance; B-type substitution introduces a net positive charge (CO_3^{2-} vs. PO_4^{3-}), whereas A-type substitution introduces a net negative charge (CO_3^{2-} vs. OH^-). Many proposed substitution mechanisms through which charge balance is maintained have been proposed, and are reviewed extensively elsewhere[4]. These proposed substitutions involve vacancies for calcium and hydroxyl groups, protonated carbonate groups and phosphate groups, and incorporation of monovalent cations such as Na^+ and NH_4^+.
The type of carbonate substitution observed in the Hap-like mineral component of bone is a combination of both A and B-type substitution, aptly named AB-type carbonate, wherein substitutions can occur for both sites[24]. Many efforts have focused on preparing AB-type carbonate, in order to emulate the structure and composition of bone. However, these methods typically employ monovalent cations (e.g. Na^+) to deliver carbonate. Such cations have been observed within the apatite structure[25]. Although trace amounts of sodium have been detected within bone[19], the amount of sodium is much less than required for charge balance with carbonate. In the present work, we seek

to synthesize AB-type carbonated hydroxylapatite without the use of a monovalent counter-cation, and to understand the mechanism of carbonate substitution in apatite believed to be more representative of that in bone than those compositions containing significant concentrations of sodium.

2.3 Materials and Methods

2.3.1 Apatite Synthesis

^{13}C-enriched carbonated hydroxylapatites (abbreviated 13CHAP throughout) were prepared using a modification of a method originally developed by Gibson and Bonfield[23]. The principal modification employed for the present work is the omission of high-temperature treatment with gaseous CO_2.

^{13}C-enriched CO_2 gas was slowly bubbled into a 25 mL aqueous solution previously acidified by the addition of 85% w/w H_3PO_4. The duration of bubbling was 10 minutes, determined by a preliminary experiment in which CO_2 was bubbled into de-ionized water while monitoring the pH. The solutions were assumed to be equilibrated, saturated with respect to CO_2 (P_{CO2} = 1 bar) when the pH of the solution no longer changed (ten minutes). The synthesis was carried out using identical tubing and a constant bubbling rate to ensure saturation of the phosphoric acid solutions with respect to CO_2. The CO_2-saturated H_3PO_4 solutions were immediately loaded into 60 mL BD syringes, and delivered via syringe pump to 25 mL of a 0.5 M $Ca(OH)_2$ slurry at a rate of 2 mL/ min for 10 min under magnetic stirring. After stirring overnight, the product was washed with de-ionized water. The solids were transferred to centrifuge tubes, which were then filled with DI water, physically shaken and sonicated for 5 minutes, followed

by centrifugation (10 min at 3500 rpm) and decanting of the supernatant. This washing procedure was repeated three times, and the samples were then dried at 70°C for 48 hours. Modification of the Ca:P molar ratio for 13CHAP-1.67, 2.0, and 1.43 was afforded by modifying the amount of 85% w/w H_3PO_4 added; for 13CHAP-1.67(2x) both the concentration of $Ca(OH)_2$ and H_3PO_4 were modified. Table 2 lists the target and measured Ca:P molar ratios for each of the four samples studied in this work.

Sample	*Notes*	*Target Ca:P*	*Measured Ca:P*	*Wt% Ca*	*Wt% P*	*% Difference from expected Ca:P*
13CHAP-1.67	Stoichiometric HAp	1.67	1.61(2)	35.5(4)	16.70(6)	-3.4
13CHAP-2.0	PO_4-deficient	2.0	1.69(2)	34.7(2)	15.88(9)	-15.6
13CHAP-1.43	Ca-deficient	1.43	1.41(1)	34.1(3)	18.71(6)	-1.6
13CHAP-1.67(2x)	Double Ca+P concentration	1.67	1.42(2)	36.2(4)	19.69(7)	-14.8

Table 2: Synthesis parameters and elemental analysis of 13CHAP samples

2.3.2 Chemical Analysis

The inductively coupled plasma-optical emission spectrometry (ICP-OES) data were collected using a Thermo iCAP 7000 series spectrometer configured with a radial torch and aqueous nebulizer. A series of five Ca and P standards were prepared in the expected range of concentrations for digested samples (10-120 ppm). The Ca:P molar ratio was fixed at 1.67 for all standards to compensate for matrix effects. The sample solids were digested in nitric acid prior to dilution. Wavelengths of 422.673 and 178.284 nm were selected for analysis of Ca and P, respectively. Measurements were made in triplicate, and uncertainties were determined from the variance.

2.3.3 Powder X-Ray Diffraction (PXRD)

Powder X-Ray diffraction patterns were collected on a Scintag PADX diffractometer (Cu Kα radiation) between 15 and 60° 2θ at a scanning rate of 0.5°/min, with a stepsize of 0.02. Lebail refinements of the lattice parameters were performed using EXPGUI[26]. The 002 reflection was fit using fityk[27].

2.3.4 Vibrational Spectroscopy

Raman and infrared (IR) spectra were collected at the Stony Brook University Vibrational Spectroscopy Laboratory. Raman spectroscopy was completed using a WITec alpha300R Micro-Imagining Raman spectrometer. This system configuration combines a confocal microscope with a highly sensitive thermoelectrically cooled, back-illuminated CCD detector allowing for the detection of low intensity Raman shifts. A 50_X optical magnification was used to produce a sub-micron spot size. A 600 line/mm holographic grating spectrometer provided a 3 cm^{-1} spectral resolution between the region of 100-3700 cm^{-1}. Each spectrum was acquired using a 785 nm laser for 120 accumulations during a one second integration period. Spectra were corrected for cosmic ray interference and then the data were reduced to subtract the incident laser line and background. A Thermo Fisher Nicolet 6700 Fourier Transform Infrared (FTIR) Michelson interferometer was used to acquire IR measurements across a spectral range of 400-4000 cm^{-1} in absorbance mode. The spectrometer was equipped with a SmartOrbit attenuated total reflectance (ATR) accessory with a Type IIa diamond element, allowing for the direct measurement of sample powders.

2.3.5 ^{1}H Single Pulse NMR

Solid-state ^{1}H NMR spectra were obtained on a Varian Inova 400 MHz (9.4 T) spectrometer operating at 399.895 MHz for ^{1}H at a spinning rate of 10 kHz, using a low ^{1}H background probe configured for 4 mm rotors. The rotor assembly consisted of ZrO_2 sleeves, Kel-F tips, and PTFE spacers. The ^{1}H pulse width (pi/2) was 5μs, and the relaxation delay was 30s. Chemical shifts were measured relative to the hydroxyl resonance in stoichiometric hydroxylapatite set to $\delta_H = 0.2$ ppm.

2.3.6 ^{31}P Single Pulse NMR

Solid-state ^{31}P NMR spectra were obtained on a ChemMagnetics 500 MHz (11.7 T) spectrometer operating at 499.786 MHz for ^{1}H and 202.318 MHz for ^{31}P at a spinning rate of 10 kHz, using a T3 HX probe configured for 4 mm rotors. The rotor assembly consisted of ZrO_2 sleeves, Kel-F tips, and PTFE spacers. The ^{31}P pulse width (pi/2) was 5μs, and the relaxation delay was 300s, chosen to ensure full relaxation. An 85 kHz ^{1}H decoupling field was applied during spectral acquisition. Chemical shifts were measured relative to the phosphate resonance in stoichiometric hydroxylapatite set to $\delta_P = 2.65$ ppm.

2.3.7 $^{13}C\{^{1}H\}$ Cross Polarization NMR

Solid-state $^{13}C\{^{1}H\}$ cross polarization NMR spectra were obtained on a Varian Inova 400 MHz (9.4 T) spectrometer operating at 100.560 MHz for ^{13}C and 399.895 MHz for ^{1}H at a spinning rate of 3.5 kHz, using a Varian Chemagnetics T3 probe configured for 7.5 mm rotors. The ^{1}H B_1 field was 50 kHz, and cross-polarization was achieved using a linear ramp of the ^{13}C B_1 field of approximately +- 3.5 kHz, centered

near the n = 1 sideband match condition. The ^{1}H decoupling field applied during acquisition was also 50 kHz. The relaxation delay was 1s, and spectra were collected at contact times of both 1ms and 8ms. The number of acquisitions varied owing to the differing amount of available material and extent of carbonate substitution in each sample. 40,000 scans were collected for 13CHAP-1.67, whereas 140,000 scans were collected for 13CHAP-2.0, 13CHAP-1.43 and 13CHAP-1.67(2x). ^{13}C chemical shifts were measured relative to tetramethylsilane (TMS) using adamantane as a secondary standard set to + 38.6 ppm.

2.3.8 $^{1}H\{^{13}C\}$ REDOR NMR

Solid-state $^{1}H\{^{13}C\}$ rotational echo double resonance (REDOR[18]) NMR spectra were obtained on a Varian Infinity Plus 500 MHz (11.7 T) spectrometer operating at 499.7845 MHz for ^{1}H and 125.661 MHz for ^{13}C at a spinning rate of 8 kHz, using a low ^{1}H background probe with an alumina spinning assembly for 5 mm (OD) rotors. The 90° ^{1}H pulse width was 5μs, and the relaxation delay was 2s. 10μs 180° pulses were applied to ^{13}C every half-rotor period for three different durations: 1.5ms (12 rotor periods), 8ms (64 rotor periods), and 32ms (256 rotor periods) in order to identify the various coupling schemes between ^{1}H and ^{13}C.

2.3.9 $^{1}H\{^{31}P\}$ REDOR NMR

Solid-state $^{1}H\{^{31}P\}$ REDOR NMR spectra were obtained on a Varian Infinity Plus 500 MHz (11.7 T) spectrometer operating at 499.7845 MHz for ^{1}H and 202.311 MHz for ^{31}P at a spinning rate of 8 kHz, using a low ^{1}H background probe with an

alumina spinning assembly for 5 mm (OD) rotors. The 90° ^{1}H pulse width was 5μs, and the relaxation delay was 2s. 10μs 180° pulses were applied to ^{31}P every half-rotor period for three different durations: 8ms (64 rotor periods), 16ms (128 rotor periods), and 32ms (256 rotor periods) in order to identify the various coupling schemes between ^{1}H and ^{31}P.

2.3 Results

2.4.1 Elemental Analysis

ICP-OES results are shown in Table 2. The measured Ca:P ratios are consistently lower than the target ratios, and the greatest deviations are observed in 13CHAP-2.0 and 13CHAP-1.67(2x). However, unreacted $Ca(OH)_2$ was observed during synthesis of 13CHAP-1.67(2x) that could not be transferred to the reaction vessel, which explains why this composition was more deficient in Ca than expected. Deviation from target stoichiometry for the other three samples is discussed below in the context of other results.

2.4.2 Powder X-Ray Diffraction (PXRD)

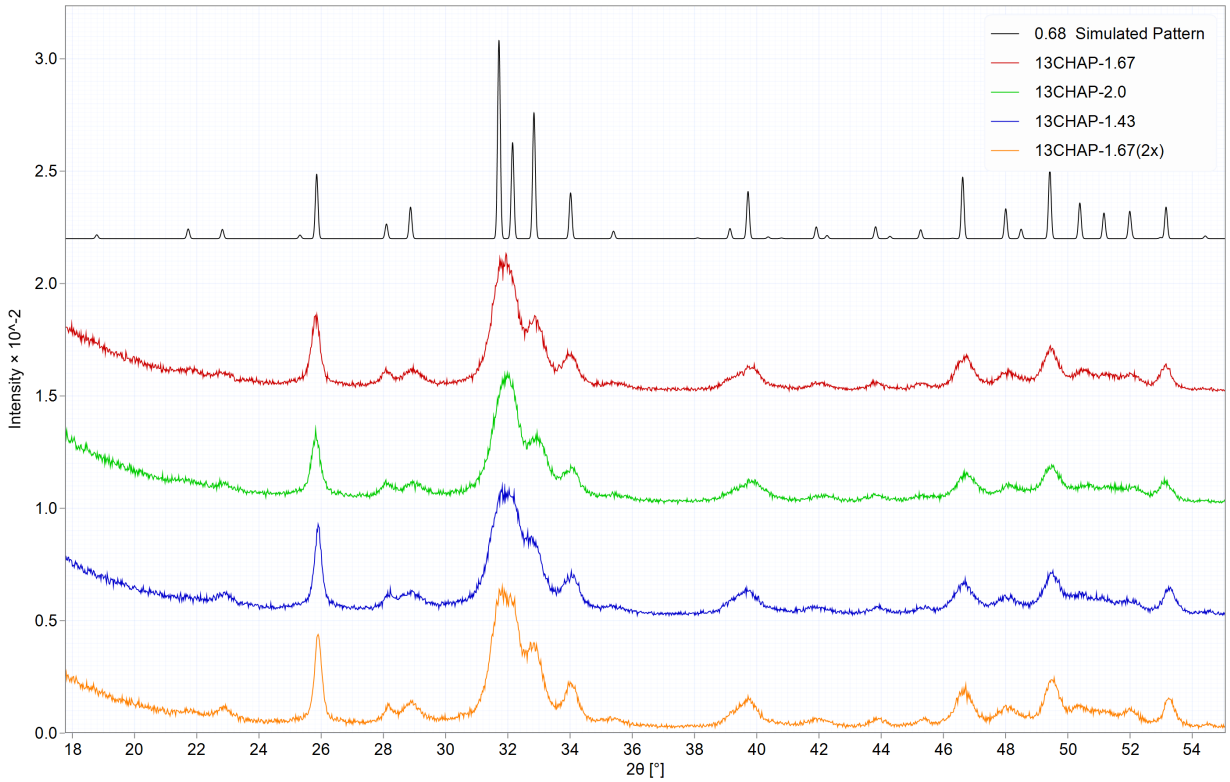

Figure 15: PXRD Results

Sample	a (Å)	c (Å)	vol (Å^3)	chisq	wRp	FWHM 002	Wt% CO_3[a]
13CHAP-1.67	9.4323(7)	6.8920(6)	531.03(7)	1.9	0.0949	0.177	1.28
13CHAP-2.0	9.4222(8)	6.8961(8)	530.21(8)	1.839	0.0931	0.182	2.97
13CHAP-1.43	9.4541(8)	6.8747(6)	532.17(8)	1.881	0.0958	0.140	-2.35
13CHAP-1.67(2x)	9.4428(8)	6.8801(6)	531.28(7)	2.55	0.1117	0.145	-0.47

Table 3: Lebail refinement and fitting of the 002 reflection. [a]wt% CO_3 determined by linear correlation with *a* lattice parameter documented in LeGeros et al.[28]

PXRD patterns for the present samples are shown in Figure 15, and the results of Lebail refinements are shown in Table 3. The simulated pattern at the top of Figure 15 is derived from the hydroxylapatite structure reported in [29]. The position and intensity of the reflections in this simulated pattern correspond well to those observed in the experimental patterns. The experimental reflections are very broad, resulting in overlap of many reflections, particularly for the series of reflections between 31-35° 2θ.

The effect of carbonate substitution on HAp lattice parameters is well documented for both A-type and B-type substitutions, the latter of which is typically observed for aqueous precipitation methods, which were utilized here. Increasing carbonate substitution for phosphate (B-type) in HAp results in a decrease in the *a* lattice parameter, and a minor increase in the *c* parameter[28]. Given the synthesis conditions 13CHAP-2.0 is expected to contain the greatest amount of carbonate, and 13CHAP-1.43 is expected to contain the least amount. The refined lattice parameters shown in Table 3 reflect this trend; 13CHAP-2.0 has the smallest *a* parameter and the largest *c* parameter, and the converse is true for 13CHAP-1.43.

Based on LeGeros et al.[28] the amount of B-type carbonate can be calculated from the *a* lattice parameter, via:

$$a = 9.44 - 0.006*(\text{wt\% B-type } CO_3) \quad (18)$$

The approximate wt% CO_3 for the present samples calculated from this relationship is tabulated in the right-most column of Table 3. As predicted based on synthesis conditions, 13CHAP-2.0 contains the greatest amount of carbonate, followed by 13CHAP-1.67. The results for 13CHAP-1.43 and 13CHAP-1.67(2x), however, yield negative values for the wt% CO_3, because the *a* lattice parameter for these samples is greater than 9.44Å, used in the above equation. It is well known[19] that A-type substitution results in dilation of the anion channel, which results in larger *a* lattice parameter values. We postulate based on these results that 13CHAP-1.43 and 13CHAP-1.67(2x) may contain a significant amount of A-type carbonate.

Liao et al.[30] noted that increasing amount of carbonate results in smaller crystallite size, which gives rise to broadened XRD peaks in the case of submicron particle size. This relation is described by the Scherrer equation.

$$\boldsymbol{\tau = \frac{K\lambda}{\beta cos\theta}} \quad (19)$$

τ is the crystallite size, *K* is the shape factor for the crystallite, λ is the X-ray wavelength, β is the full-width at half-maximum (FWHM) of the X-ray reflection, and θ is the Bragg angle. The 002 reflection was fit using fityk[27] and the results are shown in Table 3. The peak widths for this reflection are observed to narrow in the order 13CHAP-2.0 > 13CHAP-1.67 > 13CHAP-1.67(2x) > 13CHAP-1.43. This result suggests that those samples with high carbonate content are also finer grained, giving broadened peaks in the PXRD pattern.

2.4.3 Vibrational Spectroscopy

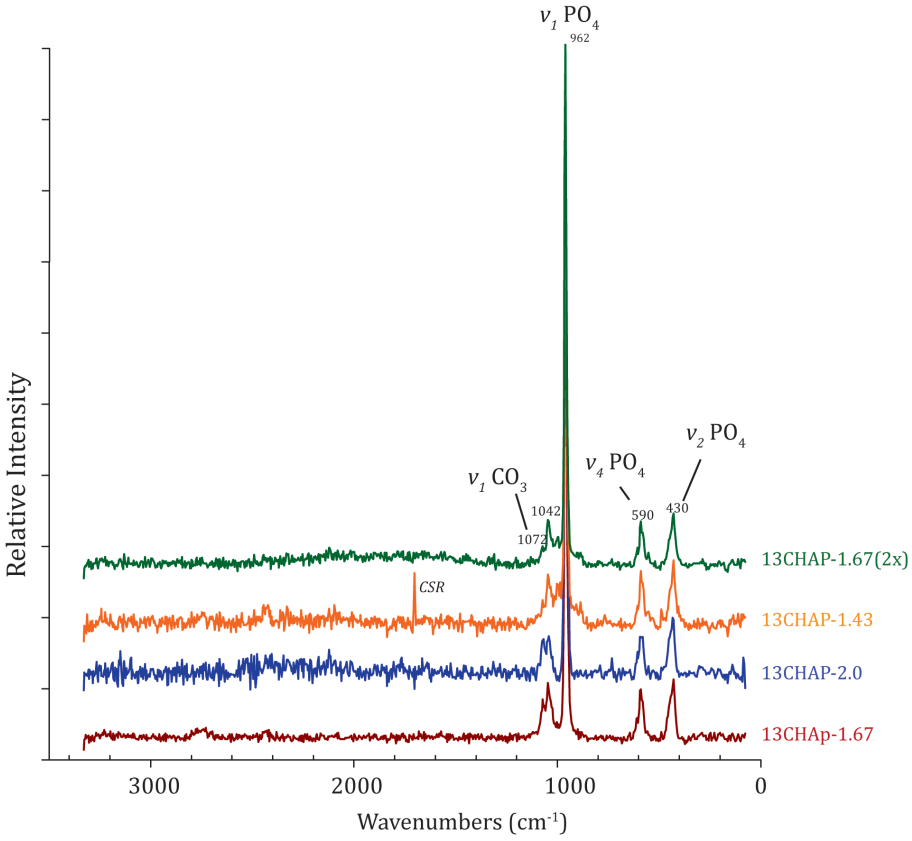

Figure 16: Raman spectra of 13CHAP samples

Raman spectra of the 13CHAP samples investigated in this work are shown in Figure 16. Bands due to phosphate are clearly visible in all samples; ν_1 PO_4 at 962 cm^{-1}, ν_2 PO_4 at 430 cm^{-1}, ν_3 PO_4 at 1042 cm^{-1}, ν_4 PO_4 at 590 cm^{-1}.[25], [31] The ν_1 CO_3 band at 1072 cm^{-1} is apparent in only two samples, 13CHAP-1.67 and 13CHAP-2.0. Krajewski et al.[31] observed that the width of the ν_1 PO_4 band is correlates linearly to the wt% CO_3.

$$\boldsymbol{wt\%\ carbonate} = \frac{(\boldsymbol{FWHM\nu_1 - 8.83})}{\mathbf{0.87}} \qquad (20)$$

The approximate weight percent carbonate in the present samples was calculated using this method and is shown in Table 4. The carbonate content calculated by this method is much greater than that from the refined lattice parameters. The relative amounts are in general agreement with the interpretation from the *a* lattice parameter, with 13CHAP-1.67 and 13CHAP-2.0 containing the greatest amount of carbonate, and 13CHAP-1.43

and 13CHAP-1.67(2x) featuring the least. However, as for the correlation between the *a* lattice parameter and carbonate content, the correlation between width of the ν_1 PO_4 band and carbonate content was derived from samples containing mainly B-type carbonate, so it is probable that calculation of A-type carbonate content is not fully taken into account using this method.

Sample	FWHM ν_1-PO_4 (cm^{-1})	wt% Carbonate[(a)]
13CHAP-1.67	13.77	5.69
13CHAP-2.0	14.54	6.56
13CHAP-1.43	12.92	4.70
13CHAP-1.67(2x)	12.35	4.06

Table 4: Approximation of carbonate content based on Raman spectra. (a) wt% carbonate determined using the method described by Krajewski et al.[31]

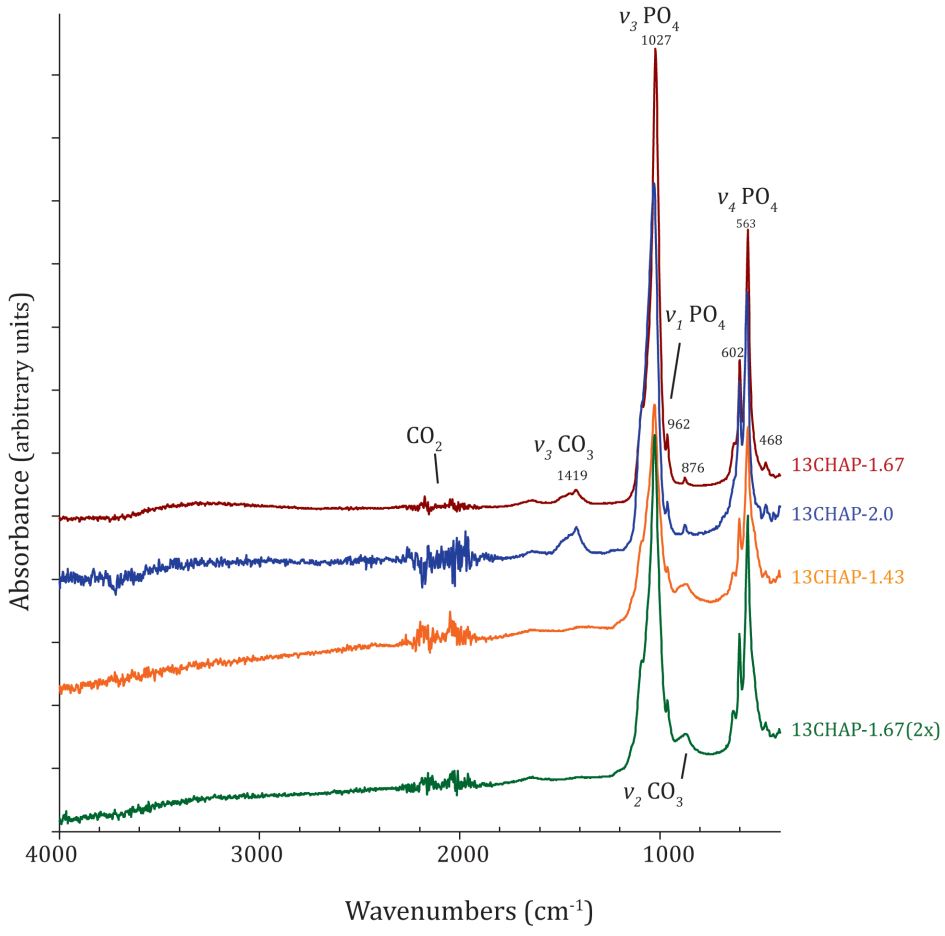

Figure 17: FTIR Spectra of 13CHAP samples

FTIR spectra of the 13CHAP samples investigated are shown in Figure 17. Several phosphate bands are also observed in these spectra: the ν_1, ν_3, and ν_4 PO_4 bands at 962 cm^{-1}, 1419 cm^{-1}, and 563-602 cm^{-1}, respectively. Carbonate ν_2 bands, near 876 cm^{-1}, are relatively narrow and well defined for 13CHAP-1.67 and 13CHAP-2.0, but are much broader for 13CHAP-1.43 and 13CHAP-1.67(2x). In a recent compilation of the literature, Fleet [19] demonstrated that ν_2 carbonate bands due to B-type substitution occur at lower wavenumbers than those for A-type substitution, and that relative to A-type or B-type carbonate in hydroxylapatite, the ν_2 bands in AB-type carbonate hydroxylapatite are much broader due to the overlap of A and B-type ν_2 bands. The type of carbonate substitution for 13CHAP-1.43 and 13CHAP-1.67(2x) is likely to be AB-type, based on the breadth of the ν_2 carbonate bands for these samples. The position of the ν_2 bands in 13CHAP-1.67 and 13CHAP-2.0 appear in the lower range of wavenumbers relative to the broad signals in 13CHAP-1.43 and 13CHAP-1.67(2x), and match within reasonable uncertainty the range specified by Fleet[19] for B-type carbonate (870-873 cm^{-1}). Therefore the type of carbonate in 13CHAP-1.67 and 13CHAP-2.0 is likely to be dominantly B-type. The weak intensity of the ν_2 bands prevents rigorous deconvolution and definitive assignment of the type of substitution The ν_3 carbonate band which Rey et al.[32] assign to B-type substitution is only observed in the spectra of 13CHAP-1.67 and 13CHAP-2.0. The observation of this band only in 13CHAP-1.67 and 13CHAP-2.0 further strengthens our interpretation that substitution is dominantly B-type.

2.4.4 ^{1}H Single Pulse NMR

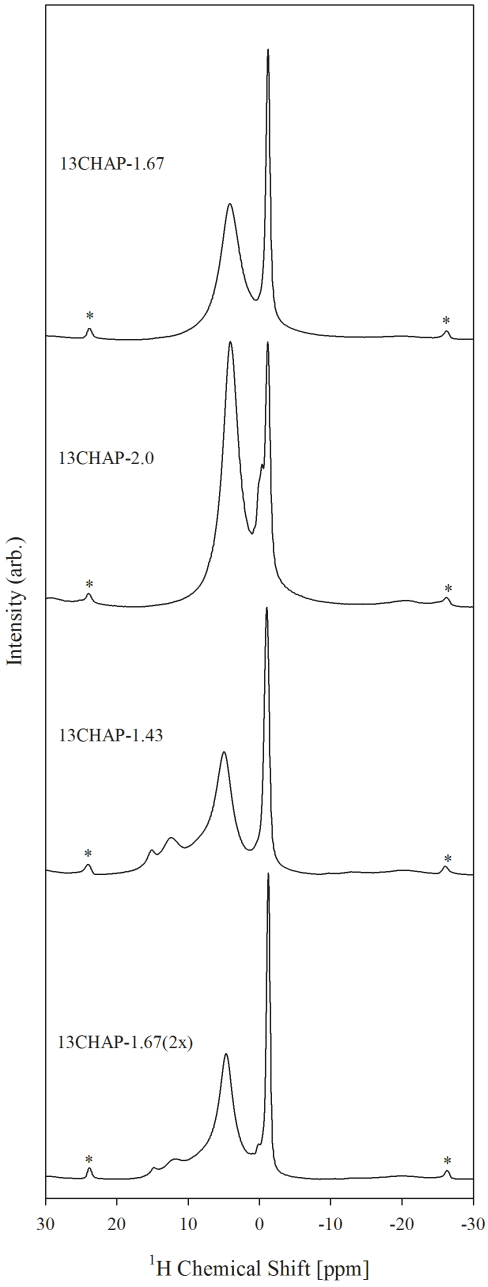

Figure 18: ^{1}H single pulse (SP) NMR spectra

13CHAP-1.67		
^{1}H Chemical Shift (ppm)	FWHM (ppm)	Relative Intensity
5.3	3.6	75.3(7)

0.1	0.7	29.4(7)
13CHAP-2.0		
5.3	2.0	75.7(3)
0.1	0.9	15.9(7)
1.3	1.1	8.4(9)
13CHAP-1.43		
6.2	3.3	21.6(3)
0.3	0.8	59.2(4)
13.4	4.0	18.3(2)
16.4	0.9	0.9(1)
13CHAP-1.67(2x)		
5.9	3.0	60.6(5)
0.0	0.6	23.6(5)
13.1	4.0	11.9(4)
1.4	0.90	3.3(1)
16.1	0.8	0.6(3)

Table 5: Results of fitting ^{1}H single pulse NMR spectra

The ^{1}H single pulse (SP) NMR spectra for the present samples are shown in Figure 18, and the results of fitting the spectra to a sum of Gaussian peaks are shown in Table 5. The ^{1}H SP spectrum of 13CHAP-1.67 contains two peaks; a narrow signal at 0.1 ppm and a broader signal at 5.3 ppm. These signals are observed in the ^{1}H SP spectra of all samples, however the chemical shifts and peak widths vary slightly. It is worth noting that the 0.1 ppm signal is broadest (0.89 ppm FWHM) for 13CHAP-2.0. An additional resonance is observed at 1.3 ppm for 13CHAP-2.0 that is also narrow, similar to the width of the signal at 0.1 ppm. Two additional peaks occur in the ^{1}H SP spectra of 13CHAP-1.43 and 13CHAP-1.67(2x): a broad (4 ppm FWHM) signal at 13.1-13.4 ppm and a narrower signal of lesser intensity at 16.1-16.4 ppm. A narrow (0.9 ppm FWHM) peak at 1.4 ppm is observed for 13CHAP-1.67(2x) similar to that at 1.3 ppm in 13CHAP-2.0.

The peak at 0.1 ppm in all samples closely resembles that previously reported for hydroxylapatite at 0.2 ppm,[33] and is assigned to hydroxyl groups in the apatite chanel.

The 1.3-1.4 ppm signals in 13CHAP-2.0 and 13CHAP-1.67(2x) have a comparable chemical shift and similar narrow lineshape to that assigned to hydroxyl groups at 0.1 ppm, so it is possible that this signal also arises from hydroxyl groups in the anion channel. ^{1}H chemical shifts correlate well with hydrogen bond length, which suggests these OH groups that exhibit higher chemical shifts experience a slight hydrogen bond interaction. The broad resonances at 5.3 ppm closely resemble signals attributed previously to surface adsorbed water[33] and are assigned accordingly. The peaks at 13.1-13.4 ppm and 16.1-16.4 ppm probably arise from an amorphous or poorly crystalline hydrogen phosphate impurity phase. This impurity could resemble monetite based on the similarity of the chemical shifts (13.6 and 16.2 ppm) previously[33]. This impurity phase is poorly crystalline because of the absence of any corresponding PXRD reflections in the patterns for these samples.

2.4.5 ^{31}P Single Pulse NMR

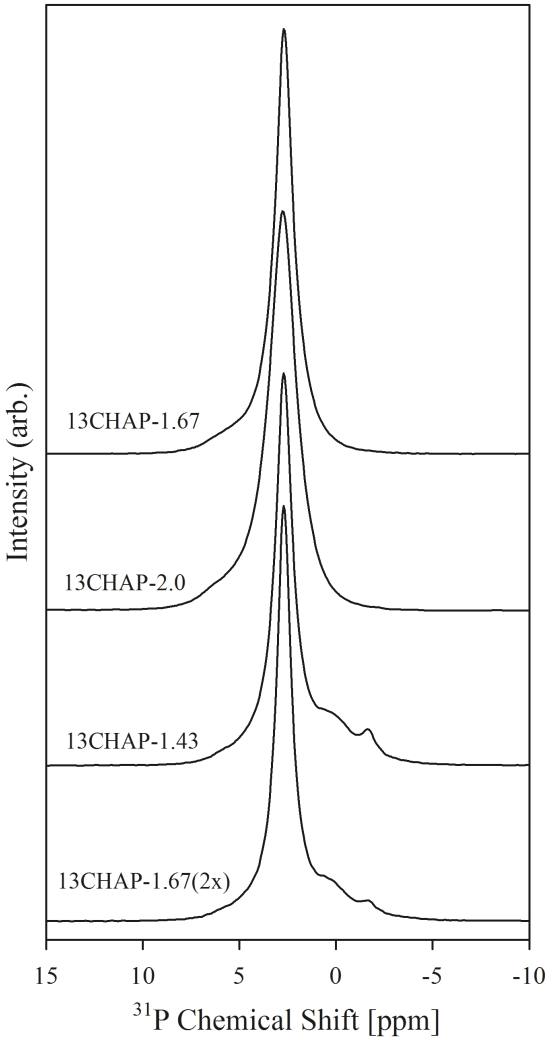

Figure 19: ^{31}P single pulse (SP) NMR spectra

13CHAP-1.67			
^{31}P Chemical Shift (ppm)	Raw FWHM (ppm)	FWHM (ppm)	Relative Intensity
2.6	1.1	1.9	73.8(4)
2.7		0.8	
3.5		4.2	26(1)
13CHAP-2.0			
2.7	1.7	2.0	66.8(9)
2.7		1.0	
3.4		4.6	33.1(9)
13CHAP-1.43			
2.7	1.1	1.4	53(4)
2.7		0.6	
3.6		3.5	19(2)

0.6		4.0	27(1)
-1.7		0.6	1.4(3)
13CHAP-1.67(2x)			
2.7	0.9	1.3	57(4)
2.7		0.6	
3.4		3.7	19(4)
0.8		4.3	24(3)
-1.8		0.6	0.6(3)

Table 6: Results of fitting ^{31}P NMR spectra

The ^{31}P single-pulse (SP) spectra are shown in Figure 19, and the results of fitting the spectra to a sum of Gaussian peaks are shown in Table 6. Two resonances appear in the spectra of all four samples; a narrower signal centered at $\delta = 2.7$ ppm, and a broad (FWHM $\approx$ 4 ppm) peak near $\delta = 3.6$ ppm. The peak at $\delta = 2.7$ ppm could not be fit with a single Gaussian curve, but could be modeled with the sum of a narrow and a broader curve at the same position. It is unlikely that the two peaks fit to the resonance at 2.7 ppm have any physical meaning but were included simply to improve the fit. Two additional signals are observed in spectra of 13CHAP-1.43 and 13CHAP-1.67(2x): a broad (~4 ppm FWHM) peak centered near 0.6-0.8 ppm and a narrower (0.6 ppm FWHM) signal at -1.7 or 1.8 ppm.

The chemical shift of the main peak, 2.7 ppm, is within experimental error reported previously for stoichiometric hydroxylapatite[34]. Therefore we assign this intensity to phosphate groups in the apatite structure. The width of this resonance increases among the four samples in the order: 13CHAP-2.0 > 13CHAP-1.67 > 13CHAP-1.43 > 13CHAP-1.67(2x) (Table 6). Substitution of carbonate introduces disorder into the apatite structure[35]. An increase in width of the apatite phosphate peak could be expected with increased amount of substituted carbonate. Such a relationship

seems to hold with the carbonate content estimated from PXRD and Raman spectroscopy. A slight deviation from this relation is between 13CHAP-1.43 and 13CHAP-1.67(2x), however the amount of carbonate in these samples is comparable, so the subsequent structural disorder may be similar.

The intensity of the broad shoulder at $\delta = 3.6$ ppm appears to increase with carbonate content as well; the greatest intensity is observed for 13CHAP-2.0 (~33%), and the least for 13CHAP-1.43 and 13CHAP-1.67(2x) (~20%). This signal may be due to a disordered phosphate impurity phase, however it is not clear if the presence of this phase is a result of carbonate substitution, or simply a function of synthesis conditions. The additional signals at -1.7 and 0.6 ppm observed in spectra of 13CHAP-1.43 and 13CHAP-1.67(2x) are tentatively assigned to the poorly crystalline hydrogen phosphate phase inferred to be present from the ^{1}H SP results, as similar ^{31}P resonances were observed in a previousy study of a series of calcium hydrogen phosphates [36].

2.4.6 $^{13}C\{^{1}H\}$ Cross Polarization NMR

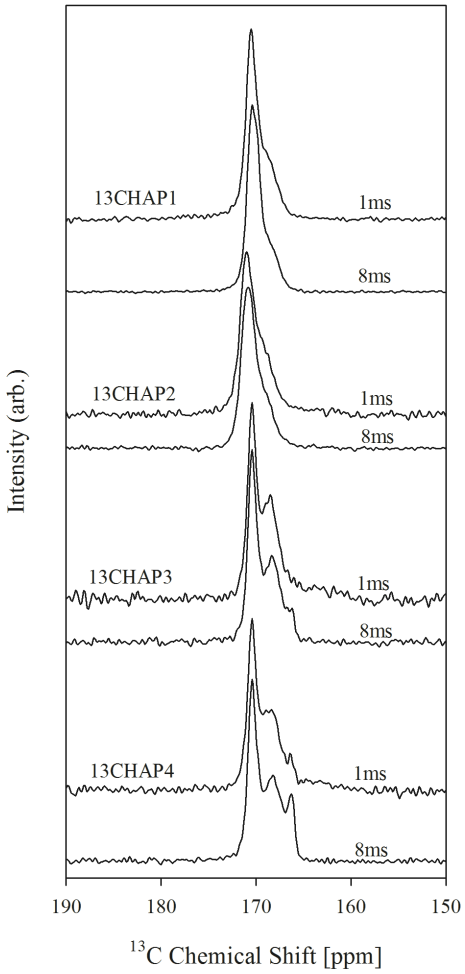

Figure 20: $^{13}C\{^{1}H\}$ Cross-polarization NMR spectra

^{13}C Chemical Shift (ppm)	FWHM (ppm)	Rel. Int. 1ms contact time	Rel. Int. 8ms contact time	Abs. Int. 1ms contact time	Abs. Int. 8ms contact time
13CHAP-1.67					
170.3	1.3	0.633(6)	0.71(2)	205(2)	413(9)
168.7	2.4	0.367(5)	0.29(2)	119(2)	169(9)
13CHAP-2.0					
170.5	1.6	0.704(4)	0.65(2)	81.6(4)	149(5)
169.2	2.7	0.296(4)	0.34(2)	34.3(5)	78(5)
13CHAP-1.43					
170.4	1.1	0.551(7)	0.466(7)	55.7(3)	80(1)
168.5	2.3	0.436(8)	0.50(1)	43.8(4)	87(2)
166.1	0.8	0.013(2)	0.026(4)	1.1(2)	4.4(7)

13CHAP-1.67(2x)					
170.4	1.2	0.343(3)	0.385(6)	33.6(2)	65(1)
168.2	2.2	0.635(4)	0.54(1)	62.2(4)	91(2)
166.2	0.9	0.022(1)	0.075(4)	2.1(1)	12.8(6)

Table 7: Fitting results for $^{13}C\{^{1}H\}$ cross polarization NMR spectra

The $^{13}C\{^{1}H\}$ cross-polarization NMR spectra of all carbonated-hydroxylapatite samples investigated in this work are shown in Figure 20, and the results of fitting the spectra to a sum of Gaussian peaks are shown in Table 7. Two resonances are observed in all samples; a relatively narrow signal centered near 170.4 ppm, and a broader feature at about 168.7 ppm. Although very similar resonances were reported by Mason et al. (170.8 ppm, 1.3 ppm FWHM and 169.8, 2.8 ppm FWHM), the intensity of the broad signal is much weaker in the present spectra, resulting in a markedly different spectral profile. The widths of these two resonances vary considerably between samples; the greatest widths are observed for both sites in 13CHAP-2.0 (1.6 and 2.7 ppm), and the narrowest resonances are observed in 13CHAP-1.43 and 13CHAP-1.67(2x) (1.2 and 2.2 ppm). This variation in peak width likely reflects differences in structural disorder and carbonate content[35]. As the carbonate concentration increases, a more distorted structure gives rise to a greater range of chemical environments, thus giving rise to a broadened ^{13}C NMR signals. The asymmetric ^{13}C spectral profile observed for both 13CHAP-1.67 and 13CHAP-2.0 closely resemble those described by Beshah et al.[37] for B-type carbonate hydroxylapatite, after heat treatment at 400°C for 24 hrs. Because of this close correspondence to the results reported previously we tentatively assign the type of carbonate substitution in 13CHAP-1.67 and 13CHAP-2.0 to B-type substitution of carbonate for phosphate. An additional narrow signal is observed in the spectra of 13CHAP-1.43 and 13CHAP-1.67(2x) at 166.1 ppm, assigned to A-type carbonate in the

hydroxyl position because of the close correspondence with a ^{13}C signal assigned by Beshah et al.[37] to A-type carbonate. The substitution type is classified as AB-type for both 13CHAP-1.43 and 13CHAP-1.67(2x). Beshah et al.[37] also reported ^{13}C spectra of AB-type carbonate apatites, to which the present spectra bear many similarities.

The absolute intensities tabulated in Table 7 show that the signal intensity of each of the resonances for all samples increases as the contact time is increased from 1ms to 8ms. This result indicates that spectral changes with contact time relate primarily to differences in the C/H cross-relaxation time, T_{CH}, rather than ^{1}H relaxation effects. The intensity of both dominant signals (170.4 and 168.7 ppm) increase similarly between 1ms and 8ms contact periods, suggesting that the observed asymmetric line shape is due to a single ^{13}C environment, or that the kinetics of cross polarization for both sites proceed at similar rates. Mason et al. described significant changes in intensity as a function of contact time; however data were collected at several intermediate contact times providing higher resolution of cross-polarization kinetics. Data at only two contact periods could be collected over the given time period for acquisition, so a detailed analysis of cross-polarization buildup kinetics could not be performed. ^{13}C single-pulse spectra could also not be collected, owing to the dilute concentration of carbonate.

2.4.7 $^{1}H\{^{13}C\}$ REDOR NMR

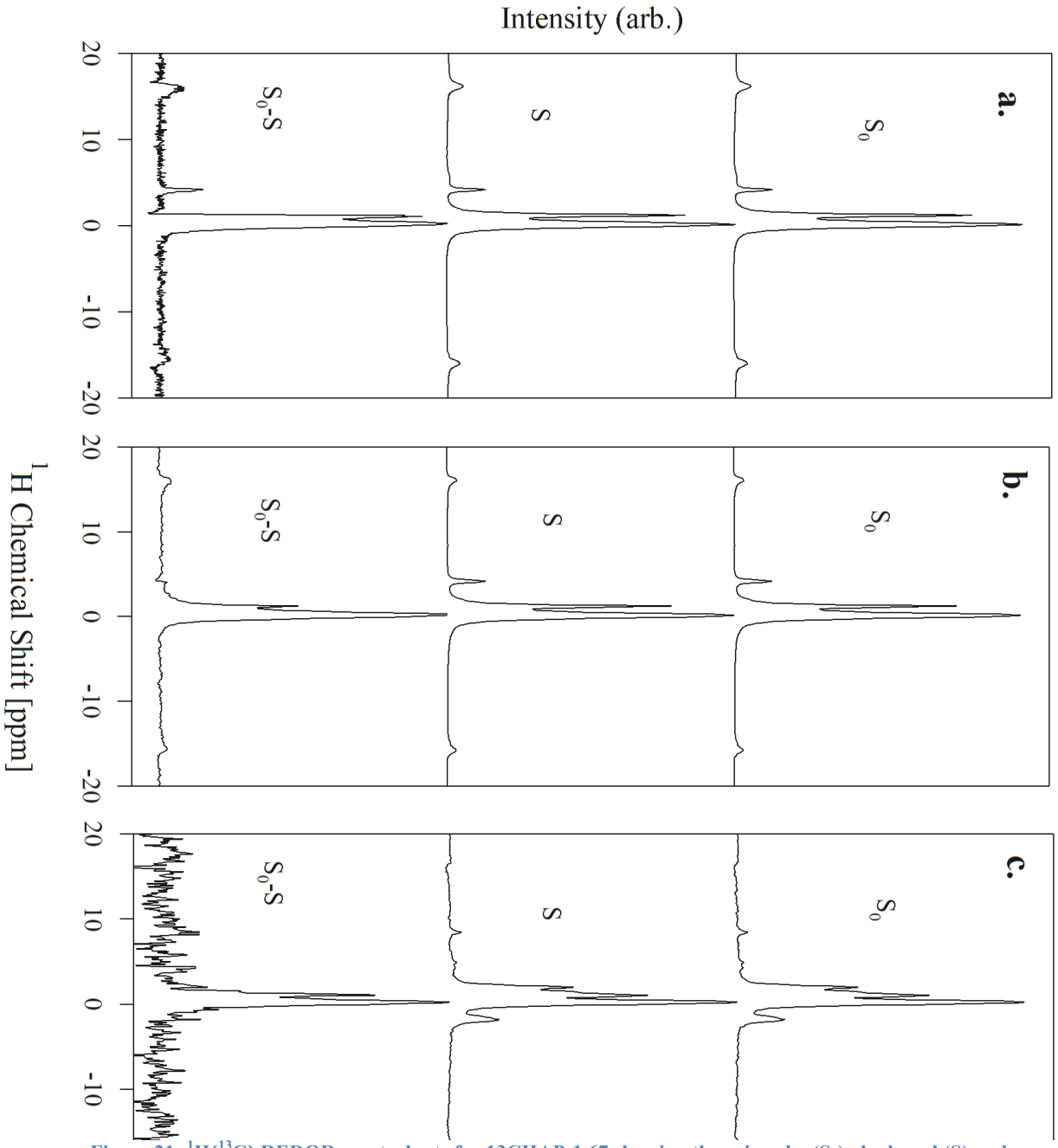

Figure 21: $^{1}H\{^{13}C\}$ REDOR spectral sets for 13CHAP-1.67 showing the spin echo (S_0), dephased (S) and difference spectra for dephasing times of a. τ = 1.5ms b. τ = 8ms and c. τ = 32ms

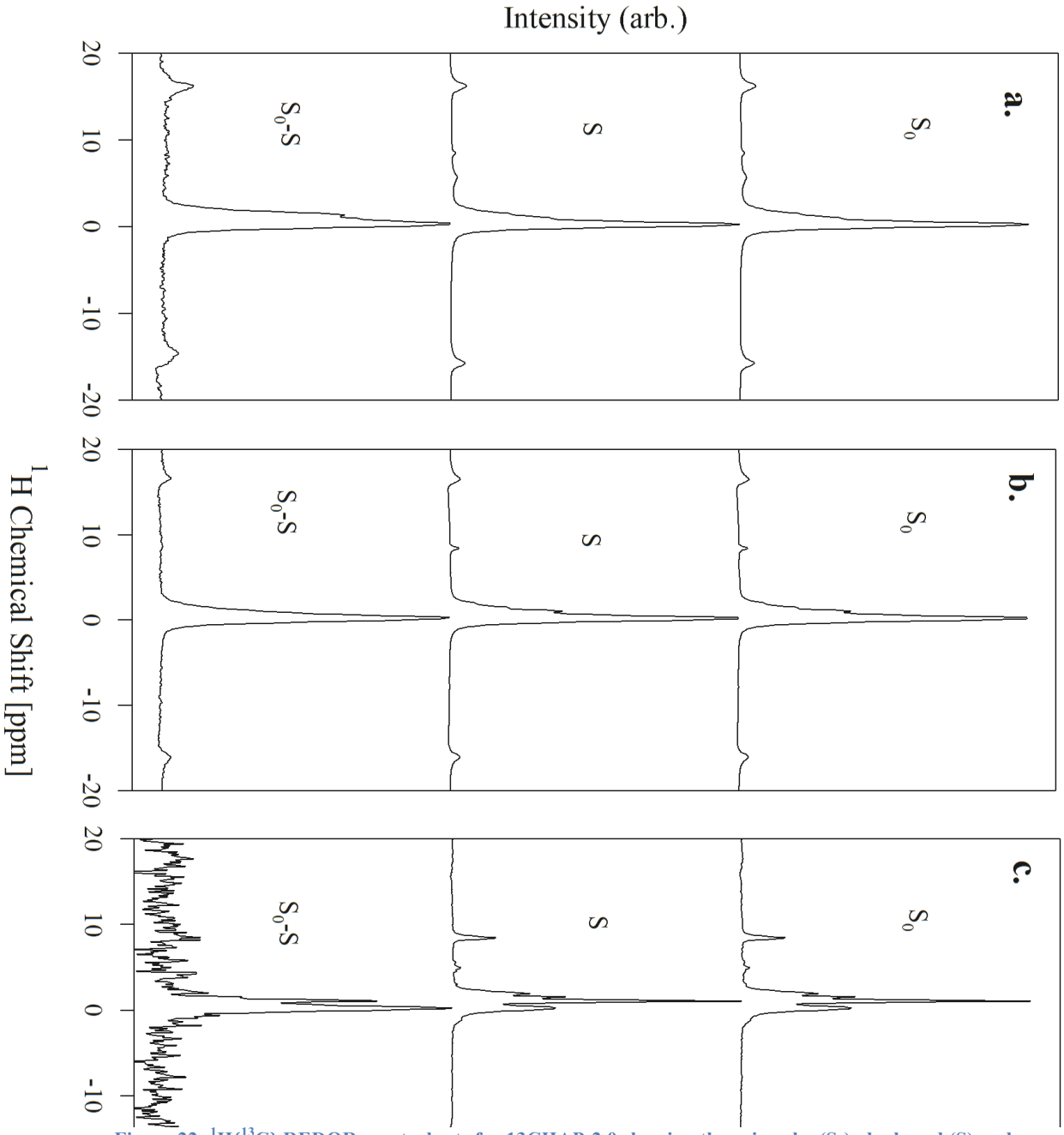

Figure 22: $^1H\{^{13}C\}$ REDOR spectral sets for 13CHAP-2.0 showing the spin echo (S_0), dephased (S) and difference spectra for dephasing times of a. τ = 1.5ms b. τ = 8ms and c. τ = 32ms

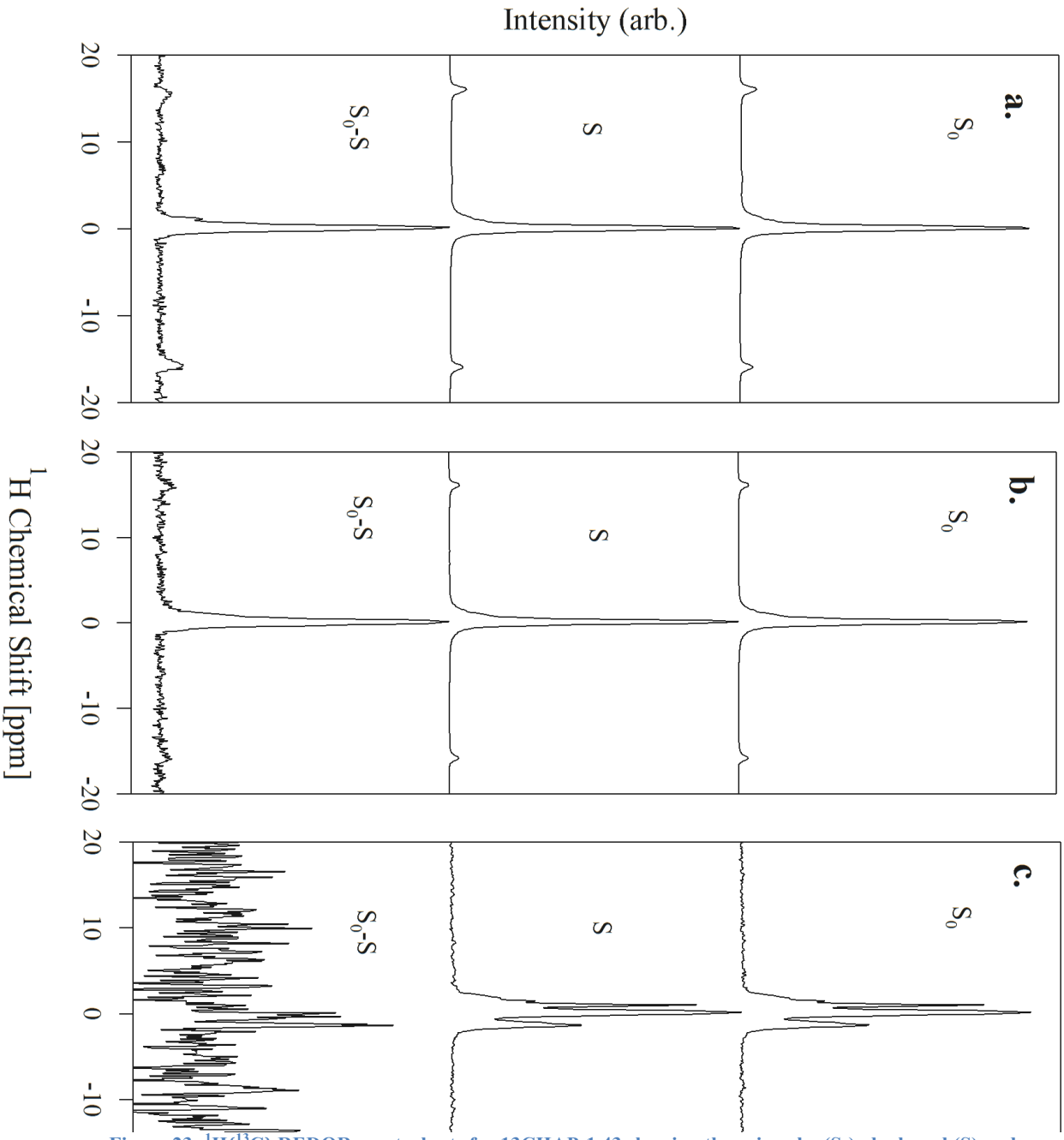

Figure 23: $^1H\{^{13}C\}$ REDOR spectral sets for 13CHAP-1.43 showing the spin echo (S_0), dephased (S) and difference spectra for dephasing times of a. τ = 1.5ms b. τ = 8ms and c. τ = 32ms

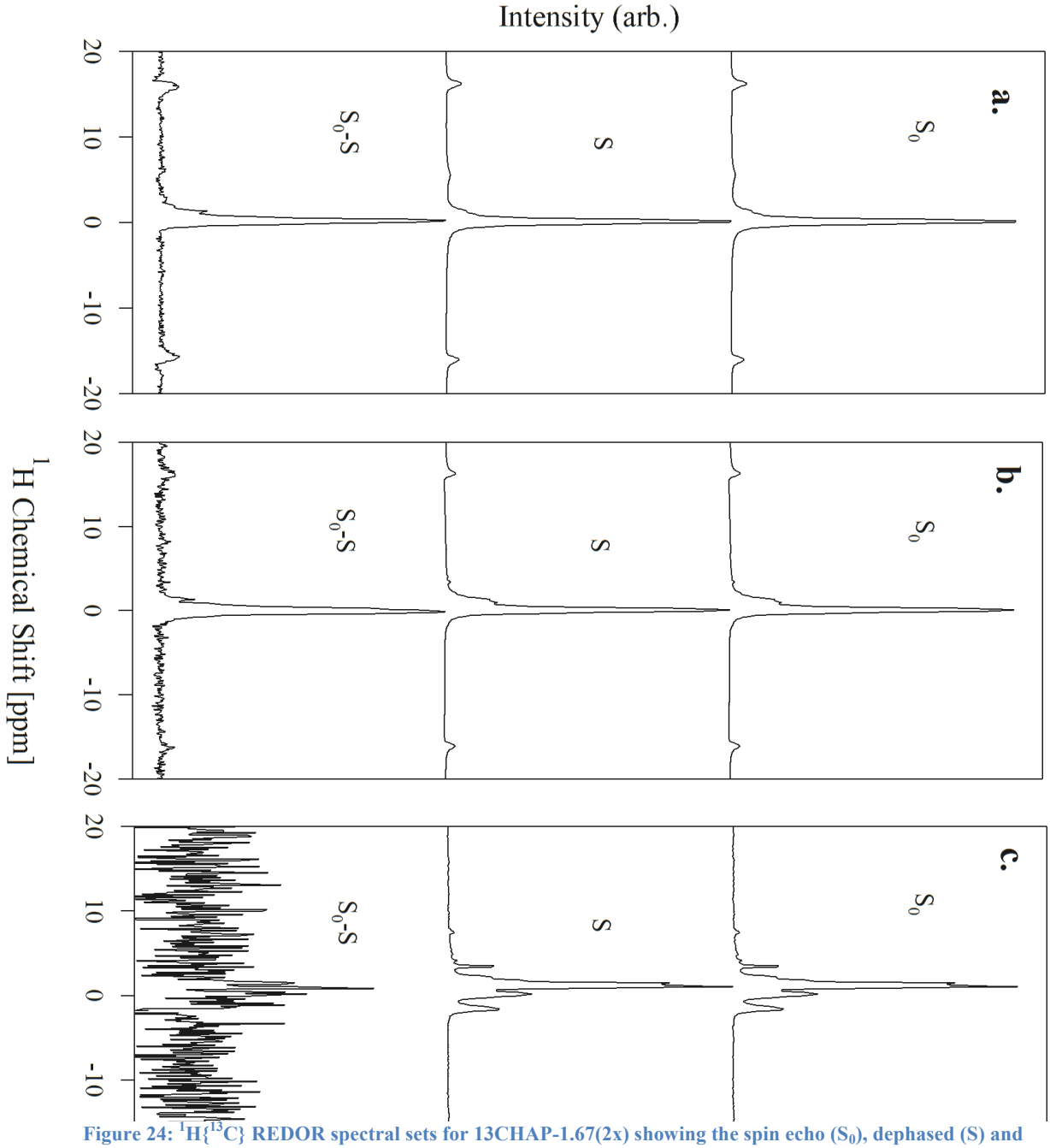

Figure 24: ^{1}H{^{13}C} REDOR spectral sets for 13CHAP-1.67(2x) showing the spin echo (S_0), dephased (S) and difference spectra for dephasing times of a. τ = 1.5ms b. τ = 8ms and c. τ = 32ms

Figures 21-24 contain rotational echo double resonance (REDOR) spectral sets for the present samples, and illustrate the three components of the experiment[18]. The upper-most spectrum (S_0) is the result of a spin-echo experiment showing signal from all ^{1}H in the sample, with the exception of those with short T_2, that are not refocused during the spin echo sequence. The middle spectrum (S) results from an identical ^{1}H spin-echo sequence, except that ^{13}C pulses are applied every half-rotor period, which reintroduces heteronuclear H-C dipolar coupling and attenuates those ^{1}H signals coupled to ^{13}C. This attenuation increases with increasing ^{1}H inter-pulse delay (also called the dephasing period, τ), and strength of H-C dipolar coupling (shorter H-C distances and/or greater number of nearby ^{13}C). Therefore, collection of ^{1}H{^{13}C} REDOR data at various dephasing periods, and analysis of the resultant dephasing kinetics can reveal structural information, in the form of H-C interatomic distances. The bottom spectrum (S_0-S) of each set is the REDOR difference spectrum, obtained by subtracting the attenuated spin echo (S) from the unperturbed spin echo (S_0). This spectrum shows resonances for ^{1}H environments that are coupled to ^{13}C.

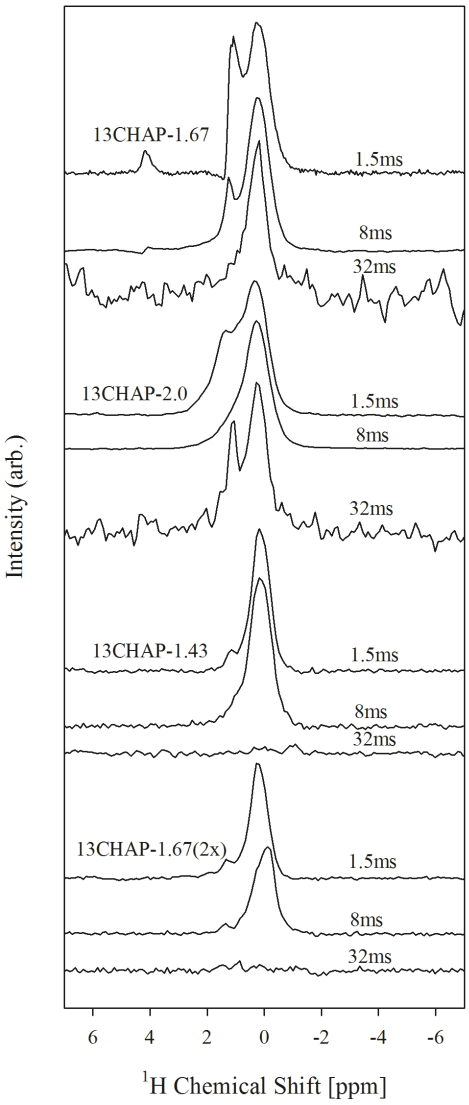

Figure 25: $^{1}H\{^{13}C\}$ REDOR Difference NMR spectra for the CHAP samples taken with dephasing times (τ) as indicated on the right

^{1}H Chemical Shift (ppm)	FWHM (ppm)	$(S_0\text{-}S)/S_0$ $\tau = 1.5ms$	$(S_0\text{-}S)/S_0$ $\tau = 8ms$	$(S_0\text{-}S)/S_0$ $\tau = 32ms$
13CHAP-1.67				
0.2	0.92	0.0052(2)	0.021(4)	0.046(3)
1.2	0.41	0.0037(2)	0.0095(7)	
4.1	0.38	0.0052(2)		
13CHAP-2.0				
0.3	0.95	0.004(1)	0.031(8)	0.057(4)
1.3	0.90	0.015(4)	0.041(3)	0.041(5)
13CHAP-1.43				
0.1	0.80	0.004(2)	0.016(2)	
1.1	0.62	0.0026(1)	0.039(4)	

13CHAP-1.67(2x)				
0.1	0.79	0.0037(2)	0.011(5)	
1.3	0.58	0.0016(5)	0.0023(8)	

Table 8: Fiting results for $^{1}H\{^{13}C\}$ REDOR difference spectra

The $^{1}H\{^{13}C\}$ REDOR difference spectra of all carbonate-hydroxylapatite samples are collected in Figure 25, and the results of fitting these spectra are listed in Table 8. The three right-most columns in Table 8 contain the fraction of the total ^{1}H signal (S_0) that attenuated by the ^{13}C pulses due to ^{1}H proximal to ^{13}C for each peak. The small size of the $(S_0\text{-}S)/S_0$ values reflects the minor contribution of carbonate in the present samples the relatively weak C-H dipolar coupling. Two relatively narrow signals are observed in all samples, near 0.2 and 1.3 ppm, although the chemical shifts of these signals vary slightly between samples. As with the ^{1}H single pulse (SP) spectra, the signal at 0.2 ppm is assigned to hydroxyl groups in the anion channel. The peak is slightly broader than that measured for the hydroxyl signal in the ^{1}H SP experiments. This difference may due to structural heterogeneity between bulk HAp and hydroxyl groups in HAp proximal to carbonate. The signal at 1.3 ppm was also observed in the ^{1}H SP spectrum of 13CHAP-2.0 and 13CHAP-1.67(2x), and is believed to be due to hydroxyl groups in the anion channel that experience slightly stronger H-bonding. The peak at 4.1 ppm is only present for 13CHAP-1.67 at τ = 1.5ms, but not at extended dephasing periods. It is possible that this signal arises from structural water, given the narrow lineshape and chemical shift comparable to that reported previously[38]. However, spinning side-bands were not observed for this peak, suggesting that the ^{1}H environments giving rise to this peak are mobile. The broad signal observed at 5.8 ppm in the ^{1}H SP NMR spectra does not occur in any of the ^{1}H spin-echo (S_0) spectra, preventing analysis via $^{1}H\{^{13}C\}$ REDOR. This

result indicates that this peak exhibits very short T_2, consistent with assignment to mobile, surface adsorbed H_2O.

In the difference spectra of 13CHAP-2.0, the 1.3 ppm signal persists at $\tau = 32$ms probably because of the elevated concentration of this environment. In fact the $^{1}H\{^{13}C\}$ REDOR fractions of both sites, 0.2 and 1.3 ppm are observed to be greatest for 13CHAP-2.0 (clearly shown in Figure 26), indicating a larger fraction of total ^{1}H signal is coupled to ^{13}C relative to the other samples. This result is in agreement with estimates of carbonate content from vibrational spectroscopy and PXRD.

In the $^{1}H\{^{13}C\}$ REDOR difference spectra of 13CHAP-1.43 and 13CHAP-1.67(2x), reasonable fits could be obtained only for dephasing periods of $\tau = 1.5$ms and 8ms, due to poor signal to noise at $\tau = 32$ms. The markedly poorer signal to noise in the difference spectra for 13CHAP-1.43 and 13CHAP-1.67(2x) and much smaller REDOR fractions $((S_0\text{-}S)/S_0)$ relative to the previous samples, suggests that the amount of ^{1}H signal that is coupled to ^{13}C is diminished in these samples relative to 13CHAP-1.67 and 13CHAP-2.0. This result is consistent with carbonate contents estimated from vibrational spectroscopy and PXRD. The broad resonances at 13.4 and 16.4 ppm in the ^{1}H SP NMR spectra of 13CHAP-1.43 and 13CHAP-1.67(2x) do not appear in the S_0 spin echo spectra collected during the $^{1}H\{^{13}C\}$ REDOR experiment, presumably due to rapid T_2 relaxation.

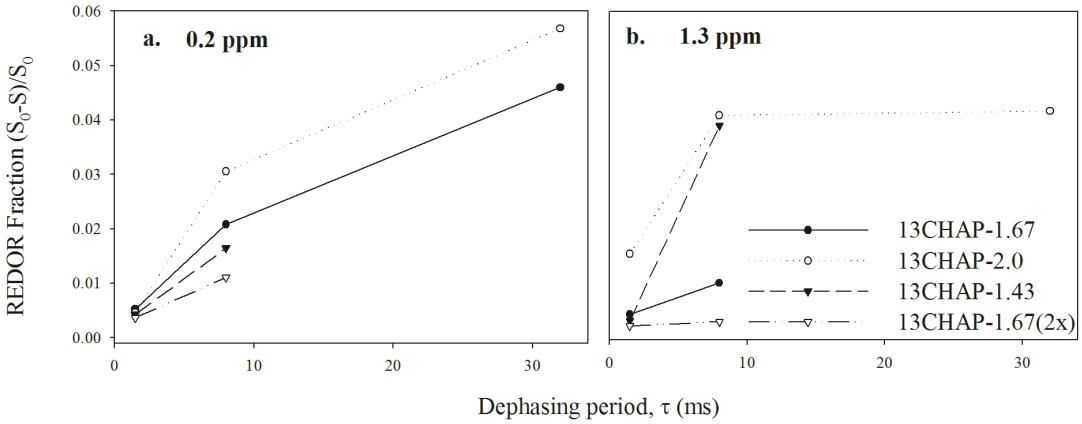

Figure 26: $^{1}H\{^{13}C\}$ REDOR fraction plots of NMR signals

2.4.8 $^{1}H\{^{31}P\}$ REDOR NMR

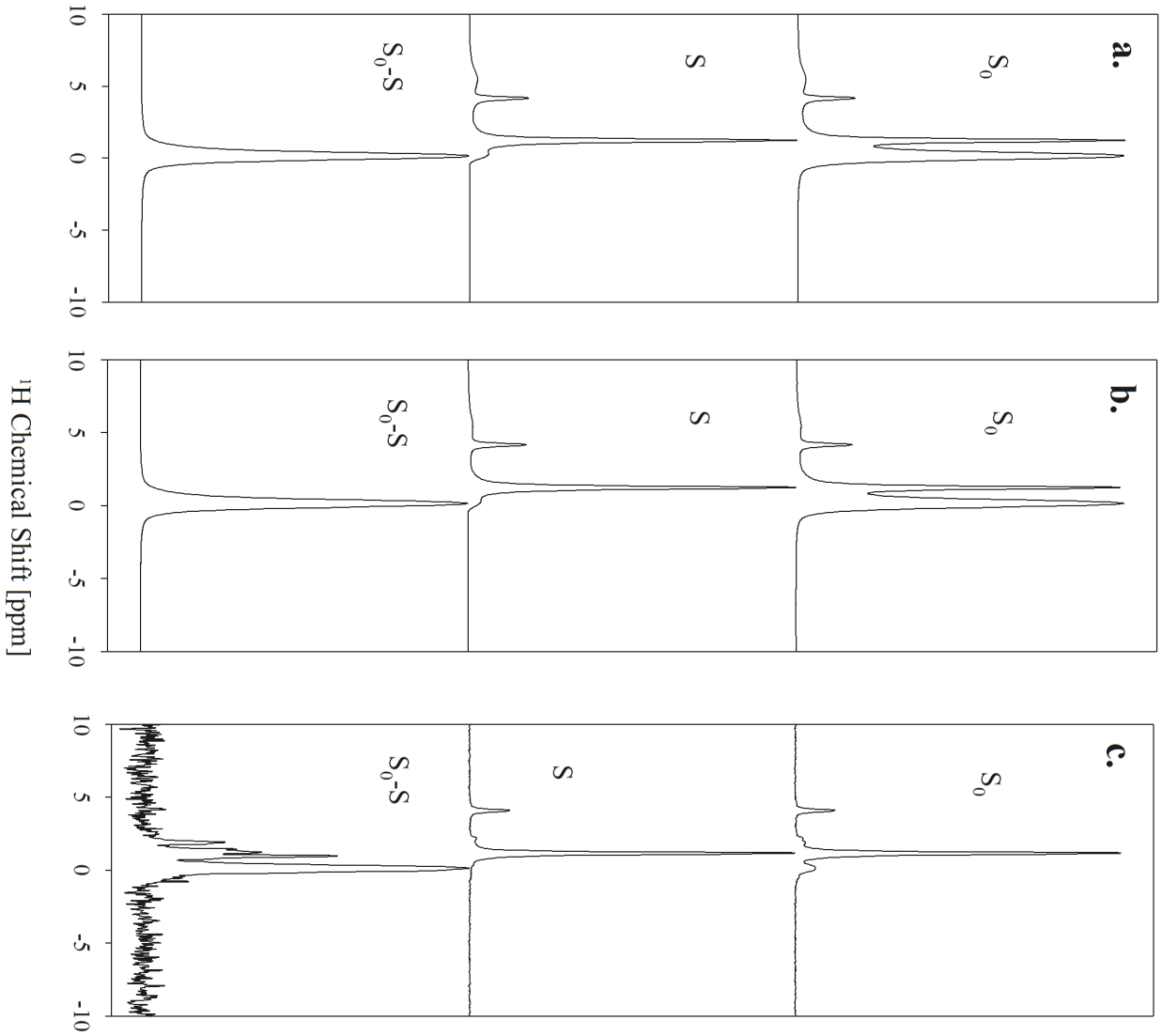

Figure 27: $^{1}H\{^{31}P\}$ REDOR spectral sets for 13CHAP-1.67 showing the spin echo (S_0), dephased (S) and difference spectra for dephasing times of a. τ = 8ms b. τ = 16ms and c. τ = 32ms

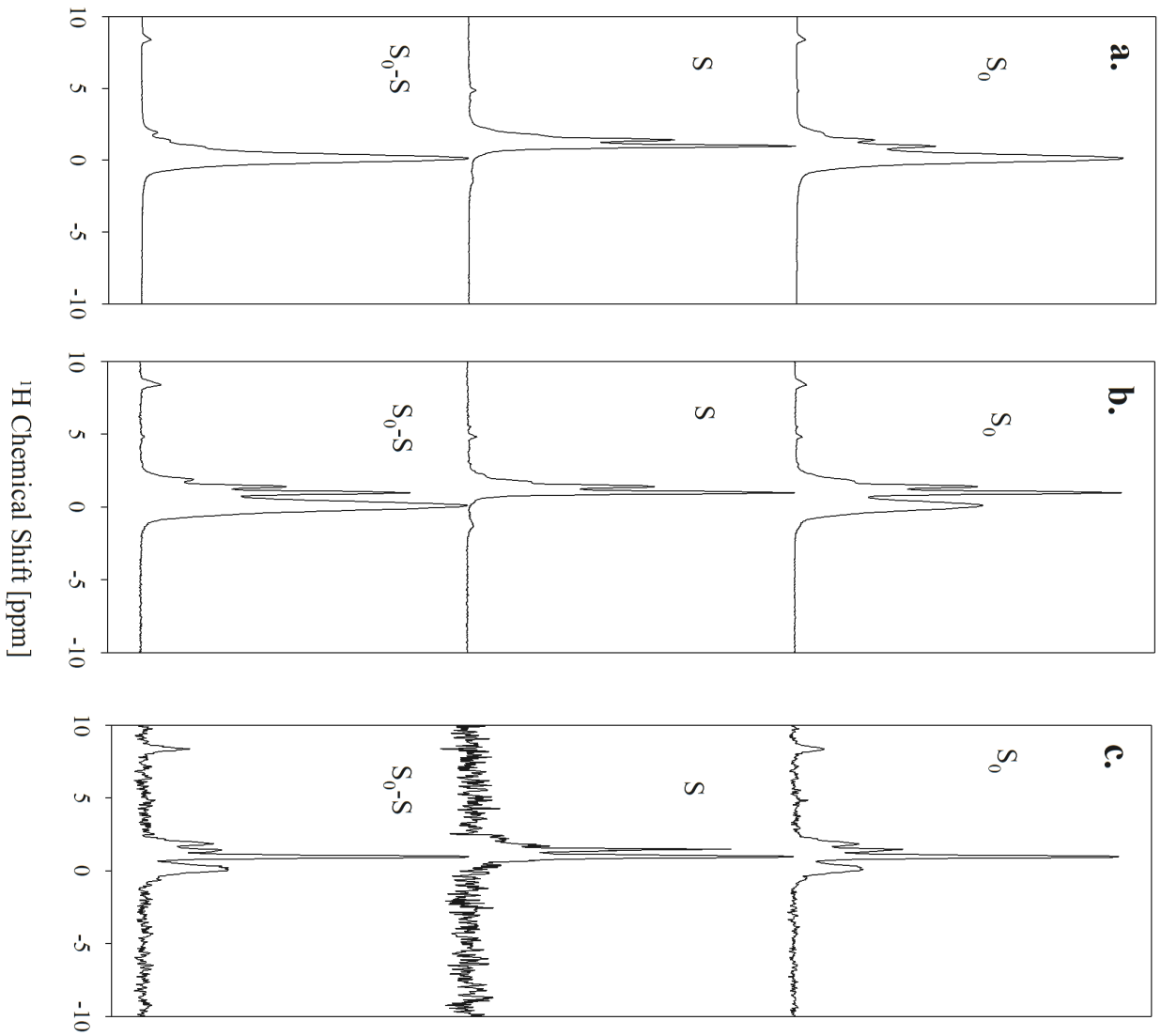

Figure 28: $^{1}H\{^{31}P\}$ REDOR spectral sets for 13CHAP-2.0 showing the spin echo (S_0), dephased (S) and difference spectra for dephasing times of a. τ = 8ms b. τ = 16ms and c. τ = 32ms

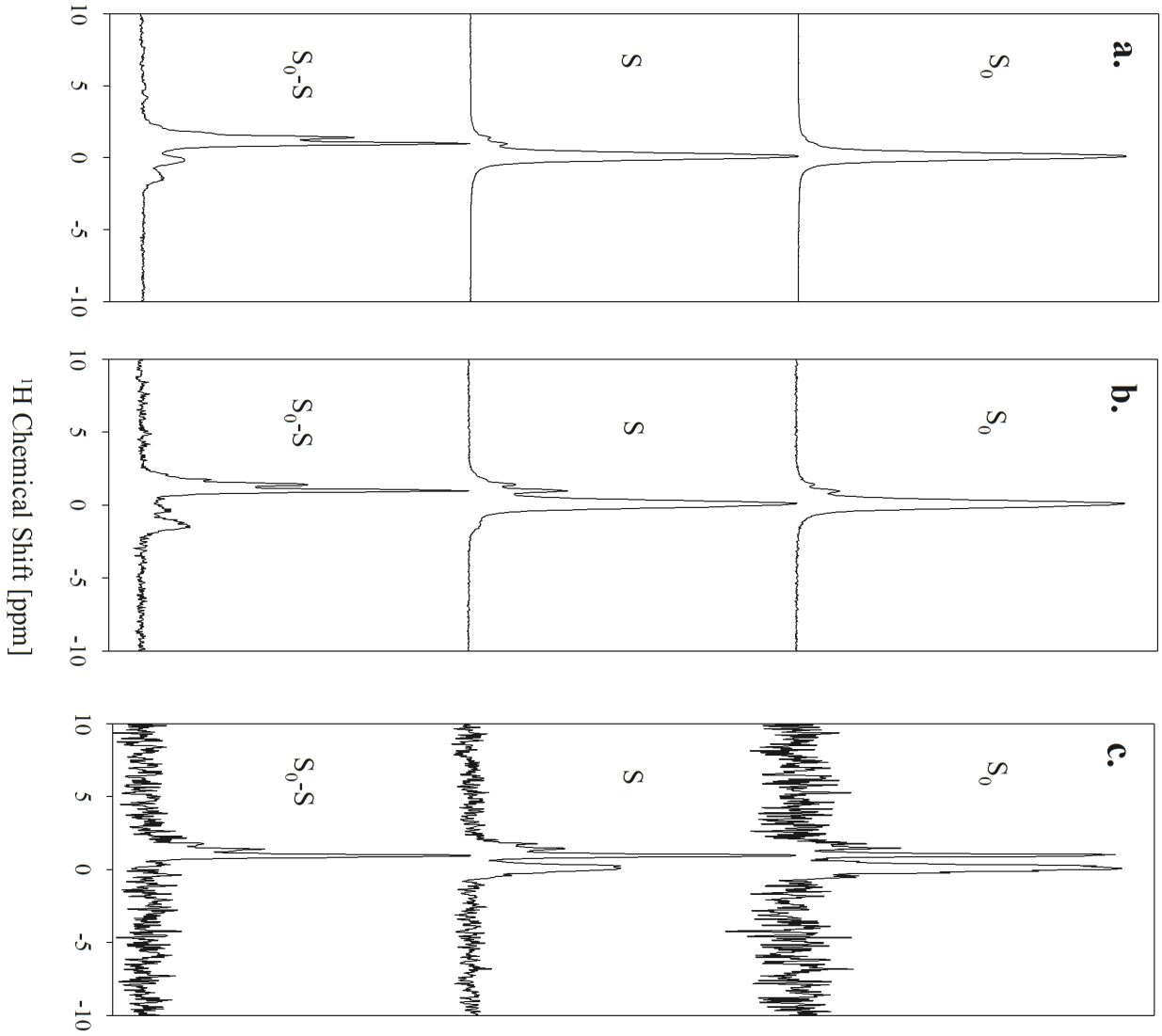

Figure 29: 1H{31P} REDOR spectral sets for 13CHAP-1.43 showing the spin echo (S_0), dephased (S) and difference spectra for dephasing times of a. τ = 8ms b. τ = 16ms and c. τ = 32ms

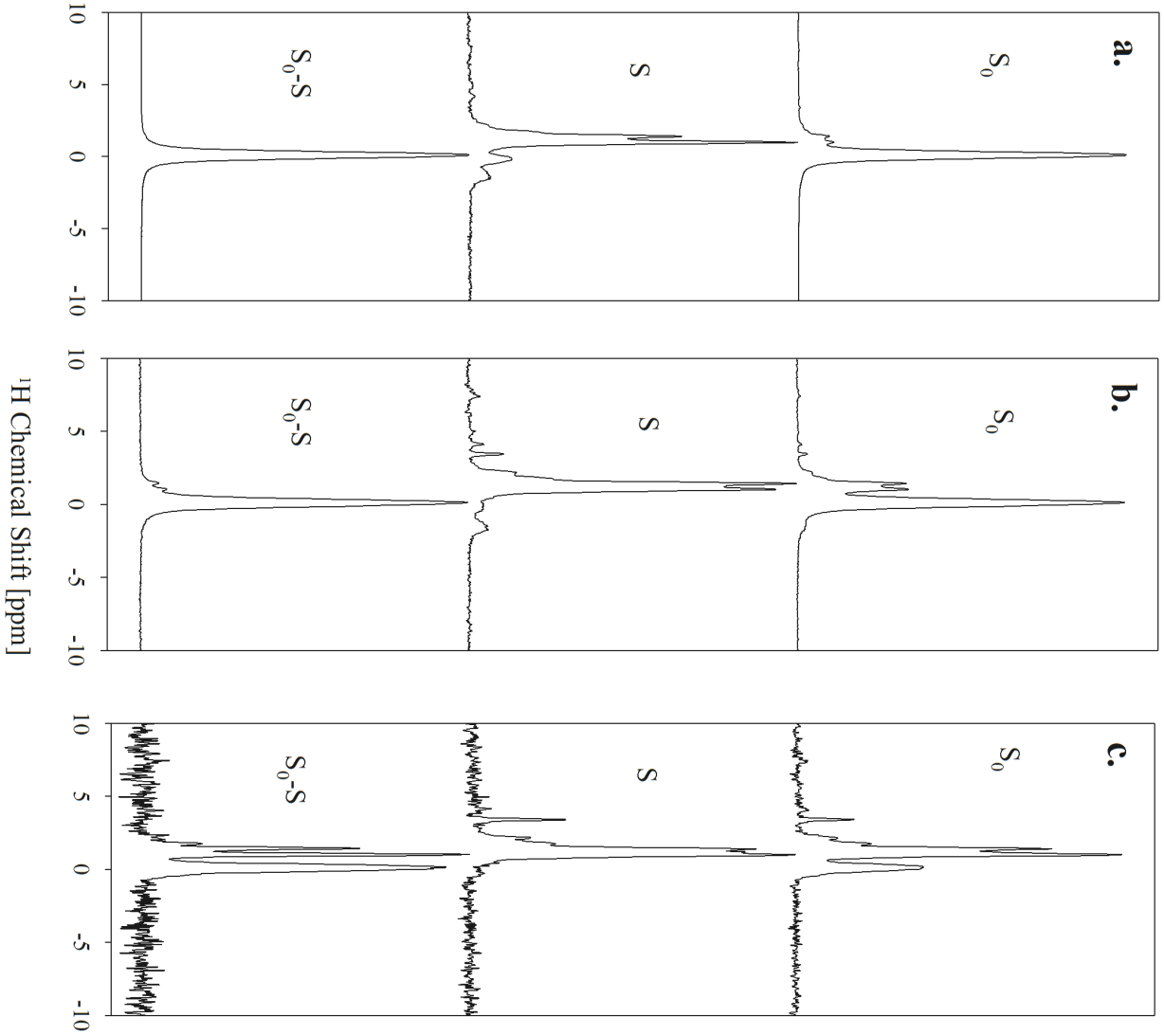

Figure 30: 1H{31P} REDOR spectral sets for 13CHAP-1.67(2x) showing the spin echo (S_0), dephased (S) and difference spectra for dephasing times of a. τ = 8ms b. τ = 16ms and c. τ = 32ms

Analogous to the $^{1}H\{^{13}C\}$ REDOR experiments discussed in the previous section, Figures 27-30 show the spin echo (upper most spectra, S_0), ^{31}P-attenuated spin echo (middle spectra, S), and $^{1}H\{^{31}P\}$ REDOR difference spectra (bottom spectra, S_0-S) for the CHAp samples at dephasing times of 8-32ms. This experiment provides resolution of those ^{1}H sites coupled to ^{31}P from impurity and background ^{1}H, and additionally can provide structural information regarding H-P interatomic distances from data acquired at several dephasing periods.

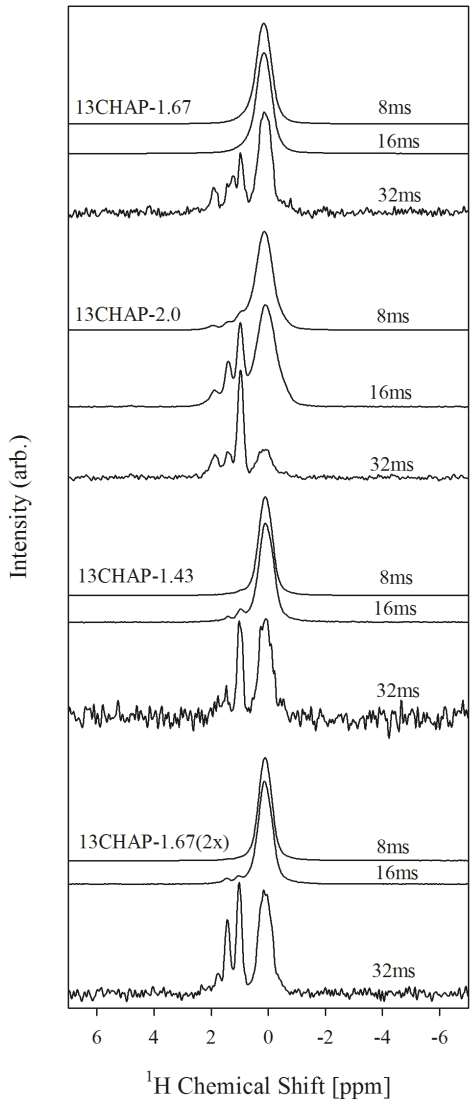

Figure 31: $^{1}H\{^{31}P\}$ REDOR difference NMR spectra. Spectra are the same as those labeled S_0-S in figs. 27-30

^{1}H Chemical	FWHM	$(S_0-S)/S_0$	$(S_0-S)/S_0$	$(S_0-S)/S_0$

Shift (ppm)	(ppm)	τ = 8ms	τ = 16ms	τ = 32ms
13CHAP-1.67				
0.1	0.6	0.133(7)	0.994(5)	0.02(1)
0.9	0.24			0.021(3)
1.3	0.35			0.027(6)
1.9	0.25			0.014(2)
13CHAP-2.0				
0.1	0.7	0.015(6)	0.995(3)	0.018(2)
1.0	0.3	0.007(5)	0.533(4)	0.086(5)
1.4	0.26	0.006(1)	0.77(2)	0.031(9)
2.0	0.4	0.004(5)	0.19(7)	0.041(9)
8.4	0.4	0.015(2)	0.971(6)	0.387(1)
13CHAP-1.43				
0.1	0.55	0.019(1)	0.989(3)	0.007(1)
1	0.3	0.0113(8)	0.703(4)	0.0081(4)
1.4	0.5	0.0050(6)	0.977(2)	0.020(6)
13CHAP-1.67(2x)				
0.1	0.6	0.798(3)	0.19(3)	0.929(3)
1	0.3		0.21(2)	0.312(2)
1.5	0.25		0.9(3)	0.279(2)
1.8	0.2			0.26(1)

Table 9: Results of fitting $^{1}H\{^{31}P\}$ REDOR NMR spectra

The $^{1}H\{^{31}P\}$ REDOR difference spectra collected at various dephasing periods (τ) appear in Figure 31, and the results of fitting these spectra are in Table 9. As in the $^{1}H\{^{13}C\}$ REDOR experiment, the $^{1}H\{^{31}P\}$ REDOR fraction ($(S_0-S)/S_0$) shown in Table 9 represents the amount of ^{1}H signal (S_0) dephased owing to coupling to ^{31}P (S_0-S).

For all samples, the main peak in the $^{1}H\{^{31}P\}$ REDOR difference spectra was best fit using a narrow (FWHM = 0.6 ppm) peak at 0.1 ppm. Two additional signals appear in the difference spectra of all samples, at 0.9 and 1.4 ppm. A peak at ~2 ppm occurs in the spectra of 13CHAP-1.67, 1.43, and 2.0. A difference peak at 8.4 ppm is also observed only for 13CHAP-2.0, at all dephasing periods.

REDOR fraction vs. dephasing period plots for the five ^{1}H NMR resonances that exhibit ^{31}P dephasing are shown in Figure 32. Between 8 ms and 16 ms dephasing periods, it is evident that as the dephasing period is increased, so too does the extent of signal attenuation in the REDOR experiment, giving rise to an increased REDOR fraction in the difference spectra. Between dephasing periods of 16ms and 32ms, however, the REDOR fractions for most signals decline significantly. The signal to noise for spectra collected at 32ms is quite poor, owing to significant T_2 relaxation for all ^{1}H signals. The reported REDOR fractions at 32ms may be reflective of the limitation of the REDOR experiment at extended dephasing periods, or poor rotor synchronization. The magnitude of the 13CHAP-1.67(2x) REDOR fractions do not decline markedly between 16ms and 32ms, only a minor decline is observed for the 0.1 ppm signal, and 0.9 and 1.4 ppm signals increase.

As discussed with the $^{1}H\{^{13}C\}$ REDOR results, the difference peaks at 0.1 and 1.4 ppm are tentatively assigned to channel hydroxyl groups as in stoichiometric hydroxylapatite, and the latter experience a somewhat stronger H-bonding environment. The difference signals at 2.0 and 8.4 ppm do not occur in the $^{1}H\{^{13}C\}$ REDOR spectra, indicating that these difference signals are due to hydrogen bonded ^{1}H environments exclusively associated with phosphate groups, and not carbonate. With the current data it is not possible to rank the ^{1}H signals in the REDOR difference spectra with regard to ^{1}H-^{31}P interatomic distances. There exist too many signals overlapping in the same spectral region, and data were collected at only three dephasing periods, preventing accurate assessment of the rate at which $(S_0\text{-}S/S_0)$ increases with τ. It is clear, however, that the

$^{1}H\{^{31}P\}$ REDOR difference spectra of 13CHAP-2.0 show more resonances at higher chemical shift either with greater intensity, or are detected at shorter dephasing periods than the other three samples, which indicates a greater concentration of the corresponding sites. This result suggests that B-type carbonate substitution, which is presumed to dominate for this sample, may give rise to a complex and varied set of ^{1}H environments. It is worth pointing out however, that these downfield shifts may also arise due to variation in Ca:P molar ratio during synthesis, and not B-type substitution.

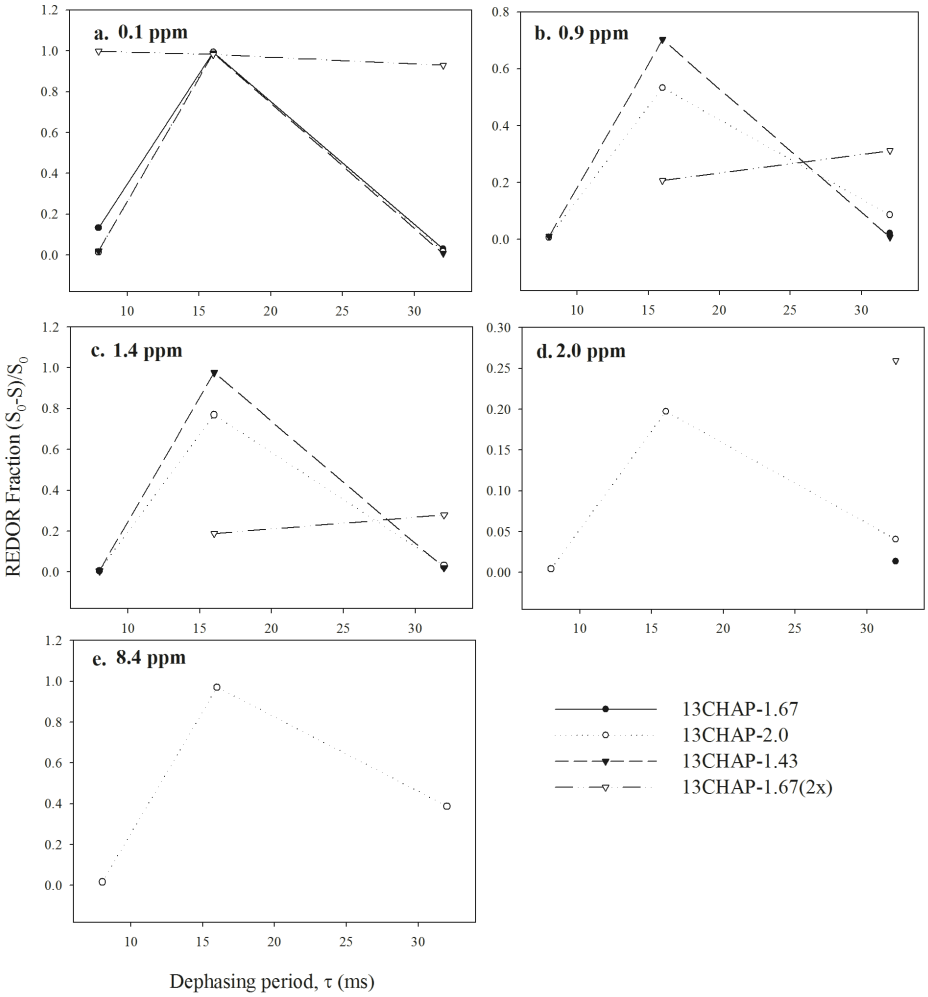

Figure 32: $^{1}H\{^{31}P\}$ REDOR fraction plots of NMR signals

2.5 Discussion

2.5.1 ^{1}H Assignments

^{1}H Chemical Shift (ppm)	^{1}H SP	$^{1}H\{^{13}C\}$ REDOR	$^{1}H\{^{31}P\}$ REDOR	Assignment
0.1-0.3	X	X	X	Channel hydroxyl groups
0.9-1.0			X	H-bonded hydroxyl groups to phosphate
1.1-1.5	X	X	X	H-bonded hydroxyl groups
1.8-2.0			X	H-bonded hydroxyl groups to phosphate
4.1		X		Structural water
5.3-6.4	X			Surface adsorbed water
8.4			X	Strongly H-bonded hydroxyl groups (HPO_4)
13.1-13.4	X			Amorphous calcium hydrogen phosphate
16.1-16.4	X			Amorphous calcium hydrogen phosphate

Table 10: ^{1}H peak assignments from the current work. Crossed-out cells denote observation of a particular signal using the associated NMR experiment

The chemical shifts of ^{1}H resonances observed in this work are shown in Table 10, in addition to assignments for these signals. Two signals are observed in all three (^{1}H single pulse, $^{1}H\{^{13}C\}$ REDOR, $^{1}H\{^{31}P\}$ REDOR) ^{1}H NMR experiments, at 0.1-0.3 ppm, which has been assigned to channel hydroxyl groups, and at 1.1-1.5 ppm, which has also been assigned to hydroxyl groups, however the means by which this peak is shifted to higher chemical shifts is unclear. If the H-C interatomic distances for those ^{1}H signals observed in $^{1}H\{^{13}C\}$ REDOR difference spectra are assumed to be consistent among samples, then it is possible to attribute differences in $^{1}H\{^{13}C\}$ REDOR fractions at a constant dephasing period to relative concentration. The $^{1}H\{^{13}C\}$ REDOR difference spectrum of 13CHAP-2.0 features the greatest REDOR fraction for the signal at 1.1-1.5 ppm, shown in Figure 26b. As noted in both the PXRD and FTIR analysis, the inferred amount of carbonate in the present samples also indicates that 13CHAP-2.0 contains the greatest amount of carbonate, which suggests that this signal may be important to the incorporation of carbonate.

It was proposed by Mason et al.[25] by $^{1}H\{^{13}C\}$ HETCOR analysis (not performed here due to insufficient ^{13}C signal) that ^{1}H signal at 1.3 ppm is associated with ^{13}C giving rise to peaks at δ_C = 169.3 and 170.3 ppm, and is due to a protonated carbonate species. As a result the authors proposed a coupled AB-type substitution mechanism based on protonated carbonate species:

$$Na^{+} + {}^{B}HCO_3^{-} + {}^{A}CO_3^{2-} = Ca^{2+} + PO_4^{3-} + OH^{-}$$

This substitution is based on the presence of sodium, which was observed using ^{23}Na NMR to be included in the apatite phase. As noted by Beshah et al. [37], A-type substitution should result in a ^{13}C signal at 166.5 ppm, which was not observed in the work by Mason et al[25]. The synthesis method utilized in the present work was selected specifically to avoid the use of sodium. Based on the interpretation of FTIR and ^{13}C NMR results the dominant substitution mechanism for 13CHAP-1.67 and 13CHAP-2.0 is believed to be B-type. While it is possible that the ^{1}H peak in the $^{1}H\{^{13}C\}$ REDOR difference spectra at 1.3 ppm is indeed due to a protonated carbonate species in the phosphate site, it is difficult to propose a mechanism of substitution for a protonated carbonate species into the phosphate site without a coupled change in cation valence such Na^{+} for Ca^{2+}. If instead carbonate is present in its unprotonated form, then a coupled substitution involving calcium vacancies is possible, as was described by Pan and Fleet[4]:

$$\square + 2{}^{B}CO_3^{2-} = Ca^{2+} + 2PO_4^{3-}$$

In the above equation charge balance is maintained by the generation of one vacancy in the calcium site and the exchange of two phosphate groups for carbonates. If the vacancy were to occur at the Ca(2) site, the close H-Ca(2) interatomic distance (2.695Å) could

reduce the shielding for the hydroxyl ^{1}H due to proximity to a vacancy. This would have a comparable effect to a hydroxyl group hydrogen bonding to an electronegative element such as F, which would resulting in a greater chemical shift. 13CHAP-2.0 has the highest Ca:P ratio, and the greatest amount of carbonate, observed in the phosphate site. The $^{1}H\{^{13}C\}$ REDOR fraction for the signal at 1.3 ppm is greatest at a given dephasing period for 13CHAP-2.0, suggesting a relationship between the peaks at greater chemical shift and B-type carbonate substitution. The presence of calcium vacancies is further supported by the nonstoichiometric Ca:P ratios measured via ICP, which show the greatest deviation from expected Ca:P for 13CHAP-2.0, shown in Table 2. Additionally, Wilson et al.[39] ascribed diminished Ca occupancies and reduced P-O interatomic distances in hydroxylapatite to Ca vacancies via Rietveld refinement. While this work was focused specifically on non-stoichiometric, carbonate-free hydroxylapatite, the observation of calcium vacancies via Rietveld refinement further strengthens the case for their existence, and offers a potential compensation mechanism for charge balance in carbonate substitutions.

The $^{1}H\{^{13}C\}$ REDOR difference spectrum at τ = 1.5ms of 13CHAP-1.67 clearly shows a signal at 4.1 ppm. There is also a slight bump above the baseline at this position in the difference spectrum at 8ms, however the intensity of this peak is too low to successfully integrate. Yoder et al.[40] described the presence of structural water in its deuterated form using ^{2}H NMR, and noted that the narrow NMR peak width was probably due to thermal motion of water molecules within the apatite anion channel. Unfortunately the effect of thermal motion would also average the heteronuclear dipolar

coupling integral to the REDOR experiment, preventing detection of structural water by this method.

A ^{1}H signal at 8.4 ppm is observed in the $^{1}H\{^{31}P\}$ REDOR difference spectra of 13CHAP-2.0 at all three dephasing periods. Because of the high chemical shift, signal from this site it is clearly resolved from that due to hydroxyl groups in the anion channel. The complete absence of this signal in the spin echo spectra with ^{31}P irradiation (S) for all dephasing periods shown in Figure 28 clearly shows that this site is strongly coupled to ^{31}P. Additionally this signal is clearly visible in the $^{1}H\{^{13}C\}$ REDOR S_0 and S spectra, and not in the difference spectra, providing conclusive evidence that this signal is not coupled to ^{13}C. Yesinowski et al.[33] observed comparable signal at 8.7 ppm in the ^{1}H single-pulse NMR spectra of hydroxylapatite which they assigned to HPO_4 groups, and this assignment provides sufficient explanation for the NMR results observed in the present work. Hydrogen phosphate was not observed in 13CHAP-1.67, which contains a similar amount of carbonate as 13CHAP-2.0, so there appears to be no correlation between this moiety and B-type carbonate substitution.

The ^{1}H SP signals at 13.1-13.4 and 16.1-16.4 in 13CHAP-1.43 and 13CHAP-1.67(2x) are assigned to a poorly crystalline hydrogen phosphate impurity phase. This assignment is further supported by the presence of corresponding ^{31}P signals, at positions consistent with previous reports for hydrogen phosphate. This phase is believed to be poorly crystalline because reflections corresponding to a crystalline monetite are not observed in the PXRD patterns. All PXRD reflections could be indexed to HAp. The absence of these ^{1}H signals in any of the spin echo (S_0) spectra collected during REDOR

experiments indicates short T_2 relaxation constants, possibly owing to coupling to a mobile ^1H reservoir.

2.5.2 A and B-type carbonate substitution

The type of carbonate substitution most closely resembling that of bone mineral is AB-type[32]**.** In order to better understand the nature of the biomineralized HAp, a substantial amount of effort has focused on preparation of apatites containing this type of carbonate substitution. However almost all of these preparations involve the use of sodium or ammonium to generate AB-type CHAP, via the substitution:

$$Na^+ + {}^{B}CO_3^{2-} + {}^{A}CO_3^{2-} = Ca^{2+} + PO_4^{3-} + 2OH^-$$

The mechanism proposed by Mason et al.[25] where the B-type carbonate species is protonated is also a possible mechanism. A closer analogue to bone mineral is an AB-type CHAP without a significant concentration of monovalent cation to facilitate coupled substitution. Such a mechanism was the focus of the synthesis efforts of Gibson and Bonfield[23], wherein a AB-type CHAP was prepared by a two step process: aqueous precipitation of B-type CHAP, followed by sintering at 1100°C under a stream of CO_2 gas, to yield A-type CHAP[19]. It is clear that although this kind of preparation may yield apatite materials of the appropriate composition and carbonate substitution, the methods utilized are not representative of biomineralization. By increasing the amount of phosphate in solution used to precipitate samples as was done in the present work in 13CHAP-1.43, or by increasing the concentration of both calcium and phosphate as in 13CHAP-1.67(2x), we were able to prepare AB-type carbonate apatites using solely room temperature precipitation methods. The total amount of substituted carbonate is clearly lower than 13CHAP-1.67 and 13CHAP-1.43 (shown in Table 4 via Raman

spectroscopy), yet the substitution type appears to be more representative of truly biological apatite. Identification of the substitution type was made possible through the utilization of $^{13}C\{^{1}H\}$ cross-polarization NMR methods, which may be why previous studies employing primarily other characterization techniques such as FTIR failed to clearly indicate this synthetic route.

2.6 Conclusions

Interpretation of the PXRD, FTIR, and $^{13}C\{^{1}H\}$ cross-polarization results indicate that the type of carbonate substitution in 13CHAP-1.67 and 13CHAP-2.0 is B-type. Similarly, these methods (with the exception of PXRD, which suggests A-type substitution) indicate that AB-type carbonate substitution is observed in 13CHAP-1.43 and 13CHAP-1.67(2x), which to the best of our knowledge has not been achieved previously without the use of a monovalent cation or high temperature treatment. Both downfield ^{1}H resonances observed in REDOR experiments and diminished Ca:P ratios indicate that the mechanism of charge compensation for B-type substitution may be the generation of Ca vacancies. The existence of such vacancies has not yet been proven, nor has their role in facilitating charge balance in B-type carbonate substitution. By performing comparable analysis on samples of varied Ca:P ratio without carbonate, we hope to determine whether or not vacancies are a function of bulk chemistry or atomic substitution.

Chapter 3: Hydrogen Environments in Low-H, F,Cl Apatites Revealed by Double Resonance Solid-State NMR

Reproduced with permission from the Journal of Physical Chemistry.
J. Phys. Chem. C. 2015, 119, 28605-28613

3.1 Abstract

A series of hexagonal low H, F,Cl apatite compositions synthesized by high-temperature reaction is characterized by powder x-ray diffraction (PXRD), and various ^{1}H magic-angle spinning (MAS) solid-state NMR methods. Quantitative ^{1}H NMR analysis indicates the ^{1}H content in all samples is low, and is due to OH in apatite. ^{1}H{^{31}P} REDOR NMR difference spectroscopy indicates hydroxyl groups are preferentially oriented towards fluorine, probably due to OH^{-}•••F^{-} hydrogen bonding. Clustered hydroxyl groups are also observed, and may play a significant role in hexagonal solid-solution for ternary F,OH,Cl apatites. From these results a modification of a previous ternary F,OH,Cl column anion sequence is proposed.

3.2 Introduction

Apatite and related materials are important in a wide array of research disciplines, ranging from planetary science[41] to materials science[42] to dentistry.[43] The usefulness of apatite for these and other applications lies in the ability of the apatite structure to accommodate and adapt to substitution in both cation and anion sites.[4] This structural flexibility has given rise to several technological applications for apatite minerals, such as the incorporation of large radionuclide metals into cation sites for nuclear waste remediation,[44] and anionic substitution of a hydroxyl group for fluorine, as a means of enhancing acid resistivity in dental enamel.[10] Many of the atomic-scale

mechanisms by which substitutions occur in the apatite lattice are not completely understood. Understanding these mechanisms is relevant to planetary science because it provides a link between the apatite structure and the geological conditions during crystallization. This work is also critically important in materials science, because it aids in the optimization of current material properties, and in the design of new materials. The response of the apatite structure to atomic substitutions is, in general terms, the primary motivation for this work.

Naturally occurring apatite can be represented chemically as $Ca_5(PO_4)_3(F,OH,Cl)_1$. The anions F^-, OH^- and Cl^- occur in a 1-dimensional channel parallel to the crystallographic c-axis, which is the structural feature that controls anionic solid solution. The position of the anion in this channel is the principal difference between end-member structures, and varies in response to steric effects between column anions and adjacent calcium sites. For larger anions such as Cl^- this effect is significant, leads to anion displacements as large as 1.2 Å from the standard fluorine position, and induces symmetry changes from hexagonal to monoclinic phases.[45] Consequently creation of binary and ternary compositions requires some kind of structural adaptation, such as symmetry breaking, coupled substitution, or the generation of new anion positions.[46] It is likely that structural adaptations would be most critical in solid solutions in which anionic radii and end-member crystallographic positions differ greatest, namely for binary compositions between fluorapatite (r_F = 1.33Å, x, y, z = 0,0,0.25) and chlorapatite (r_{Cl}= 1.81Å, x, y, z = 0,0,0.4323(4)).[45], [47]

To investigate structural relationships along the F,Cl apatite boundary requires samples that are free of hydroxy component. Scientists thus far have had to rely on laboratory synthesis to obtain nearly pure binary F,Cl samples low in OH^-, as even those natural samples initially described as 'OH^- poor' have been shown to contain significant hydroxy component.[41] Exclusion of OH^- from synthetic samples is difficult, because anhydrous synthesis requires exceptionally high temperatures, where atmospheric control is a challenge. Compositional accuracy in binary F,Cl apatite synthesis, specifically exclusion of OH^- to the extent possible and quantitative measurement of its concentration in apatite, is important because the presence of OH^-, even in small amounts, promotes anion distributions that yield average hexagonal symmetry through reversals in crystallographic anion positions.[48],[49] The distribution of OH^- in reversal regimes, the influence of neighboring anion positions, and the minimum concentration of OH^- in which average hexagonal ordering is observed have not yet been investigated completely. Elucidation of OH^- structural environments in near-binary F,Cl apatites would improve our understanding of the types of structural adaptations that can stabilize sterically strained apatite compositions. Characterization and measurement of structural OH^- present at minor concentration in apatite is a challenging task, due to significant contributions from background signals in many spectroscopic techniques arising from sources such as adsorbed water, impurity phases, and materials inherent to the experiment, anisotropic effects in the measurement of fluorine via electron microprobe analysis (EPMA)[50], and difficulty in quantifying the apatite OH stretch in Fourier-transform infrared (FTIR) spectroscopy[51].

Recently, our group provided crystal structure refinements for a synthetic F,Cl apatite prepared with extra care to minimize OH^- component, and comprised of crystals large enough for single-crystal x-ray diffraction (SCXRD). Measurements of OH^- content were performed using both $^{31}P\{^1H\}$ cross-polarization (CP) nuclear magnetic resonance (NMR) and electron microprobe (EMPA) measurements, yielding values of 0.004 and 0.03 mole fraction OH^-, respectively.[52] The refined structure indicates that solid solution and hexagonal ordering is achieved via the occurrence of two previously undescribed crystallographic anion positions for F^- and Cl^- in the average structure, although the distribution of local channel configurations remains unknown. Here, we provide structural data for several apatite compositions along the F,Cl binary in addition to the sample described by Hughes et al.,[52] with particular focus on the concentration and structural environments of OH^-, using powder X-ray diffraction (PXRD) and ^1H MAS NMR. Our results show the hydroxyl groups are preferentially oriented towards fluorine, and that the amount of structural OH^- in these samples is low.

3.3 Materials and Methods

3.3.1 Synthesis

Near-binary fluor-chlorapatite was prepared from mixtures of tricalcium-phosphate, calcium fluoride and calcium chloride at high temperature. Tricalcium phosphate (TCP) was synthesized by high-temperature (1250°C) reaction of calcium carbonate and ammonium phosphate monobasic. The reaction product was determined to be phase-pure by powder x-ray diffraction (PXRD). Anhydrous calcium chloride and calcium fluoride were purchased in sealed ampules from Sigma Aldrich and opened immediately before use. Mixed powders of reagents, adjusted to the proper target

composition, were ground together and loaded into a Pt capsule. The Pt capsule was then inserted into a silica glass tube, and a capillary drawn using an oxygen torch. The sample was subsequently dried under vacuum at 800 °C for 30 minutes, after which the capillary was severed, leaving the Pt capsule sealed under vacuum. The evacuated silica tube + Pt capsule assembly was then heated to 1200°C and reacted for 18 days, yielding clear hexagonal crystals ~10 μm in diameter. Nominal sample compositions are listed in Table 11. Samples are designated F*x*Cl*y*, where *x* and *y* are the mol% of fluor and chlor-apatite component, respectively. End-member compositions are designated F100 and Cl100.

3.3.2 Powder X-ray Diffraction (PXRD)

The powder X-ray diffraction patterns were collected using a Rigaku Ultima IV (Cu Kα radiation) with a D/TeX high speed linear position sensitive detector. The patterns were collected over a range of $10^{o} \leq 2\theta \leq 120^{o}$ with a step size of 0.01° at a rate of 2°/min. Pawley refinements of the lattice were conducted using the program TOPAS (v4.1, Bruker AXS).

3.3.3 ^{1}H Single-Pulse (SP) MAS NMR Spectroscopy

The ^{1}H SP/MAS spectra were collected on a 400 MHz (9.4T) Varian Inova spectrometer operating at 399.895 MHz for ^{1}H. A 4 mm (O.D.) low ^{1}H background probe was used, with ZrO_2 rotors, Kel-F tips, and PTFE spacers. The MAS rate was 10 kHz. For quantitative analysis, the sample volume was divided using a PTFE spacer into two sections; the lower section contained a pectolite secondary intensity standard, selected for its downfield ^{1}H chemical shift and low proton density.[53] The secondary internal intensity standard was calibrated by comparison of signal levels from a series of

hydroxyapatite (HAp)/quartz mixtures of known ratio that occupied the upper rotor section. The standard and samples were confined to the middle third of the standard rotor sample volume. More detailed information regarding the intensity calibration can be found in the electronic supplemental information (ESI). Qualitative ^{1}H single-pulse spectra were obtained by filling the rotor volume completely with sample, omitting the pectolite insert. Qualitative spectra were corrected for background intensity by subtracting an empty rotor spectrum collected under identical acquisition parameters. The 90° pulse width was 5 μs with a pulse delay of 30 seconds, and 2000 transients were collected. A backward linear prediction of 5 FID points was applied to correct baseline artifacts.

3.3.4 $^{1}H\{^{31}P\}$ REDOR NMR Spectroscopy

$^{1}H\{^{31}P\}$ REDOR NMR spectra were collected on a 500 MHz Varian Infinity Plus spectrometer, with operating frequencies 499.786 MHz for ^{1}H and 202.318 MHz for ^{31}P, using a low H-background probe configured with an alumina spinning assembly for 5mm (O.D.) rotors. Spectra were collected at 8 kHz MAS (125 μs rotor period), with a 90° ^{1}H pulse width of 5 μs, and a pulse delay of 2 seconds for approximately 20,000 scans. Application of 180° pulses to ^{31}P (10 μs) every half-rotor period for 2 ms was sufficient to attenuate signal due to ^{1}H sites coupled to ^{31}P. Total integrated intensities were determined from the first point in the phase-corrected FID, and corrected for background using the signal from an empty rotor.

3.4 Results

3.4.1 Powder X-ray Diffraction (PXRD)

Table 11 shows the refined lattice parameters for the seven fluor-chlorapatite samples determined using Pawley refinement. It is well known that increasing Cl content along the F,Cl apatite binary results in expansion of the a_1-a_2 dimensions, and a concurrent reduction in the *c*-axis.[46] The present results, shown in Figure 33, depict the same trend. Because the a_1-a_2 lattice dimensions expand with increased Cl content, despite the fact that the *c* unit cell dimension decreases with increasing Cl content, the net effect is an increase in the unit cell volume, as shown in Figure 34. The exception to this trend is in the *c* parameter near the F-endmember, which is slightly larger for F90Cl10 than F100. There is no current explanation for this minor deviation from ideal solid solution. The lattice parameters reported are in reasonable agreement with previous findings by Mackie and Young[54], and Schettler[55], shown in Figure 35. The results reported by Schettler[55] define a trend of unit cell volumes consistently larger than determined in the present study, with the exception of those compositions near the Cl-endmember. The unit cell volumes of Cl-rich compositions reported by Schettler are comparable to the volumes reported in this work. The authors proposed that the unit cell volume of those compositions near the Cl-endmember deviate from the linear trend due to the formation of oxyapatite component, which would theoretically reduce the average lattice parameters of a F,Cl apatite composition. Thus far oxyapatite has only been observed in apatites composed of atoms with larger ionic radii such as Sr^{2+},[56] I^-,[57] and various rare-earth elements.[42] The current samples were synthesized under vacuum, and the variation of unit cell parameters with composition was not observed to

deviate significantly from linearity. We conclude that oxyapatite is most likely not present in the samples described in this work.

Sample	Target Composition	a (Å)	c (Å)	Vol (Å^3)	χ^2	wRp
F100	$Ca_5(PO_4)_3F$	9.365042(21)	6.875966(19)	522.2564(27)	1.31	0.0533
F90Cl10	$Ca_5(PO_4)_3F_{0.9}Cl_{0.1}$	9.395387(19)	6.876913(19)	525.7189(26)	1.24	0.051
F67Cl33	$Ca_5(PO_4)_3F_{0.67}Cl_{0.33}$	9.457202(35)	6.846911(19)	530.3354(42)	1.3	0.0524
F50Cl50[(a)]	$Ca_5(PO_4)_3F_{0.5}Cl_{0.5}$	9.505327(24)	6.829141(21)	534.3562(31)	1.19	0.0483
F33Cl67	$Ca_5(PO_4)_3F_{0.33}Cl_{0.67}$	9.54126(36)	6.810291(29)	536.9177(46)	1.23	0.0495
F10Cl90	$Ca_5(PO_4)_3F_{0.1}Cl_{0.9}$	9.620194(70)	6.779728(60)	543.3886(93)	1.38	0.0381
Cl100	$Ca_5(PO_4)_3Cl$	9.6450561(30)	6.763683(23)	544.9088(38)	1.24	0.0511

Table 11: Refined lattice parameters of F,Cl apatites. Uncertainties in parenthesis are for the last reported digit. (a) F50Cl50 composition used in Hughes et al., 2014.

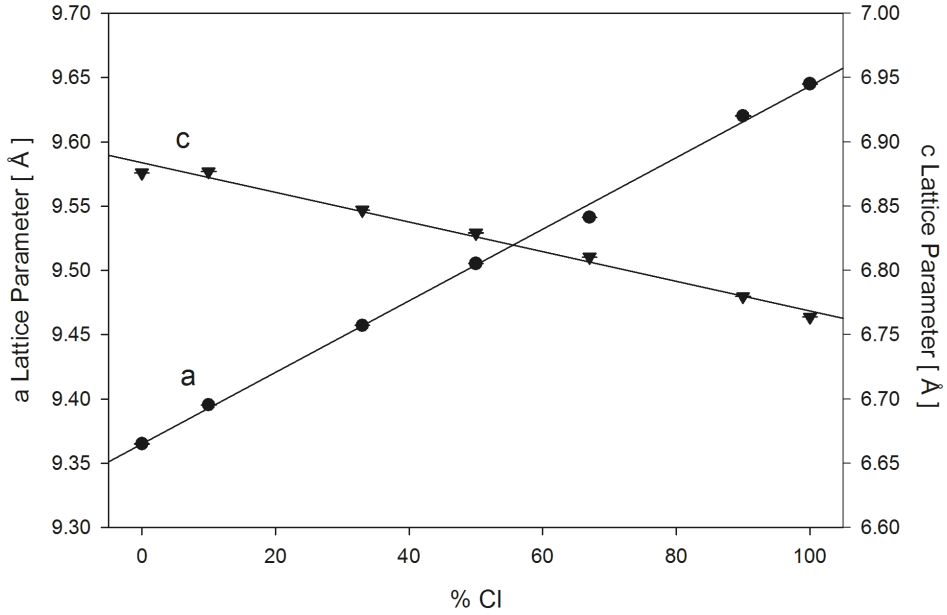

Figure 33: Variation in lattice parameters a and c as a function of chlorine content. Uncertainties are smaller than symbol size.

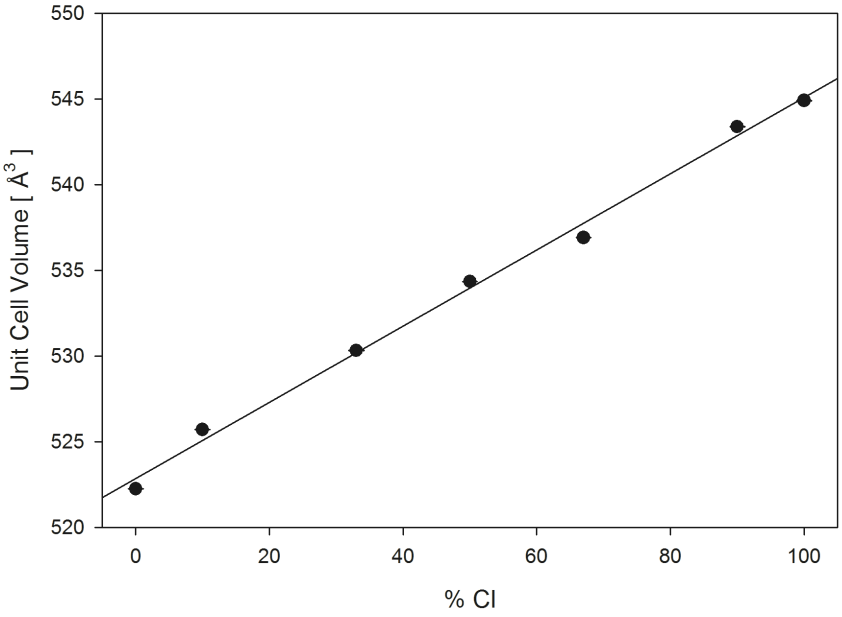

Figure 34: Variation in unit cell volume as a function of chlorine content. Uncertainties are smaller than symbol size.

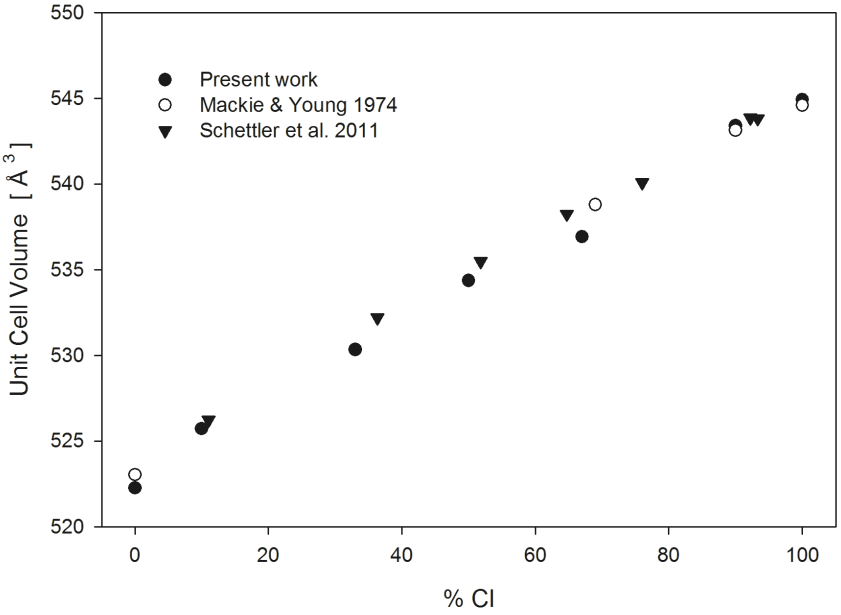

Figure 35: Variation of unit cell volume with chlorine content for binary F,Cl apatites reported previously compared to that of the present study.

3.4.2 ^{1}H Single-Pulse (SP) MAS NMR Spectroscopy

^{1}H single-pulse (SP) spectra of the F/Cl apatites analyzed in this work are shown in Figure 36. These spectra were background corrected by subtracting signal due to an

empty NMR rotor. For all samples the spectral profiles are broad (FWHM ~11 ppm) and complex, due to multiple sources of ^{1}H signal such as background from rotor and probe materials, surface-adsorbed water, and structural ^{1}H. Two distinct signals are observed: a broad component at $\delta \approx +6$ ppm believed to arise from surface-adsorbed water,[33] and a narrow component at $\delta \approx +2.3$ ppm, which remains unassigned. Signal due to structural ^{1}H cannot be identified in these spectra owing to strong overlapping intensity of these signals, and the minor to trace amounts of structural ^{1}H presumed to be present.

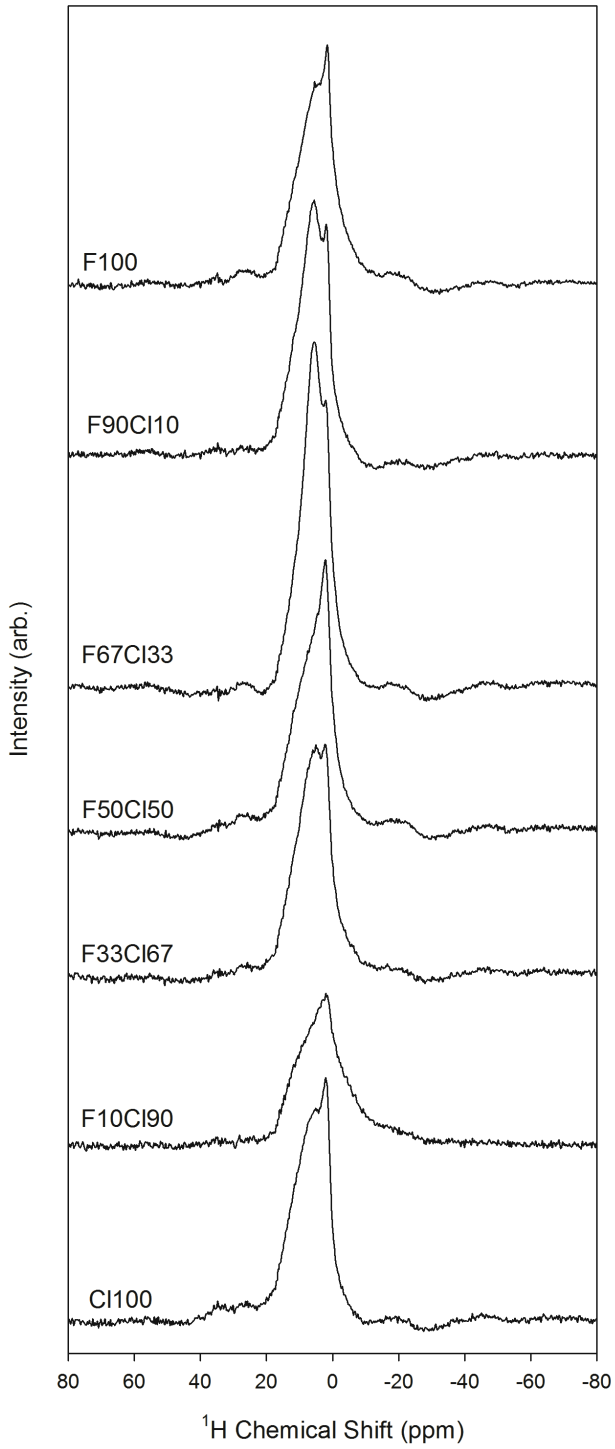

Figure 36: Background-corrected 1H Single-Pulse (SP) Spectra of F,Cl apatites.

3.4.3 $^{1}H\{^{31}P\}$ REDOR NMR Spectroscopy

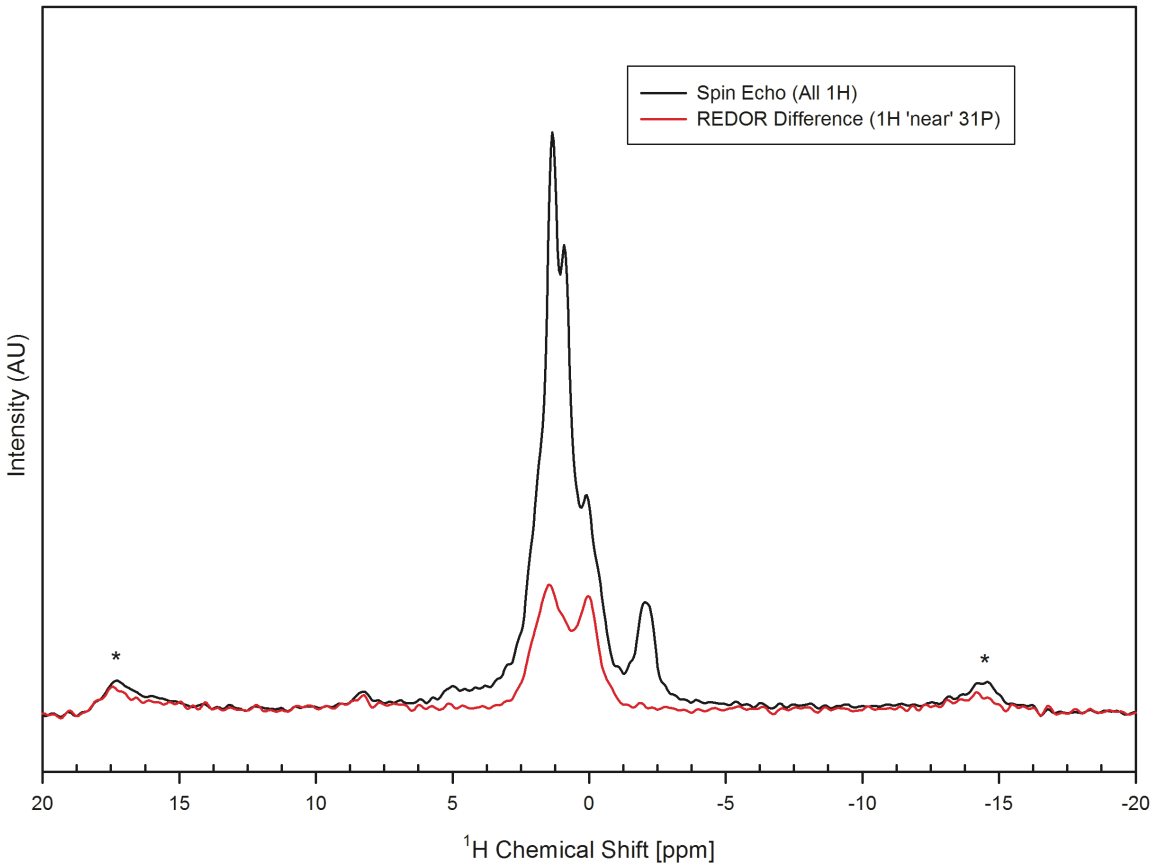

Figure 37: $^{1}H\{^{31}P\}$ REDOR Results from F50Cl50. In black: Spin echo spectrum, showing all 1H. In red: REDOR difference spectrum, showing only 1H within a few Å of 31P. Asterisks denote spinning side bands (SSBs).

To identify signal arising from apatite structural H we have employed ^{1}H-observe, ^{31}P dephased rotational echo double resonance ($^{1}H\{^{31}P\}$REDOR) experiments. The $^{1}H\{^{31}P\}$ REDOR experiment enables quantification of OH component in apatite by resolving structural sources of ^{1}H from other potential sources of ^{1}H signal, such as background from probe and rotor materials, impurities, or adsorbed water. The REDOR experiment also provides information regarding the local ^{1}H environments as the

composition is modified, manifested as the ^{1}H chemical shift. Figure 37 illustrates the key elements of the REDOR experiment: in black is the ^{1}H spin echo spectrum of F50Cl50, which contains signal from all the H in the sample, including a significant component due to background sources of ^{1}H typical of ^{1}H MAS NMR spectra. In red is the REDOR difference spectrum, obtained by subtracting from the ^{1}H spin echo spectrum a similar spectrum in which the signal due to ^{1}H proximal to ^{31}P has been eliminated by irradiation of the ^{31}P nucleus during the echo sequence. Subtracting this dephased spectrum from the spin echo yields the REDOR difference spectrum, which contains signal only from H within atomic-scale proximity to P nuclei in this case structural H in apatite. The amount of ^{1}H signal believed to be due to structural apatite ^{1}H relative to the total signal is shown in the third column of table 2, labeled %Hap from REDOR.

Sample	^{1}H Signal: Sample mass[(a)]	% HAp from REDOR[(b)]	Mole fraction OH[(c)]
F100	0.0147(3)	25	0.0052(2)
F90Cl10	0.018(1)	40	0.007(1)
F67Cl33	0.022(1)	43	0.012(1)
F50Cl50	0.015(2)	51	0.011(2)
F33Cl67	0.014(1)	31	0.004(1)
F10Cl90	0.0139(7)	31	0.0034(7)
Cl100	0.023(1)	61	0.019(2)

Table 12: Determination of OH component using ^{1}H NMR. (a) Ratio of total ^{1}H signal to sample mass in rotor. (b) Percentage of total ^{1}H signal due to apatitic ^{1}H, determined using $^{1}H\{^{31}P\}$ REDOR. Percentages are reported to the nearest integer to compensate for variation inherent to the experiment such as amplifier fluctuations and probe detuning. (c) Mole fraction OH component, determined using quantitative ^{1}H SP/MAS results and $^{1}H\{^{31}P\}$ REDOR.

The results of quantitative ^{1}H NMR analysis of structural ^{1}H are shown in Table 12. The second column, labeled ^{1}H Signal: Sample mass, shows the total amount of ^{1}H signal measured relative to the sample mass in the NMR rotor. In addition to the results from $^{1}H\{^{31}P\}$ REDOR spectroscopy, these data were used in calculating the mole fraction of OH, shown in right-most column of Table 12. The results indicate that despite the precautionary steps taken to eliminate formation of OH-component and obtain true

binary F/Cl apatite, some OH component persists. Chlorapatite contains the highest concentration of structural OH of all samples, a OH mole fraction of 0.019. The OH fraction reported here for F50Cl50 is comparable to those values obtained previously via EMPA and $^{31}P\{^{1}H\}$ CP/SP MAS NMR analysis.[52] It is believed that the value reported here is more representative of true apatite OH content, as it was determined from intensity measured from OH groups directly. It is important to point out, however, that the amount of OH-component is low (mole fraction OH < 0.02), representing a minor component for all samples, with no systematic trend with F/Cl content.

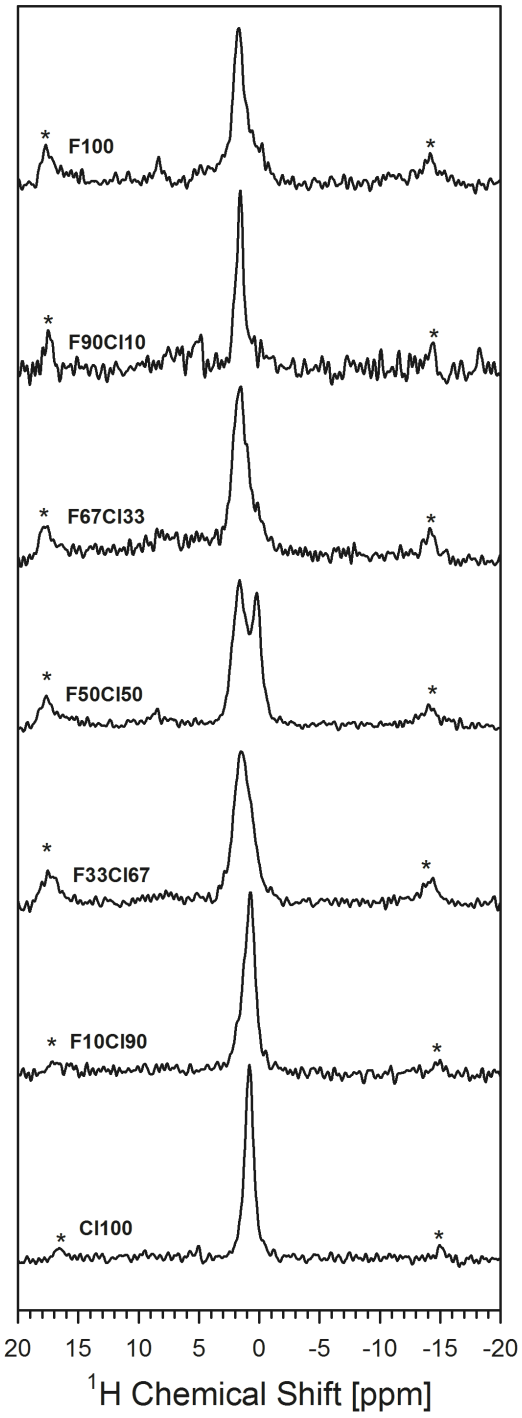

Figure 38: $^{1}H\{^{31}P\}$ REDOR Difference Spectra of F-Cl apatite samples, as indicated. Asterisks denote spinning side bands (SSBs).

The $^{1}H\{^{31}P\}$ REDOR difference spectra contain prominent peaks in the range +1.8 to 0.2 ppm with associated spinning sidebands. These resonances occur in the chemical shift range previously reported for hydroxyl groups in apatite[33]. In addition, some samples appear to show features in the range 5-7 ppm that could arise from additional environments, such as structural water[53], but in all cases the spectral intensity for these features rises insufficiently above noise to attribute with confidence to additional H environments. The $^{1}H\{^{31}P\}$ REDOR difference spectra for the F,Cl apatites investigated in this work are shown in Figure 38. These spectra contain signal from only the ^{1}H environments within the apatite structure located within atomic scale distances to phosphorus atoms. Much more structural information about those ^{1}H environments in apatite than the ^{1}H single-pulse spectra can be observed in these spectra, shown in Figure 36. This is due to the fact that the $^{1}H\{^{31}P\}$ REDOR experiment eliminates sources of ^{1}H signal not coupled to a phosphorus-bearing phase.

For F100 and F90Cl10 the difference spectrum features a single, well-resolved narrow (~ 0.8 ppm FWHM) peak at δ = +1.8 ppm. The peak for F67Cl33 is broader (FWHM = 1.4 ppm) than that for F100 and F90Cl10, and centered at δ = +1.7 ppm with some trailing intensity towards smaller chemical shifts. The $^{1}H\{^{31}P\}$ REDOR difference spectrum of F50Cl50 contains two overlapping peaks, a broad (FWHM = 1.4 ppm), asymmetric resonance at δ = +1.6 ppm and a narrower (FWHM = 1 ppm) resonance at δ = +0.2 ppm. A single broad (FWHM = 1.6 ppm) resonance at δ = +1.7 ppm is observed in the $^{1}H\{^{31}P\}$ REDOR difference spectrum of F33Cl67. The peak shape is asymmetric with some intensity towards smaller chemical shifts. The width of the peak at δ = +0.8 ppm in the F10Cl90 spectrum is significantly narrower (FWHM = 1.1 ppm) than that of

F33Cl67, and has some trailing intensity towards higher chemical shifts. The single peak in the spectrum of Cl100 is narrow, symmetric, and also exhibits a chemical shift of δ = +0.8 ppm.

These results are summarized in Table 13 and indicate a general trend in which the observed peak widths are narrow for end-members, and become progressively broader for intermediate compositions. The ^{1}H chemical shifts in these spectra become smaller as the chlorine content increases, with the exception of the second peak at 0.2 ppm, observed for F50Cl50.

Composition	Chemical Shift [ppm]	Peak Width (FWHM)
F100	1.8	0.8 ppm
F90Cl10	1.8	0.8 ppm
F67Cl33	1.7	1.4 ppm
F50Cl50	1.7; 0.2	1.4; 1 ppm
F33Cl67	1.7	1.6 ppm
F10Cl90	0.8	1.1 ppm
Cl100	0.8	0.8 ppm

Table 13: ^{1}H chemical shifts and peak widths for apatites determined via ^{1}H{^{31}P} REDOR difference spectroscopy

3.5 Discussion

3.5.1 Comparison of refined lattice parameters to previous efforts

The correspondence between the lattice parameters reported here and those reported previously[54], [55] is surprising in light of the fact that those studies utilized an open-atmosphere flux growth synthesis method developed by Prener[58], which could permit incorporation of OH-component from atmospheric water vapor. It is possible that the concentration of OH component in the present samples is too low to significantly affect the average structure parameters.

McCubbin et al.[48] determined by EMPA that a binary F,Cl apatite with a target composition of F50Cl50 crystallized as F50Cl37OH13. This observation suggests substitution of OH component excludes Cl over F, and effectively increases the F:Cl ratio. Assuming linear end-member mixing, incorporation of OH component and exclusion of Cl would result in a smaller unit cell volume than a true 'OH-free' binary F,Cl sample. Although the F50Cl50 sample discussed in the present work is not free of OH, the concentration is significantly lower than that described by McCubbin et al. (EMPA mole fraction OH = 0.03 vs. 0.13). The lower OH content is reflected in the larger unit cell volume of the present sample (534.4 vs. 527.6 $Å^3$ in McCubbin et al.). However, it is important to emphasize that the difference in unit cell volumes is somewhat exaggerated, as a Cl/OH substitution of a mole fraction = 0.13 in F,Cl apatite (i.e. F50Cl37OH13 instead of F50Cl50) should (assuming linear end-member mixing) result in a unit cell volume roughly two $Å^3$ smaller than an ideal F50Cl50 composition, not roughly six $Å^3$ as was observed experimentally. The OH concentration must be substantial to significantly alter the lattice parameters, which may explain why the lattice parameters reported in the present work correspond well with those[54], [55] synthesized using an open air flux synthesis.[58]

3.5.2 Quantitative measurements of OH in apatite and the utility of ^1H NMR

Several methods have been developed to investigate the amount of OH-component in F,Cl apatites, the most prominent being Fourier-transform infrared spectroscopy (FTIR) and electron microprobe analysis (EMPA). Quantification of the OH-stretch in FTIR spectra requires special orientation of individual grains[51], which is not experimentally feasible for the small grains obtained in this work. Quantifying FTIR

intensity also requires calculation of the coefficient of molar absorptivity, dependent on both sample thickness and composition.[59] The amount of OH component cannot be determined by EMPA directly. Instead F and Cl concentrations are measured,[41] and OH content is calculated by difference, assuming F + Cl + OH = 1 apfu. For the present study we employed a ^{1}H NMR method capable of measuring OH content directly, and suitable for fine-grained powders such as those obtained in this work. The method also distinguishes apatite OH groups from other sources of H, such as background from probe and rotor materials, impurities, or adsorbed water. Comparison of the OH concentration in apatite determined via ^{1}H NMR to the EMPA results of previous workers is difficult, as the data reported here reflect OH content by direct measurement, whereas values reported by others have been determined by difference, which neglects contributions due to column vacancies and a postulated oxyapatite component.[55] EMPA data are available for only one F/Cl composition discussed here, F50Cl50, analyzed in part of a previous contribution, by difference from EMPA-measured F^- and Cl^- content.[52] The OH^- content determined directly by ^{1}H NMR is comparable within experimental uncertainty to that determined by difference using EMPA, mole fraction of OH^- = 0.011(2) via ^{1}H NMR vs. 0.03(5) via EMPA.

3.5.3 OH structural environments in F,Cl Apatite

Careful ^{1}H SP/MAS NMR chemical shift analysis of F,OH apatites by Yesinowski and Eckert[33] revealed that the ^{1}H chemical shift is affected principally by hydrogen bonding between hydroxyl proton and the two adjacent anion positions. For a hydroxyl group oriented vertically in the apatite anion channel with the O-H internuclear vector pointing downward, the proton chemical shift is affected by the occupants of the

two column anions sites below. The authors posited that if the hydrogen bonding between OH and the adjacent anion site is strong, the hydroxyl proton exhibits a larger ^{1}H chemical shift. The second nearest anion site can affect the ability of the adjacent anion to serve as a hydrogen bond acceptor, and indirectly change the ^{1}H chemical shift.

A relationship between hydrogen bonding and the ^{1}H chemical shift similar to that reported in F,OH apatites also appears to be observed in the present study. When the fluorine sites adjacent to OH are replaced by chlorine atoms (moving from the F100 composition to the Cl100 composition), the hydrogen bonding between the hydroxyl group and these anion sites is decreased, which results in a smaller ^{1}H chemical shift. If the anion sites adjacent to hydroxyl protons were indiscriminately occupied, the ^{1}H chemical shifts would systematically change from larger values for fluorine-rich samples to smaller values for chlorine rich samples. However, the chemical shifts do not vary linearly with composition. The fluorine rich samples (F100 and F90Cl10) exhibit the same chemical shift, at δ = +1.8 ppm, probably due to OH*-F-F sequences. The chlorine rich samples (Cl100 and F10Cl90) also have identical chemical shift values of δ = +0.8 ppm, assigned to OH*-Cl-Cl anion arrangements. The asymmetry observed in the peak in the spectrum of F10Cl90 is probably due to hydroxyl groups proximal to fluorine. The intermediate samples (F67Cl33, F50Cl50, F33Cl67) have broad, asymmetric signals centered at δ = +1.7 ppm. The similarity of these chemical shifts to those of the fluorine rich samples suggests that most OH preferentially forms OH*-F arrangements over OH*-Cl. This observation may indicate that OH•••F hydrogen bonding in the anion channel lends stability to the overall structure, possibly due to reduced anion-anion distances as a result of this interatomic attraction. Only in very Cl rich compositions is the majority of

OH observed proximal to chlorine, as observed in F10Cl90 and Cl100. The broad peak width at intermediate composition can be attributed to inability to resolve OH*-F-Cl from OH*-F-F arrangements. Likewise, the asymmetry towards higher chemical shift for F10Cl90 can be attributed to presence of unresolved OH*-Cl-Cl and OH*-Cl-F with perhaps a small fraction of OH*-F-Cl represented by the tail of intensity toward this chemical shift. The peak at δ = +0.2 ppm in F50Cl50 is assigned to clustered OH*-OH-OH regimes, as in end-member hydroxyapatite.[33] It cannot be ascertained from these data whether the apparently clustered OH environments in F50Cl50 occur within the F/Cl apatite or as a separate hydroxylapatite phase.

Hughes et al. [49] proposed a mechanism of maintaining hexagonal symmetry in solid solutions of ternary F,OH,Cl apatite involving column reversals that feature a fluorine atom in the center of the reversal sequence, and chlorine atoms and hydroxyl groups positioned above and below in the sequence Cl-Cl-OH-F-HO-Cl-Cl, shown in Figure 39a. In such local arrangements the hydroxyl protons are pointed towards the single fluorine atom. As discussed previously, the ^{1}H chemical shift in apatite is sensitive only to those anion positions below the hydroxyl proton, so the presence of chlorine atoms positioned adjacent to the hydroxyl oxygen, as proposed in the work by Hughes et al.,[49] would not be expected to have a large effect on the ^{1}H chemical shift. A similar arrangement could occur in the present samples, and could explain why OH*-F sequences are dominant in a Cl-rich apatite composition (F33Cl67). The present results suggest two modifications to Hughes' original ternary. First, because hydroxyl groups were observed to occur primarily in OH*-F-F,Cl environments, there are probably at least two halogen atoms in the column reversal sequence, not one, such as illustrated in Figure

39b. Hydroxyl groups in the OH*-F-HO arrangements proposed by Hughes et al.[49] would give chemical shifts of δ = +1.2 ppm,[33] but were not observed in a significant concentration. Additionally, evidence for the presence of clustered hydroxyl groups was observed in the spectrum of F50Cl50, so there may be OH*-OH-OH in the reversal sequence for compositions near F50Cl50. A specific arrangement that features clustered hydroxyl groups in which OH*-F-HO regimes (δ = +1.2 ppm) are not present is difficult to propose. It is possible that NMR signal due to OH*-F-HO is present, but was not observed due to overlapping intensity from the broad signal at δ = +1.7 ppm. It is also possible that this ^{1}H NMR signal is due to a separate phase of hydroxyapatite, and was not detected via PXRD analysis due to the low concentration of the phase.

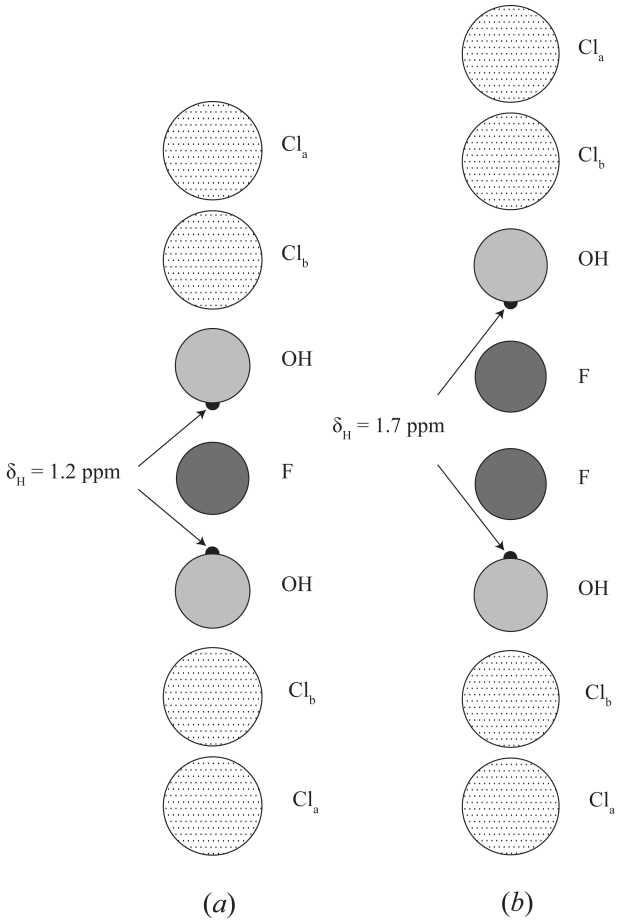

Figure 39(a): Anion column reversal sequence proposed by Hughes et al. [49] and (b) Anion column reversal sequence modified to comport with $^{1}H\{^{31}P\}$ REDOR NMR results

3.6 Conclusions

The work by Yesinowski and Eckert[33] illustrates that ^{1}H NMR is a very sensitive tool for illuminating structural environments in F,OH apatites. Here, this analysis is extended to low-OH F,Cl apatites, through the implementation of double resonance NMR, specifically $^{1}H\{^{31}P\}$ REDOR difference spectroscopy. This analysis shows the ^{1}H chemical shift is affected more strongly by fluorine than chlorine, and that protons in columnar hydroxyl groups are preferentially oriented toward fluorine, even in Cl-rich compositions. These results suggest OH groups hydrogen bonded to fluorine atoms may play a central role in the formation of column reversals in ternary apatite, and

that in general, hexagonal solid solution and column anion arrangements in apatite are affected strongly by interactions between adjacent column anions. A fundamental understanding of the arrangements and bonding of atoms in minerals such as apatite is useful for both the geoscience and materials science communities.

Clustered hydroxyl groups are observed in one F,Cl composition, F50Cl50, however it is not currently known how hydroxyl groups may facilitate column reversal arrangements and allow solid solution, or if the hydroxyapatite-like environments occur in a separate OH-rich phase. Future ^{1}H NMR characterization of ternary F,Cl,OH samples with higher OH content should elucidate the prevalence and dependence of clustered OH on the arrangement of column anions and solid solution.

Chapter 4: Apatite solid-solution along the F,Cl binary investigated using multinuclear solid-state NMR methods

4.1 Abstract

A set of synthetic low-H, F,Cl apatites was investigated using ^{31}P, ^{19}F, and ^{35}Cl solid-state magic angle spinning (MAS) NMR spectroscopic methods. ^{31}P single-pulse (SP) NMR spectra show that phosphate groups experience minor ^{31}P chemical shift deviations from linear behavior as fluorine-rich compositions become chlorine-rich. ^{19}F SP NMR spectra reveal complex, broadened spectral profiles, and are not correlated to composition. $^{19}F\{^{35}Cl\}$ TRAPDOR indicates that the spectral profiles are not due to distinct ^{19}F-^{35}Cl distances, and we propose that the complex ^{19}F lineshapes are principally due to variation in ^{19}F-Ca distance. Approximate fluorine atomic positions are calculated based on ^{19}F chemical shifts of alkaline earth fluoride salts, and the results are in good accord with those proposed for F,Cl apatites from XRD data.

4.2 Introduction

Apatite ($Ca_5(PO_4)_3X$, where X = F, OH, or Cl) is an important mineral group for scientists in fields ranging from earth and space sciences to biomaterials and medicine. Much research is focused on chemical composition and crystal structure, as these molecular-scale properties are related to physical observables such as mechanical strength or biocompatibility[60]. In the geological realm chemical analysis of apatite provides insight into the volatile content in magmas, which is associated with magma explosivity[1]. Changes in apatite composition or structure often have significant impacts on physical or chemical properties, spawning a great deal of interest in this field.

The most remarkable feature regarding the apatite crystal structure is its ability to accommodate cations and anions of broadly different sizes. As a result apatites have been utilized in technological fields such as nuclear waste storage[44] and as electrolytes in solid oxide fuel cells[42]. The molecular-scale mechanisms by which substituents of varying size and charge are incorporated into the apatite structure are poorly understood, but are of great fundamental importance to geoscientists and materials scientists, as they can provide clues into the geological conditions of crystallization, and suggest pathways for the preparation of novel materials with desirable properties. The current work focuses specifically on structural adaptations related to anion substitutions between fluorine, chlorine, and hydroxyl groups.

The monovalent anions in naturally occurring apatite (F^-, OH^-, and Cl^-) occupy a 1-dimensional channel parallel to the crystallographic *c*-axis. Solid solution among end-members is controlled by the sequence and atomic positions of anions in this channel. The 'walls' of the channel are composed of Ca2 triads that define a plane orthogonal to the *c*-axis, positioned at $z = 0.25$ and 0.75. The positions of column anions are often described relative to these triads. The fluoride ion in fluorapatite is centered within the Ca2 triads consistent with crystallographic mirror planes observed parallel to the *a*-*b* plane. The presence of mirror planes bisecting the fluorine and three Ca positions indicates that the crystal system is hexagonal. Hydroxyl groups and chloride ions are too large to occupy the fluorine position in fluorapatite due to steric constraints from the triad of Ca2 atoms, and are displaced in end-member compositions 0.35Å and 1.3Å above or below the Ca2 triads for hydroxylapatite and chlorapatite, respectively. Average

hexagonal symmetry is achieved for end-member hydroxlapatite and chlorapatite by a balanced distribution of anion occupancies above and below the Ca2 triad. As a consequence of greatly varying end-member column anion positions, combining end-member structures to create single-phase binary (F,OH; F,Cl; OH,Cl) and ternary (F,OH,Cl) apatite compositions results in unacceptably small interatomic anion distances. Therefore, the generation of binary and ternary apatite compositions requires a structural adaptation of some kind (e.g. a reduction in symmetry from hexagonal to monoclinic, thereby lifting restraints on possible column anion positions, or the generation of new anion positions that preserve hexagonal symmetry).

Previously we have described a series of apatite compositions very close to the F-Cl binary, wherein dilute hydroxyl groups were shown to play an important role in occupying positions at the interface between fluorine and chlorine atoms[61]. However, the concentration of hydroxyl groups was low (< 2 mol percent), so only a minor fraction of fluorine/chlorine arrangements could feature hydroxyl groups at the interface. The present work focuses on the F-Cl binary because disparate end-member anion positions would likely induce prominent structural adaptations, which could more easily permit observation of the adaptation mechanism. In this work, we apply ^{19}F, ^{31}P and ^{35}Cl NMR methods to this same set of near binary F,Cl samples examined in Ch.3 [61], in order to explore the arrangement of major column anions. ^{31}P NMR spectra indicate that phosphate groups in apatite are sensitive to the identity of the nearest anion column occupant, but not to the F/Cl arrangement. ^{19}F NMR spectra show that changes in fluorine environments with composition are complex and vary non-linearly as chlorine

content is increased. The complex ^{19}F line shapes likely reflects a distribution of F-Ca2 distances, indicating that the fluorine atoms are disordered in the anion channel.

4.3 Materials and Methods

4.3.1 Apatite Synthesis

Preparation of the present samples has been described previously [61], but is summarized here for completeness. Near-binary fluor-chlorapatite was prepared from mixtures of tricalcium-phosphate, calcium fluoride (99.99%, Alfa Aesar), and calcium chloride (99.99%, Alfa Aesar) at high temperature. Tricalcium phosphate (TCP) was synthesized by high-temperature (1250 °C) reaction of calcium carbonate (99.5%, Alfa Aesar) and ammonium phosphate monobasic (98+%, Sigma-Aldrich). The reaction product was determined to be phase-pure by powder X-Ray diffraction (PXRD). Anhydrous calcium chloride and calcium fluoride were purchased in sealed ampules and opened immediately before use. Mixed powders of reagents, in proportion to the desired target composition, were ground together and loaded into a Pt capsule. The Pt capsule was then inserted into a silica glass tube, and a capillary drawn using an oxygen torch. The sample was subsequently dried under vacuum at 800°C for 30 min, after which the capillary was severed by melting, leaving the Pt capsule sealed under vacuum. The evacuated silica tube + Pt capsule/sample assembly was then heated to 1200°C and reacted for 18 days, yielding transparent hexagonal crystals ~10 μm in diameter.

Samples are designated FxCly, where x and y are the nominal mol% of fluor- and chlorapatite component, respectively. End-member compositions are designated F100

and Cl100.

4.3.2 Solid-State NMR

Solid-state magic angle spinning (MAS) NMR spectra were obtained on a Varian Infinityplus 500 MHz (11.7 T) spectrometer operating at 202.318 MHz for ^{31}P, 470.179 MHz for ^{19}F, and 48.98 MHz for ^{35}Cl using standard single-pulse (SP) techniques. ^{31}P and ^{35}Cl spectra were collected at a spinning rate of 10 kHz, and ^{19}F spectra at 15 kHz. A T3 HX probe configured for 4mm rotors was used for all experiments. The rotor assembly consisted of ZrO_2 sleeves, and vespel tips and spacers. The ^{31}P pulse width (pi/2) was 5 μs, and 128 transients were collected at a relaxation delay of 30s. At longer relaxation delays signal intensity did not increase further, so at this delay the spectra are fully relaxed. ^{31}P chemical shifts were measured relative to the phosphate resonance in stoichiometric hydroxylapatite set to $\delta_P = 2.65$ ppm. The ^{19}F pulse width was 5μs (pi/2), and the relaxation delay was 600s for full relaxation, determined by acquisition of fluorapatite spectra with relaxation delays between 5 and 800s. After 600s signal intensity did not increase further, so these spectra are considered fully relaxed. The number of transients varied between 4 and 148 owing to the varied concentration of fluorine. ^{19}F chemical shifts were measured relative to $CFCl_3$ (*aq)* set to $\delta_F = 0$ ppm. The solution (non-selective) ^{35}Cl $\pi/2$ pulse width was set to 4μs using signal from a 1M aqueous solution of NaCl. For solids acquisition 2μs pulses were used (selective $\pi/2$)[62]. The relaxation delay was 2s, and the number of transients varied between 2400 and 170,000 to obtain suitable signal to noise due to the varied concentration of chlorine. Chemical shifts were measured relative to NaCl (*aq*) set to $\delta_{Cl} = 0$ ppm. No signal was observed in background spectra for ^{35}Cl, ^{19}F, and ^{31}P collected using an empty 4mm rotor.

$^{19}F\{^{35}Cl\}$ TRAPDOR [63] data were collected for the F50Cl50 composition at a spinning rate of 20 kHz, using a probe outfitted for 3.2 mm (O.D.) rotors. The ^{19}F pulse width (pi/2) was 5 µs, and the ^{35}Cl solid pulse width (pi/2) was 12 µs. The interpulse delay (τ) was 750 µs, the relaxation delay was 120s, and 345 scans were collected.

4.4 Results

4.4.1 ^{31}P Single-Pulse (SP) MAS NMR Spectroscopy

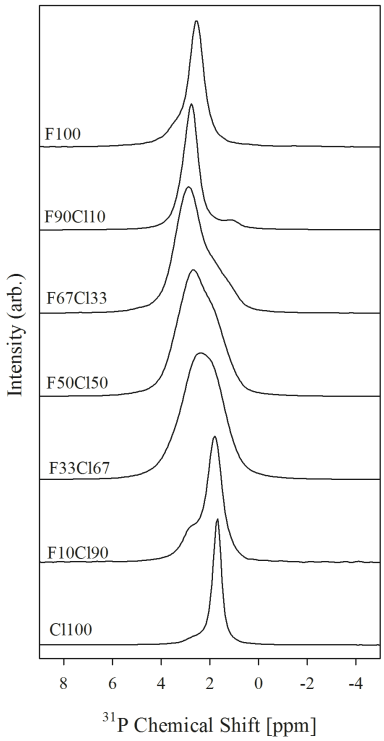

Figure 40: ^{31}P SP NMR spectra of F,Cl apatites; 128 scans collected with a pulse delay of 30s

	Chemical Shift (ppm)	FWHM (ppm)	Relative Intensity	1st Spectral Moment (ppm)
F100	3.4	0.8	0.13(3)	2.7
	2.5	0.7	0.87(3)	
F90Cl10	2.8	0.7	0.96(2)	2.7
	1.1	0.8	0.04(1)	
F67Cl33	2.9	1.3	0.79(6)	2.6
	1.6	1.3	0.21(7)	
F50Cl50	2.7	1.6	0.80(6)	2.6
	1.5	1.2	0.20(4)	
F33Cl67	2.6	2.0	0.33(12)	2.4
	2.2	1.8	0.67(10)	
F10Cl90	2.8	0.9	0.21(11)	2.0

	1.8	0.7	0.79(11)	
Cl100	1.9	1.4	0.29(20)	1.8
	1.7	0.4	0.71(20)	

Table 14: ^{31}P NMR Parameters. Uncertainty in relative intensity obtained by fitting spectra thrice with minor adjustments to phasing.

The ^{31}P single-pulse (SP) MAS NMR spectra of the F,Cl apatites investigated in this work are shown in Figure 40, and the results of least-squares fitting of the spectra to a sum of Gaussian curves are shown in Table 14. All spectra were fit using two peaks, however the position, width, and relative contribution vary considerably between differing compositions. Despite the complex, asymmetric nature of the observed line shapes, a few general trends are noted. The line shapes of those samples at or near end-member composition (Cl100, F100, Cl90F10, and F10Cl90) feature prominent, relatively narrow (0.4-0.7 ppm FWHM) signals and shoulders of greater width and lesser intensity. In the case of the end-members, the broadened shoulder is observed at higher chemical shift to the prominent narrow signal. The origin of the trailing intensity towards higher chemical shift in F100 and Cl100 is uncertain, however it is possible that this signal is due to a small amount of a poorly crystalline phosphate phase.

For those binary compositions nearest the end-members (F10Cl90 and F90Cl10), the shoulders appear on opposing sides of the primary resonance; in F10Cl90 the shoulder appears at lower chemical shift to the main signal, and in F90Cl10 the shoulder is observed at higher chemical shift relative to the main signal.

Previous solid state ^{31}P NMR analysis of apatite has shown that the phosphate ^{31}P chemical shifts of fluorapatite and hydroxylapatite are indistinguishable [64], [65], and that ^{31}P chemical shifts of fluorapatite and chlorapatite can be readily resolved[66].

O'Donnell et al. [66] demonstrated that phosphate tetrahedra associated with fluorine nuclei give a higher chemical shift relative to those associated with chlorine, and comparable chemical shifts were observed in the present end-member ^{31}P spectra (2.7 vs. 1.7 ppm in the present work for Cl100, 3.3 vs. 2.5 ppm in the present work for F100). Based on this information we assign the shoulder in F90Cl10 at lower chemical shift to phosphate groups adjacent to chlorine, and assign the shoulder at higher chemical shift in F10Cl90 to phosphate groups adjacent to fluorine. These assignments are relatively straightforward because phosphate groups in apatite are closely associated with only a single column anion position. The shortest anion-P distance in fluorapatite is 3.6Å and the next shortest is 4.98Å[46], probably too large a distance to effect phosphate chemical environments. As a result only two distinct chemical environments exist, phosphate proximal to fluorine, or phosphate proximal to chlorine. The relative signal intensities of the two peaks for F90Cl10 and F10Cl90 are in reasonable agreement with expected 1:9 or 9:1 ratio considering the uncertain compositions and incomplete resolution based on nominal F:Cl stoichiometry. A similar agreement is observed for F67Cl33 and F33Cl67; 79 and 33 percent of the ^{31}P intensity is attributed to the peak at greater chemical shift (P near F) for F67Cl33 and F33Cl67, respectively. The resolution of both signals appears much poorer in F33Cl67.

The origin of the trailing intensity towards higher chemical shift in F100 and Cl100 is uncertain, however it is possible that this signal is due to a small amount of a poorly crystalline phosphate phase.

The peak widths of all signals increase as the F:Cl ratio approaches 1:1, suggesting a distribution of ^{31}P chemical environments due to structural disorder. Least-squares fitting of the F50Cl50 spectrum using two peaks resulted in two broad resonances, with the peak at higher chemical shift 4 times more intense than the signal at lower chemical shift. However the reported relative intensities of these signals may be inaccurate, owing to the poor resolution and uncertain peak.

4.4.2 ^{19}F SP MAS NMR Spectroscopy

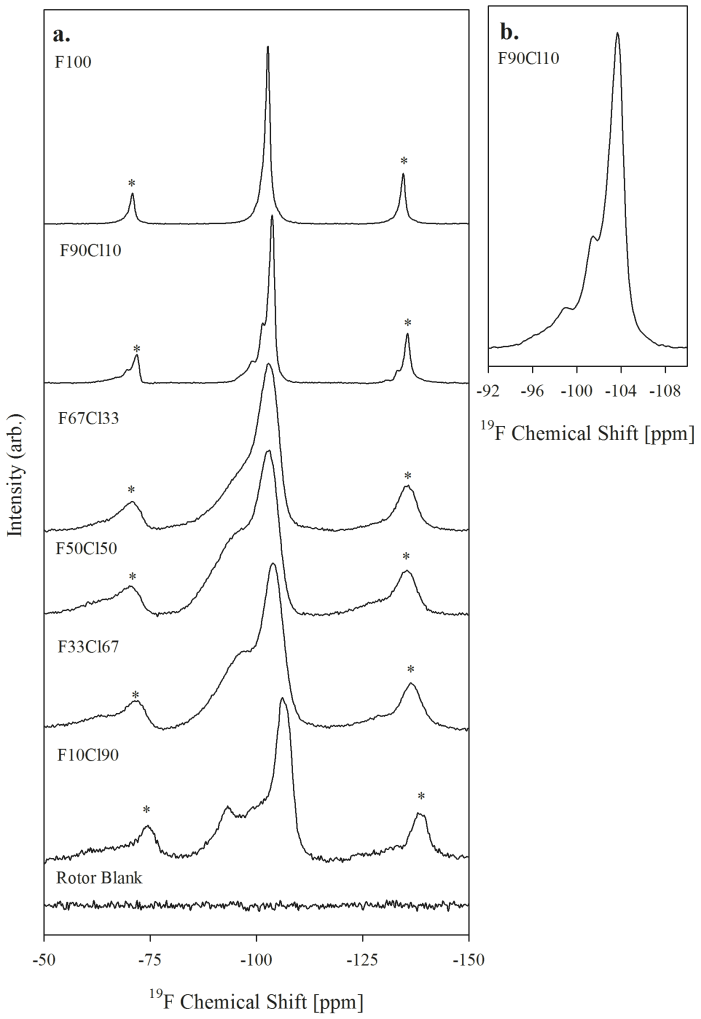

Figure 41a: ^{19}F SP MAS/NMR spectra of F,Cl apatites: collected using 600s pulse delays. Number of acquisitions varied for samples owing to the concentration of ^{19}F; 4 scans for F100 and F90Cl10, and 8, 16, and 32 scans for F67Cl33, F50Cl50, and F33Cl67, respectively. 148 scans collected for both F10Cl90 and the rotor blank. Fig 2b: The center band region of the ^{19}F NMR spectrum of F90Cl10 at expanded scale. Asterisks denote spinning side band positions (SSBs)

Chemical Shift (ppm)	FWHM (ppm)	Relative Intensity	1st Spectral ^{19}F moment (ppm)
F100			
-102.6	1.5	1	-102(1)
F90Cl10			
-96.3	2.7	0.03(3)	-101.4(8)
-99.3	3.2	0.14(4)	
-101.3	1.2	0.11(4)	
-103.8	1.7	0.72(5)	
F67Cl33			
-97.3	11.1	0.49(1)	-100.3(5)
-103.0	4.8	0.503(9)	
F50Cl50			
-96.2	13.5	0.65(1)	-98.3(5)
-103.0	5.0	0.352(6)	
F33Cl67			
-97.2	13.3	0.61(1)	-100(3)
-104.1	4.9	0.392(6)	
F10Cl90			
-93.2	6.5	0.20(1)	-102.0(4)
-101.2	8.4	0.34(2)	
-106.5	4.1	0.46(1)	

Table 15: Results of fitting ^{19}F MAS NMR Spectra

The ^{19}F single-pulse (SP) NMR spectra of the F,Cl apatites investigated in this work are shown in Figure 41, and the results of least-squares fitting of the spectra to a sum of Gaussian curves are shown in Table 15. The ^{19}F NMR spectrum of F100 features a single narrow peak, indicative of a singular, well-defined fluorine chemical environment as expected for single-phase fluorapatite. The ^{19}F NMR spectrum of F90Cl10 shows a narrow prominent resonance, and trailing intensity at higher chemical shift with two additional peaks. Figure 41b more clearly shows the signals in F90Cl10 at expanded horizontal scale. The signals at higher chemical shift are not believed to arise

from ^{19}F environments proximal to trace impurities such as OH within the apatite lattice because of the low concentration of OH measured previously [61] (less than two mol%).

The ^{19}F NMR spectra of F67Cl33, F50Cl50, F33Cl67, and F10Cl90 exhibit broadened spectral profiles relative to those of F90Cl10 and F100. These spectra were fit with two symmetrical signals a relatively narrow signal at lower chemical shift and a broadened shoulder at greater chemical shift, and in the case of F10Cl90 a horn is also observed at -93.2 ppm. The broad shoulder in these spectra is most prominent for F50Cl50. The 1st spectral moments are shown in the right-most column of Table 15, and increase as the F:Cl ratio approaches 1:1. The end-member or near-end-member compositions, F100, F90Cl10, and F10Cl90 have similar first spectral moments, approximately -102 ppm.

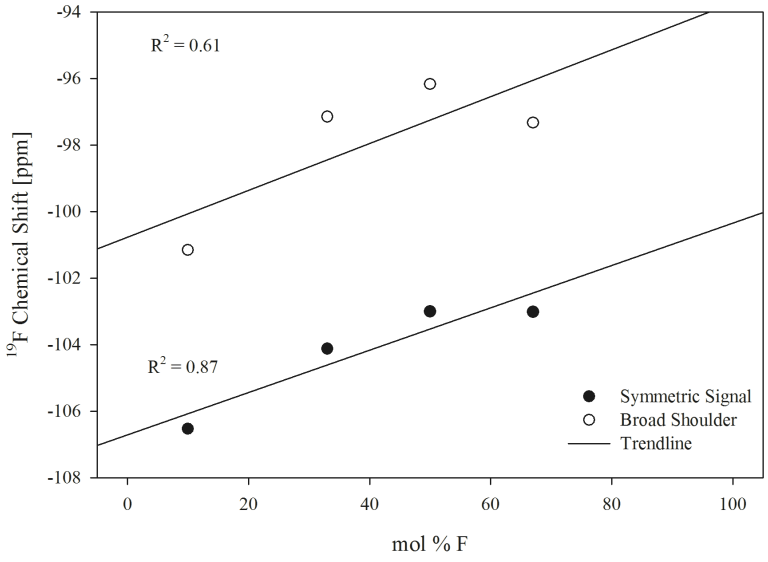

Figure 42: Plot ^{19}F chemical shifts vs. fluorine content for broadened F,Cl apatite compositions

As the Cl content increases, the signals move to lower chemical shift, reflecting the effect of a less electronegative element (Cl) on the spectra, which is reflected in Figure 42. There is otherwise no apparent simple relationship between F:Cl ratio and ^{19}F spectral features, in contrast to the ^{31}P results.

4.4.3 $^{19}F\{^{35}Cl\}$ TRAPDOR NMR Spectroscopy

The results of the $^{19}F\{^{35}Cl\}$ TRAPDOR NMR experiment for F50Cl50 are shown in Figure 43. The TRAPDOR[63] experiment is a double-resonance pulse sequence that permits elucidation of coupling schemes between spin-½ and quadrupolar nuclei, such as ^{19}F and ^{35}Cl in the present case. The upper spectrum (Figure 43a) is a spin echo spectrum, showing those ^{19}F environments that have not been attenuated due to short T_2 relaxation. The spin echo and single-pulse spectra appear very similar, reflecting the nominal amount of T_2 relaxation for this sample. The lower spectrum (Figure 43b) shows the $^{19}F\{^{35}Cl\}$ TRAPDOR difference spectrum, which shows those ^{19}F environments that are coupled to ^{35}Cl. The TRAPDOR difference spectrum has been scaled vertically to facilitate comparison to the upper spin echo spectrum. The ratio between the intensity of the broad shoulder and the narrower signal at lower chemical shift remains unchanged between the spin echo spectrum and the TRAPDOR difference, which indicates that the resolved spectra features do not correspond to F with significant differences in average F-Cl interatomic distances. This observation agrees with the ^{19}F SP NMR results that showed no systematic variation in spectral profile with F:Cl ratio.

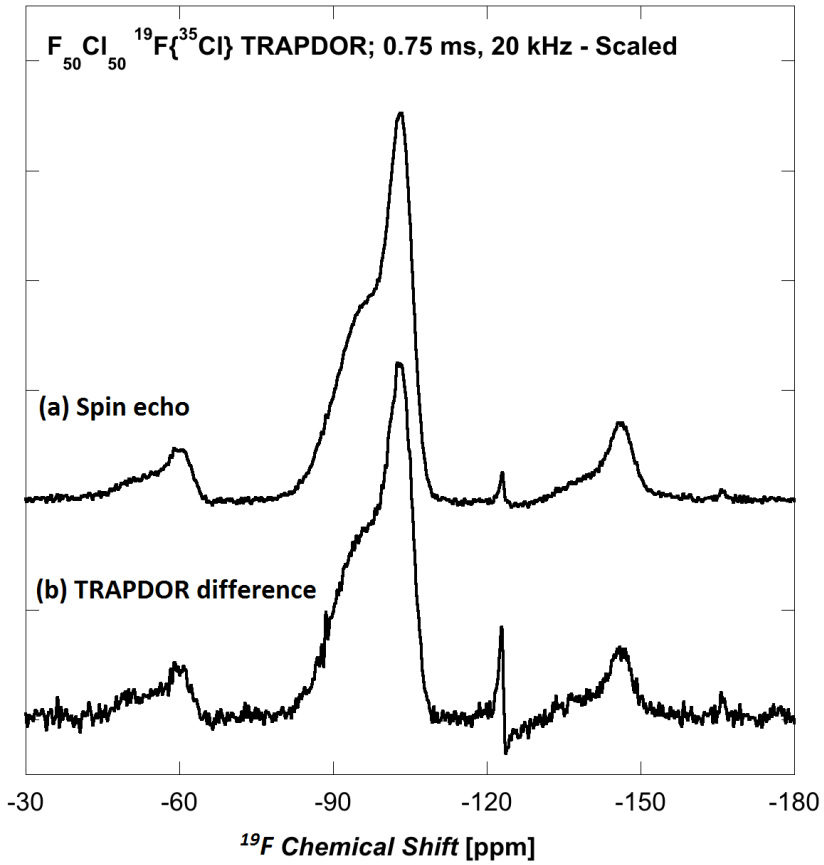

Figure 43: $^{19}F\{^{35}Cl\}$ TRAPDOR NMR of F50Cl50. Spin echo spectrum shown in the upper spectrum, TRAPDOR difference spectrum shown below, scaled to facilitate comparison with the spin echo. 345 scans were collected at a spinning rate of 20kHz, using a 120s relaxation delay.

4.4.4 ^{35}Cl SP MAS NMR Spectroscopy

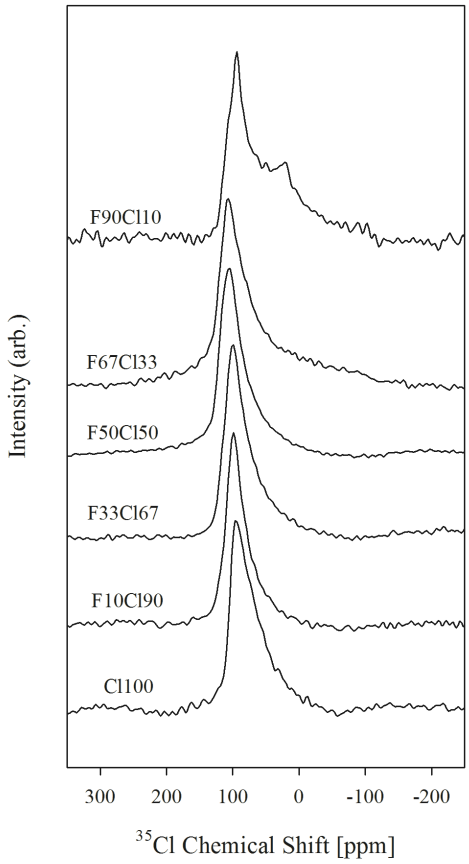

Figure 44: ^{35}Cl SP NMR Spectra of F,Cl Apatites. The pulse delay was 2s for all samples, and 170,000, 80,000, 44,000, 5000, 4000, and 3700 scans were collected for F90Cl10, F67Cl33, F50Cl50, F33Cl67, F10Cl90, and Cl100, respectively.

Sample	^{35}Cl left peak position [ppm]	FWHM [ppm]	1st spectral ^{35}Cl moment [ppm]
F90Cl10	94.1	35	46(4)
F67Cl33	106.5	48	35(10)
F50Cl50	104.0	41	63(7)
F33Cl67	100.7	39	76(4)
F10Cl90	99.0	33	77(4)
Cl100	96.5	44	58(6)

Table 16: ^{35}Cl Chemical Shifts

The ^{35}Cl single-pulse (SP) NMR spectra are shown in Figure 44. Except for that of F90Cl10, these spectra can broadly be described as featuring a sharp left edge with trailing intensity to lower chemical shift. Peak shapes of this type have been ascribed to a distribution of quadrupolar coupling constants, arising from a distribution of electronic

environments of varying asymmetry but with relatively small range of chemical shifts. Spectral parameters are reported in Table 16, and demonstrate that as the fluorine content is decreased and the chlorine content increases, the position of the signals move to lower chemical shift. The F90Cl10 and F67Cl33 ^{35}Cl spectra feature significant trailing intensity to smaller chemical shift, indicating that the Cl atoms in these samples may experience a greater range of electronic environments than the other samples. There is a peak in the spectrum of F90Cl10 at +20 ppm, possibly due to quadrupolar fine structure. However, ^{35}Cl NMR experiments at different field strength are necessary to deduce the origin of this signal.

The amount of existing ^{35}Cl data in the literature is rather limited, owing to the low γ and poor sensitivity of the ^{35}Cl nucleus. McCubbin et al. [67] described a F,Cl composition in which the target F,Cl composition was F50Cl50, and observed a second-order quadrupolar line shape with an isotropic ^{35}Cl chemical shift of +115 ppm. The ^{35}Cl C_Q from that work (1.6 MHz) was significantly greater than that reported previously for chlorapatite (0.8 MHz)[68].

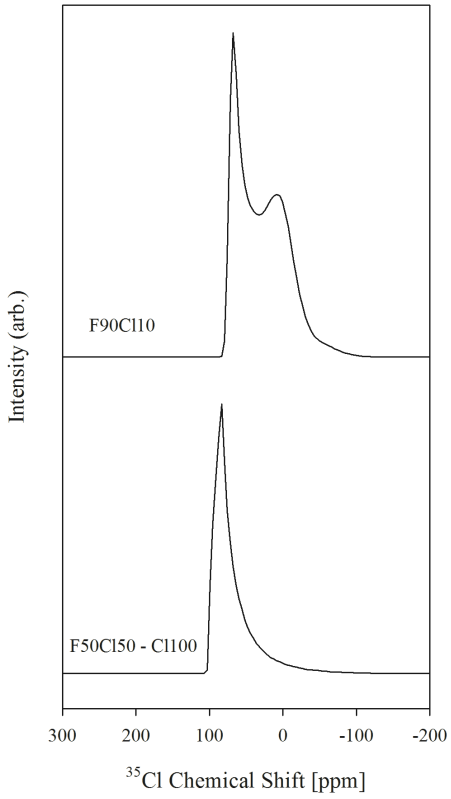

Figure 45: Simulated ^{35}Cl SP NMR Spectra approximating F90Cl10 and the four compositions between F50Cl50 and Cl100

Composition	δ_{iso} (ppm)	C_Q (MHz)	η
F90Cl10	94.1	2.5	-0.35
F50Cl50-Cl100	100	1	-0.5
	95	1	-0.5
	90	1	-0.5
	85	1	-0.5

Table 17: Simulated ^{35}Cl NMR parameters.

^{35}Cl simulations of F90Cl10 and F50Cl50 are shown in Figure 45, and the NMR parameters for these spectra are shown in Table 17**.** These calculations were made using a distribution of electric field gradients (EFG, η in Table 17). The upper spectrum labeled F90Cl10 was generated to approximate the second-order quadrupolar pattern of the same composition shown in Figure 44, which features a horn at +20 ppm. The

experimental ^{35}Cl spectra of F50Cl50, F33Cl67 F10Cl90 and Cl100 have similar appearance, are represented in the lower simulated spectrum of Figure 45. This spectrum was generated using a range of sites with a 15 ppm range of isotropic chemical shifts (δ_{iso}) from 85 to 10 ppm, which give appropriate width to the quadrupolar line shape, identical quadrupolar coupling constants (C_Q) of 1 MHz, and a range of electric field gradients. These results suggest that the ^{35} Cl NMR spectra obtained experimentally are due to Cl environments with a small range of chemical shifts, moderate quadrupolar coupling, and a distribution of electric field gradients. The Cl environments in F90Cl10 appear more well-defined, and may exhibit fine structure owing to the reduced range of electronic field gradients.

4.5 Discussion

4.5.1 Variation in phosphorus environments

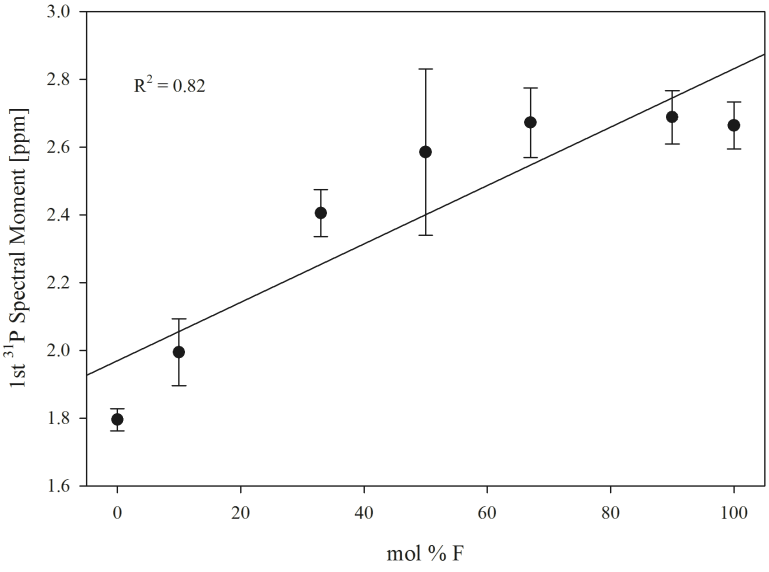

Figure 46: Plot of 1st ^{31}P spectral moment vs. fluorine content. Uncertainties obtained by fitting spectra thrice and calculating the range of spectral moments for each fit.

The ^{31}P results indicate that for the present samples, apatite phosphate groups are sensitive to only the nearest anion column occupant. The correlation between anion column occupant and ^{31}P chemical shift is apparent in Figure 46, which features the 1st ^{31}P spectral moment (intensity weighted average chemical shift) plotted against the target amount of fluorine in each sample. Measuring the 1st ^{31}P spectral moment eliminates errors associated with fitting the intensity of two overlapping peaks, such as peak position and width. Figure 46 reveals a fairly strong correspondence, however there are noteworthy deviations from a linear trend for end-member or near end-member compositions. The deviations may be due structural disorder associated with F,Cl solid solution, or errors in measurement due to very broad line shapes. The uncertainty in these measurements is rather large, particularly for F50Cl50.

4.5.2 On hydroxyl content and precautionary steps to minimize its concentration

Comparison of the present results with previous work shows the importance of excluding water for preparing binary F/Cl apatite. O'Donnell [66] report a ^{31}P chemical shift of 2.7 ppm for chlorapatite, that differs significantly from that observed here at 1.7 ppm. This chemical shift difference can be attributed in part to normal variation in chemical shift measurement; for example O'Donnell et al. [66] reported a fluorapatite ^{31}P chemical shift of 3.3 ppm whereas the F100 ^{31}P shift in the present work is 2.8 ppm. Both fluorapatite compositions are presumed to be nearly identical, yet their ^{31}P NMR chemical shifts differ by 0.5 ppm. Normal variation in chemical shift measurement (i.e. 0.5 ppm) fails to account for the magnitude of difference in chlorapatite ^{31}P chemical shift.

The samples described by O'Donnell et al. [66] and those in the present work were both prepared by high temperature synthesis, the principal difference being the extensive measures taken in the present work to minimize the formation of hydroxyl component (see experimental). These measures are particularly important for chlorine rich compositions, due to the hygroscopic nature of the starting materials required to prepare chlorapatite, especially calcium chloride. Therefore it is probable that the chlorine rich compositions described by O'Donnell et al. [66] contain a significant amount of hydroxyl component.

The presence of OH in the chlorapatite composition described by O'Donnell et al.[66] is reflected in the ^{31}P NMR data. The ^{31}P chemical shifts of fluorapatite and fluorhydroxylapatite are indistinguishable [64],[65], so therefore a ^{31}P spectrum of chlorapatite with some fluorine component could be expected to also resemble a chlorapatite with hydroxyl component. Either F or OH in a dominantly Cl-rich apatite composition would shift the ^{31}P peak position to higher chemical shift, so it follows that the higher chemical shift for chlorapatite observed in O'Donnell et al. [66] versus the present chlorapatite ^{31}P spectrum is likely due to the formation of hydroxyl component.

Comparison of peak widths provides further evidence for the relative success of the present study in preparing near-binary F/Cl apatite. The ^{31}P line shapes in the present work are narrow for fluorapatite and become progressively broader for compositions close to F:Cl = 1:1, which was also observed in the ^{31}P NMR work by O'Donnell et

al.[66] However the line widths in O'Donnell et al. [66] remain broad (1-1.5 ppm FWHM) for compositions between F:Cl = 1:1 (F50Cl50) and end-member chlorapatite. In contrast the present ^{31}P NMR results show progressively narrower line widths as the composition approaches end-member chlorapatite. This difference in peak width for Cl-rich compositions can also be attributed to differences in hydroxyl content. As the chlorine content increases, so does the susceptibility for incorporation of hydroxyl component during synthesis. Presence of hydroxyl would presumably yield a more complex ^{31}P peak shape from populations of phosphate groups proximal to chlorine atoms and hydroxyl groups. This effect is most clearly evident by noting the mirror image resemblance between the chlorapatite ^{31}P line shape reported in O'Donnell et al. [66] and the F67Cl33 line shape reported in the present work. The F67Cl33 line shape from the present work features a prominent (79% relative intensity) signal at 2.9 ppm, due to phosphate groups proximal to fluorine and a less prominent shoulder at 1.6 ppm, due to phosphate groups proximal to chlorine. The chlorapatite line shape in O'Donnell et al. [66] features a prominent (84% relative intensity) signal at 2.7 ppm, presumed to be due to phosphate groups proximal to a chlorine, and a less intense shoulder at 4 ppm, presumed to be due to phosphate groups proximal to hydroxyl. The reason why the peak widths do not become narrower as the target composition approaches that of chlorapatite is because the actual composition contains a significant amount of OH apatite, which is present in the ^{31}P spectra as shoulder intensity at higher chemical shift. In the present samples the ^{31}P peak widths do become narrower as the composition approaches that of chlorapatite because formation of hydroxyl component has been eliminated by the drying steps taken during sample synthesis. This interpretation is further strengthened through

comparison with the work of McCubbin et al. [67] to the present results. From electron probe microanalysis (EPMA) the authors demonstrated that the composition is F50Cl37OH13. The ^{31}P line shape for that sample most closely resembles that of F67Cl33 in the present work. Because ^{31}P signals from phosphate proximal to hydroxyl groups cannot be distinguished from phosphate groups proximal to fluorine, it follows that the ^{31}P NMR spectrum of a ternary composition such as F50Cl37OH13 would resemble F67Cl33.

O'Donnell et al. [66] also performed ^{19}F MAS NMR analysis, however these data differ significantly from the present results. This difference is partly due to NMR acquisition conditions. For example, O'Donnell et al. [66] used a lower field strength NMR spectrometer (4.7T vs. 11.7T in the present work), which could reduce resolution of distinct chemical shifts, and a lower MAS rate (10kHz vs. 15kHz in the present work), which could result in broader signals due to diminished averaging of dipolar coupling and chemical shift anisotropy. As with the ^{31}P NMR spectra, the role of hydroxyl component is likely a contributing factor to the differences between the two data sets. Although the chemical shifts of the narrow signal in the present ^{19}F NMR spectra are in good correspondence with those reported in O'Donnell et al. [66] (shown in Table 18) the line shapes in that previous study do not feature the prominent shoulder toward higher chemical shift observed here. The spectral profiles instead generally have a broad, symmetric appearance, becoming progressively broader as the F:Cl ratio is decreased. As for the ^{31}P results, these differences can be attributed to differences in OH content.

Hydroxyl groups have been demonstrated to facilitate average hexagonal anion arrangements between F and Cl, so it is likely that the hydroxyl component believed to be present in those compositions in O'Donnell et al. [66] reduces the strain in the anion column, resulting in more symmetric ^{19}F line shapes.

Nominal Composition	δ_F Present work (ppm)	δ_F O'Donnell et al. (ppm)
F100	-102.6	-102.8
F90Cl10	-103.8	-102.8
F50Cl50	-103.0	-103.4
F10Cl90	-106.5	-105.4

Table 18: ^{19}F Chemical shifts in the present work compared to a previous work

McCubbin et al. [67] observed comparable ^{19}F line shapes to those in the present work, however the intensity of the broad shoulder at greater δ is diminished relative to the sample with comparable composition discussed in the present work (F50Cl50). McCubbin et al. [67] noted that this sample contains 13 mol% hydroxyl component. Hydroxyl component has been demonstrated to play a role in facilitating a F/Cl distribution that features fluorine in its end-member position, and preserves average hexagonal symmetry[61], [69], so the diminished asymmetry in the ^{19}F line shape relative to the present work most likely reflects a larger fraction of ^{19}F nuclei in the end-member fluorine position.

These results further emphasize that minimizing hydroxyl component as was performed in the present work is important in investigating F,Cl apatite, because hydroxyl component forms readily and can impact the resulting structure in meaningful ways.

4.5.3 Variation in fluorine environments

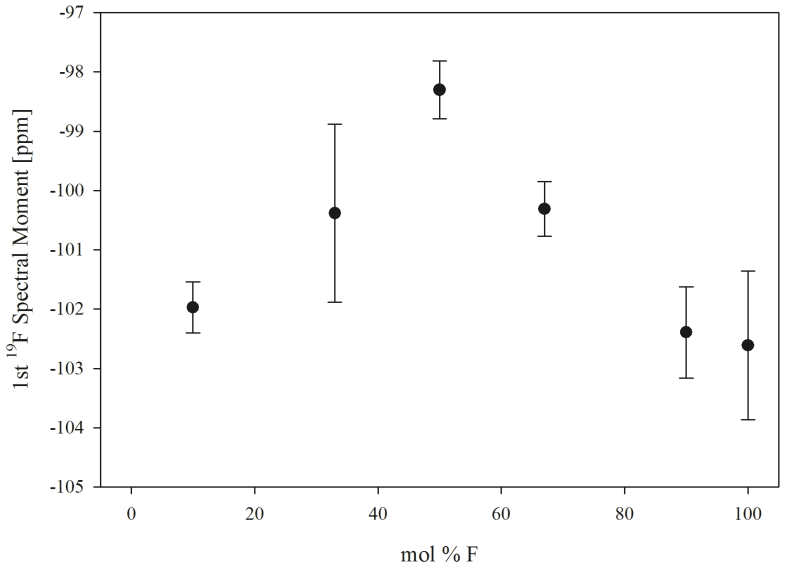

Figure 47: Plot ^{19}F chemical shifts vs. fluorine content

The ^{19}F NMR line shapes for F67Cl33, F50Cl50, F33Cl67, and F10Cl90 appear markedly different from F90Cl10 and F100; the peak width of the prominent resonance is much greater in the former set of spectra, and a broad shoulder is observed at greater chemical shift. The line shapes for those intermediate and Cl-rich compositions do not change as a function of F:Cl ratio, suggesting that the ^{19}F line shapes are insensitive to the nearest anion column occupant. Figure 47 demonstrates that the 1st ^{19}F spectral moment exhibits non-linear variation with composition, further indicating that line shapes are not correlated with anion column chemistry. The ^{19}F{^{35}Cl} TRAPDOR data support this interpretation as well; neither of the spectral features, the narrower prominent signal nor the shoulder at greater chemical shift are attenuated to a greater extent to one another, indicating that the ^{19}F line shapes are not due to variation in F-Cl distance.

The most plausible explanation for the present complex ^{19}F NMR line shapes is a variation in interatomic distance between fluorine and the Ca2 triad. Kiczenski and Stebbins[70] noted that the ^{19}F chemical shift generally increases with the radius of the adjoining cation. By normalizing metal oxidation state and structure type it is apparent that the correlation between ^{19}F chemical shift and cation radius can be extended to M-F interatomic distance. This effect is shown for a series of halite and fluorite-type metal fluorides, shown in Figure 48 and Table 19. There are deviations from the linear trend between ^{19}F chemical shift and M-F distance, particularly for the alkali halite-type fluorides, however these data indicate generally that increased M-F interatomic distance will result in a greater chemical shift. Therefore, it is likely that the broad shoulder observed at greater chemical shift in the present ^{19}F NMR results is due to a distribution of Ca2-F distances greater than the Ca2-F distance in end-member fluorapatite.

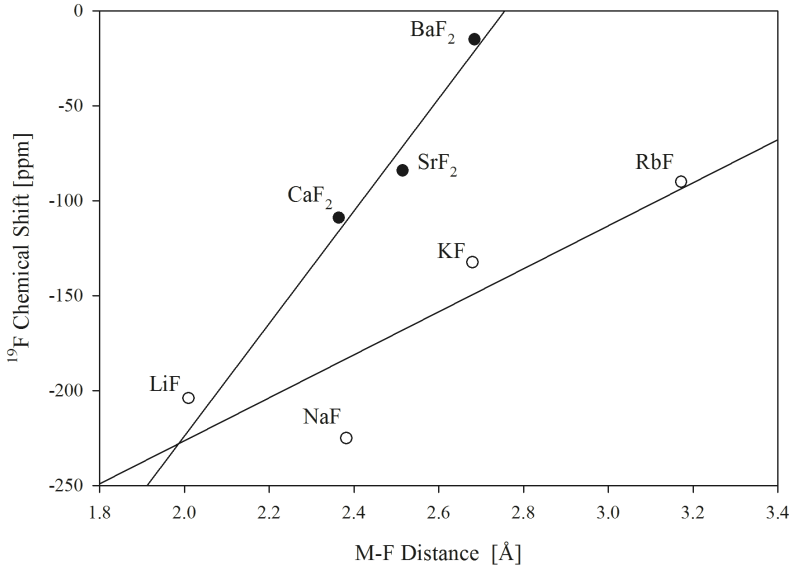

Figure 48: ^{19}F chemical shifts vs. M-F distance for halite and fluorite type metal fluorides

Structure	$d_{M\text{-}F}$(Å)	^{19}F δ (ppm)
CaF_2	2.365[71]	-109
SrF_2	2.516 [72]	-84

BaF_2	2.685 [72]	-15
LiF	2.010 [73]	-204
NaF	2.385 [74]	-225
KF	2.680 [75]	-132
RbF	3.172 [75]	-90

Table 19: M-F interatomic distances and ^{19}F chemical shifts of halite and fluorite-type metal fluorides. ^{19}F chemical shifts obtained from Kiczenski and Stebbins[70] and refs therein.

Increasing the Ca2-F distance requires either the dilation of the anion channel through migration of the Ca2 triad in the *a*-*b* directions, or movement of fluorine atoms along *c*. Movement of the Ca2 triad is unlikely, as it would result in non-linear changes in the *a* lattice parameter, which were not observed by refinement of powder X-ray diffraction data [61]. The generation of new atomic positions in the anion channel, on the other hand, has been well-described regarding apatite compositions along both the F,Cl and F,OH binaries[10], [54], and such atomic positions could be occupied without large deviations in linear behavior for lattice parameters. We conclude that the ^{19}F NMR line shapes in the present work are most likely due to variation in fluorine atomic position with respect to the Ca2 triad. The narrower resonance at lower δ is assigned to fluorine in the end-member fluorine atomic position, within the Ca2 triad or slightly displaced above or below it (giving rise to the increase in peak width), and the broad shoulder at higher δ is assigned to fluorine at a distribution of distances from the Ca2 triad, where the left most edge of the shoulder represents fluorine atoms at the greatest distance from Ca2.

It is possible to approximate changes in Ca2-F distance from ^{19}F chemical shifts using the correlation in Figure 48. Only the alkaline fluorides were used to more closely approximate apatite composition. Table 20 portrays a few parameters used in this calculation. The column second to the left, labeled peak to peak, is the distance between the peak position of the narrow resonance at lower chemical shift to the peak position of

the broad shoulder at greater chemical shift. The position of the peak in the narrow feature is presumed to be representative of F environments in the fluorapatite position, and the peak position of the shoulder at greater chemical shift frequency is presumed to represent the average displacement of fluorine away from the Ca2 triad. Measuring the position of the broad shoulder relative to the narrow signal at lower δ instead of using absolute chemical shifts eliminates the deshielding effect of Cl atoms on ^{19}F chemical shifts, and also avoids the need for an intercept term when converting from ^{19}F chemical shift to Ca2-F distance. The column immediately to the right, labeled peak to left edge, is the distance between the left-most edge of the broad shoulder and the peak position of the narrow signal, representative of the maximum displacement of fluorine away from its end-member position within the Ca2 triad. The next two columns labeled average Ca2-F and max Ca2-F represent the average and maximum Ca2-F distance obtained from the peak to peak and peak to left edge values, respectively, via the relation:

$$(\Delta^{19}F \text{ shift (ppm)} \div 296.4) + 2.311 = \text{Ca2-F (Å)}$$

In the above equation 296.4 is the slope of the ^{19}F chemical shift: metal-fluorine radius calibration for fluorite-type alkaline earth fluorides, and 2.311 is the Ca2-F distance for fluorine in its end-member position[46]. The two right most columns represent the average and maximum vertical *c*-axis displacement of the anions relative to the Ca2 triad obtained from the average and max Ca2-F distances respectively. These values were calculated using the below relation, where $FCl_{Ca2\text{-}F}$ is the Ca2-F distance for a given F-Cl composition, and $F_{Ca2\text{-}F}$ is the Ca2-F distance in end-member fluorapatite, 2.311Å[46].

$$\text{Vertical F displacement relative to Ca2 triad (Å)} = \sqrt{(FCl_{Ca2-F})^2 - (F_{Ca2-F})^2}$$

Sample	Peak to Peak (ppm)	Peak to left edge (ppm)	Average Ca2-F (Å)	Max Ca2-F (Å)	Average F displacement relative to	Furthest F displacement relative to

					Ca2 triad	Ca2 triad
F67Cl33	5.7	16.0	2.3	2.4	0.30	0.50
F50Cl50	6.8	18.5	2.3	2.4	0.33	0.54
F33Cl67	7.0	18.1	2.3	2.4	0.33	0.54
F10Cl190	5.4	16.5	2.3	2.4	0.29	0.51

Table 20: Approximation of Ca2-F distances ^{19}F NMR results. Derivation of specific parameters explained in body of text

The F50Cl50 composition was characterized by ScXRD in a previous contribution from our group[52], and new anion positions were proposed in order to preserve average hexagonal ordering, including a fluorine position displaced 0.57Å away from the fluorine position in fluorapatite. The average F positions in the second to right-most column in Table 20 should correspond to those values reported by XRD, however comparison of these values reveals that the F displacements approximated via ^{19}F NMR are significantly less than those reported via ScXRD. The maximum F displacements, shown in the right most column of Table 20, exhibit a better correspondence. It should be noted, however that the value reported from XRD and those from ^{19}F NMR are of the same order of magnitude, suggesting that the interpretation of the broad shoulder at higher chemical shift frequencies may be indeed correlated with fluorine displacements away from the Ca2 triad.

The ^{19}F spectrum of F10Cl90 features a horn at -93.2 ppm, at a higher chemical shift than the ^{19}F shift in fluorapatite and the shoulder in other F,Cl compositions. The position of this peak suggests that the Ca2-F distance is greater than that in the broad shoulder, and the symmetric shape of this peak suggests the interatomic distance is well defined. From the above calculations this signal has a Ca2-F distance of 2.4Å, and is displaced approximately 0.46Å from the fluorine position in fluorapatite. This is a closer correspondence to the new F position described by Hughes et al. [52], however ScXRD

data for F10Cl90 are not available due to prohibitively small crystal size. The definition of this peak suggests it may be a preferred F position that is not currently described.

4.5.4 ^{35}Cl and ^{19}F Spectra of F90Cl10

The ^{19}F line shapes of all intermediate compositions show similar broadened profiles, with the exception of F90Cl10. The F90Cl10 ^{19}F spectrum more closely resembles that of F100 apatite, featuring a narrow prominent signal at -103.8 ppm with some minor trailing intensity towards higher chemical shift. The ^{35}Cl spectrum of F90Cl10 is somewhat anomalous as well in that it exhibits what may be quadrupolar fine structure in the form of a horn at +20 ppm and a shoulder out to approximately -150 ppm. This suggests that the electronic environments experienced by Cl in this composition are better defined than those in the other F,Cl apatite compositions. The disordered anion position regime proposed in the other intermediate F,Cl compositions is probably not present in this composition. Fluorine atoms are probably in their end-member positions within the Ca2 triad, giving rise to a narrow ^{19}F line shape with very little intensity trailing towards higher chemical shifts. Additionally, the chlorine atoms most likely occupy fewer, well-defined atomic positions, owing to their small concentration, which gives rise to the greater detail in the ^{35}Cl NMR spectrum.

4.6 Conclusions and Future Work

By careful synthesis we were able to prepare F,Cl apatites with exceptionally low hydroxyl component. Comparison of solid-state NMR spectra of the present samples to those samples believed to have greater concentrations of hydroxyl component has shown that the presence of hydroxyl groups effect both chemical shifts and overall line shapes in significant ways. This emphasizes not only the importance of hydroxyl groups in

fluorine chlorine arrangements, but also the importance of minimizing hydroxyl content in investigating such arrangements.

The chemical shifts of all nuclei used in this study were observed to move to lower chemical shift as the chlorine content is increased, reflecting the importance of anion column chemistry on the lattice as a whole. However, significant deviations from linear mixing were observed in all cases, suggesting a complex mechanism of solid solution along this binary. The ^{19}F NMR spectra are most telling, and through careful analysis of these spectra we suggest that these variations may be due to a distribution of F-Ca2 triad distances, and approximate atomic positions of fluorine are proposed.

Further analysis is warranted to determine definitively the variation of fluorine positions with respect to the Ca2 triad. Several apatite grains may be of sufficient size for single-crystal X-Ray diffraction at a synchrotron source, which would provide more precise information regarding the average fluorine position in the anion channel, and a more suitable comparison with the present ^{19}F results. ScXRD has additionally revealed the presence of incommensurate scattering in a comparable F,Cl apatite composition[67], and it is possible that the channel anions in these samples also experience an incommensurate modulation in atomic position.

Chapter 5: ^{17}O NMR spectroscopic investigation of the effect of heating hydroxylapatite

5.1 Abstract

Hydroxylapatite (HAp) was enriched hydrothermally with $H_2{}^{17}O$ and investigated using ^{17}O single-pulse (SP), ^{31}P (SP), $^{1}H\{^{31}P\}$ REDOR solid-state NMR spectroscopy and powder X-ray diffraction (PXRD). ^{17}O NMR spectra show distinct signals for hydroxyl and phosphate oxygens, with relative intensities matching stoichiometry. Heat treatment of the sample under vacuum results in decomposition of a significant amount (50%) of HAp into β-TCP, loss of hydroxyl oxygen signal in the ^{17}O spectrum and significant reduction (75%) in the hydroxyl ^{1}H signal. Precise refinement of the lattice parameters after heat-treatment was not possible owing to overlapping reflection intensity from β-TCP, therefore the presence of oxyapatite ($Ca_{10}(PO_4)_6(O^{2-},\square)$), which has been proposed previously to form as a result of HAp heat treatment under vacuum, could not be confirmed.

5.2 Introduction

Hydroxylapatite, $Ca_{10}(PO_4)_6(OH)_2$ (HAp) is an important mineral in the medical and biomaterials sciences due to its occurrence in bone and dental enamel, and exceptional biocompatibility [4]. Research frontiers related to HAp often focus on atomic substitutions, as these substitutions often give rise to important and useful changes in chemical or physical properties. Examples include the incorporation of carbonate in HAp to improve biocompatibility [23], and the incorporation of fluoride in order to improve acid resistivity [10]. In the field of biomaterials, HAp powders often undergo

sintering during processing. There have been reports [76]-[78] that heating of HAp generates varied amounts of oxyapatite (OAp, $Ca_{10}(PO_4)_6(O^{2-}\square)$, where □ represents a vacancy at the column anion position). Such substitution of oxide ion balanced by vacancies may significantly affect important material properties, in similar fashion to the incorporation of carbonate or fluoride. It is possible that oxyapatite or oxy component forms as a result of HAp heat treatment, and therefore may be present in widely utilized HAp-based materials.

The interest in OAp also extends to earth materials, as previous work [55], [79] has posited that non-stoichiometry in the anion position for ternary (F,Cl, and OH) apatites measured via elemental analysis is due to presence of oxyapatite component. OAp was proposed to have formed from dehydration of hydroxylapatite (HAp) during synthesis, via:

$$Ca_{10}(PO_4)_6(OH)_2 \rightarrow Ca_{10}(PO_4)_6(O^{2-}\square) + H_2O$$

There have been reports of single-phase, stoichiometric oxyapatites meta-stable at room temperature for apatite structures containing strontium [77], rare-earth elements, silicates[42], germanates (GeO_4) [80], [81] and iodine [57], but identification of a calcium-phosphate oxyapatite phase remains largely unaddressed.

Henning et al. [76] described the composition of oxyapatite using high-resolution electron microscopy (HREM). However, such analysis involves intense electron beam irradiation and high vacuum. The authors noted that these far-from-ambient conditions may significantly affect the sample. Trombe and Montel reported the synthesis of apatite

with the highest proportion of oxy-component, which was prepared by heating under vacuum and analyzed under ambient conditions [77]. They report that two-thirds of the anion sites were occupied by either oxide ions or associated vacancies. This interpretation was based on changes in mass and average lattice parameters as a function of temperature, which does not conclusively identify the presence of oxyapatite under ambient conditions. The evidence for formation of OAp at elevated temperature in both works is also supported elsewhere by Liao et al. [78] However, where Trombe and Montel[77] report that some OAp persists at room-temperature after heat treatment, Liao et al.[78] propose that OAp rehydrates completely to HAp. These contrasting results exemplify a lack of consensus in the current literature regarding the stability of calcium phosphate oxyapatite under ambient conditions.

Presence of oxyapatite component has also been proposed to balance non-stoichiometry in the anion column in ternary apatites [55], [79]. However the presence of OAp in these cases is based on indirect measurement by difference, assuming stoichiometric occupancy of the anion channel position. Thus, both the existence of calcium-phosphate OAp and the presence of channel O^{2-} in various ternary (F, OH, Cl) apatites are uncertain. In this work we seek to identify using solid state NMR spectroscopy oxyapatite (OAp) prepared by dehydration of hydroxylapatite (HAp).

Solid-state NMR provides insight into the molecular level arrangement of solids through resolution of distinct chemical environments of NMR-active nuclei. The ^{17}O nucleus has been utilized in the NMR structural characterization of both inorganic [82] and organic [83] materials, due to the ubiquity and importance of oxygen. ^{17}O NMR spectroscopy has been employed specifically in the Earth sciences to resolve

crystallographically-distinct oxygen sites in various silicate minerals [84], [85], in addition to bridging (BO) and non-bridging (NBO) oxygens in crystalline silicates [86] and glasses [87]. Thus far, ^{17}O NMR studies of calcium-phosphate hydroxylapatite (HAp) have been limited to first-principles calculations of the NMR properties [88] or silicate-bearing HAp sol-gels [89]. ^{17}O NMR studies of other apatite-based materials predominantly focus on compositions containing larger atoms or chemical moieties (e.g. rare earth elements, silicates, germanates)[80],[90], as these structures have been shown to conduct oxide ions at elevated temperature, and is of great use to the solid-oxide fuel cell (SOFC) community. One such study by Panchmatia et al. [80] assigned an ^{17}O NMR signal to oxide ion in the anion channel of a La-germanante apatite.

The present effort to identify channel oxide in HAp-based materials is relevant to the biomaterials community because many biomaterials are composed of sintered HAp powders. Such materials, as a result of the sintering process, may contain significant amounts of channel oxide and vacancies. Conversion of HAp to OAp may affect rates of osseointegration, mechanical stability, or other physicochemical properties important for biocompatible applications. In addition this work is relevant to researchers in the geosciences community because the presence of OAp serves to complicate analytical measurements of OH, F, and Cl. The abundance of these elements is relevant to geological processes such as the explosivity of magmas [1] and lunar magmatism [41].

5.3 Materials and Methods

5.3.1 ^{17}O Enrichment

The method for enrichment follows approximately that described by Panchmatia et al. [80], the principal difference being in the starting ^{17}O isotopic enrichment of H_2O (30% in the present work vs. 90% in Panchmatia et al. [80]) . 100 mg of reagent grade hydroxylapatite (HAp-ri Sigma Aldrich) and 0.5 mL of 30% enriched $H_2{}^{17}O$ were loaded into an autoclave lined with PTFE, and heated at 200°C for 48 hrs. The powder was subsequently dried at 550°C for 2 hrs. under a flow of nitrogen to eliminate water and preserve isotopic enrichment.

5.3.2 Heat Treatment of HAp (HAp-HT)

The method of heat treatment for hydroxylapatite emulates to the extent possible that described by Trombe & Montel [77]. 60 mg of ^{17}O-enriched HAp were loaded into a Pt capsule, which was crimped shut to minimize spillage but allow for atmospheric exchange. The Pt capsule was then loaded into a silica tube that had been sealed previously on one end. The open end of the silica glass tube was attached to a vacuum pump and the sample was left under vacuum (10^{-4} Bar) for 24 hrs. The silica glass tube + Pt capsule assembly was then inserted into a vertical pot furnace with the vacuum tubing connected, and the sample was slowly (~5°C/min) ramped from room temperature to 850 °C, and held for 30 hrs. The sample (termed HAp-HT throughout) was then cooled to room temperature at (~5°C/min), and finally removed from vacuum. A roughly 10% reduction in mass (2 mg) was observed before and after heating, however a small amount

of powder fell out of the Pt capsule during removal, providing an explanation for at least some of this difference. Complete conversion from HAp to OAp should result in weight loss of approximately 2%.

5.3.3 Powder X-Ray Diffraction (PXRD)

The powder X-ray diffraction patterns were collected using a Rigaku Miniflex 6 (Cu Kα radiation) with a D/TeX high-speed linear position sensitive detector. The patterns were collected over a range of $10° \leq 2\theta \leq 90°$ with a step size of 0.01° at a rate of 2°/min. Lebail / Rietveld refinements of the lattice were made with EXPGUI[91].

5.3.4 ^{17}O Single-Pulse (SP) MAS NMR

^{17}O NMR spectra were obtained on a 500 MHz (11.7 T) Varian Infinityplus spectrometer operating at 67.75 MHz for ^{17}O using a T3 HX probe configured for 3.2 mm rotors. The rotor assembly consisted of ZrO_2 sleeves, with vespel tips and spacers. The solution ($\pi/2$) pulse width was set to 12μs (20.833 kHz B_1 field). 2μs pulses were used for quantitative solids acquisition[16], and the MAS rate was 23 kHz. The pulse delay was 10s to ensure full relaxation. Longer relaxation delays did not result in intensity increases. Approximately 53000 acquisitions were collected for both samples. Chemical shifts were measured relative to the natural abundance ^{17}O signal in tap water, set to 0 ppm.

5.3.5 ^{31}P Single Pulse NMR

Solid-state ^{31}P NMR spectra were obtained on a ChemMagnetics 500 MHz (11.7 T) spectrometer operating at 202.318 MHz for ^{31}P at a spinning rate of 8 kHz, using a T3

HX probe configured for 5 mm rotors. The rotor assembly consisted of ZrO_2 sleeves, Kel-F tips, and PTFE spacers. The ^{31}P pulse width (pi/2) was 5μs, and the steady-state relaxation delay was 30s. 20 scans were collected for all samples. Chemical shifts were measured relative to the phosphate resonance in stoichiometric hydroxylapatite, set to δ_P = 2.65 ppm.

5.3.6 $^{1}H\{^{31}P\}$ REDOR NMR

Solid-state $^{1}H\{^{31}P\}$ REDOR NMR spectra were obtained on a Varian Infinity Plus 500 MHz (11.7 T) spectrometer operating at 499.7845 MHz for ^{1}H and 202.311 MHz for ^{31}P at a spinning rate of 8 kHz, using a low ^{1}H background probe with an alumina spinning assembly configured for 5 mm (OD) rotors. The 90° ^{1}H pulse width was 5μs, and the relaxation delay was 2s. 10μs 180° pulses were applied to ^{31}P every half-rotor period for 8ms (64 rotor periods), which was sufficient to attenuate intensity from ^{1}H signals coupled to ^{31}P. 400 scans were collected for each sample investigated.

5.4 Results

5.4.1 Powder X-Ray Diffraction (PXRD)

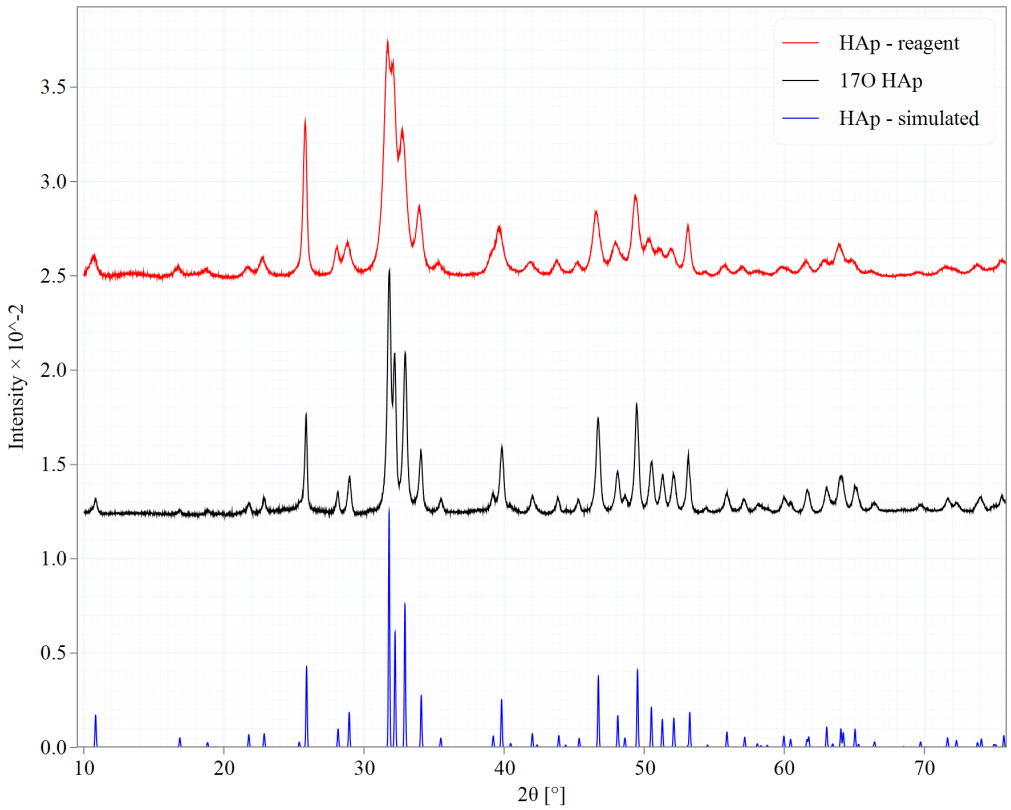

Figure 49: PXRD patterns of reagent-grade HAp shown in red, and after ^{17}O-enrichment, shown in black. Simulated spectrum from Hughes et al.[45] shown in blue

Experimental PXRD patterns of HAp before and after ^{17}O-enrichment are shown in red and black respectively, in Figure 49. Shown in blue is a simulated pattern generated from the structure data of Hughes et al. [45]. The positions and intensities of the observed reflections are in good agreement with the calculated pattern, indicating that the ^{17}O enrichment process did not modify the hydroxylapatite (HAp) structure or introduce significant amounts of an impurity phase. However, analysis of the peak shapes in the experimental PXRD patterns reveals significant differences in width. The

width of the 002 reflection is reduced by about a factor of two after the hydrothermal enrichment reaction, shown in the right-most column of Table 21. This reflection was selected because of its prominence and isolation from other reflections. The observed change in peak width may be indicative of recrystallization during ^{17}O enrichment. The lattice parameters obtained via LeBail refinement are shown in Table 21. As a result the hydrothermal treatment, the *a* lattice parameter is reduced 0.0037 Å, the *c* lattice parameter is increased 0.0139 Å, and the unit cell volume is increased by 0.64 $Å^3$. The reported changes in lattice parameters may simply be a result of more precise calculation of reflection positions, as the reflections in the HAp PXRD pattern prior to ^{17}O enrichment are broad relative to those after enrichment.

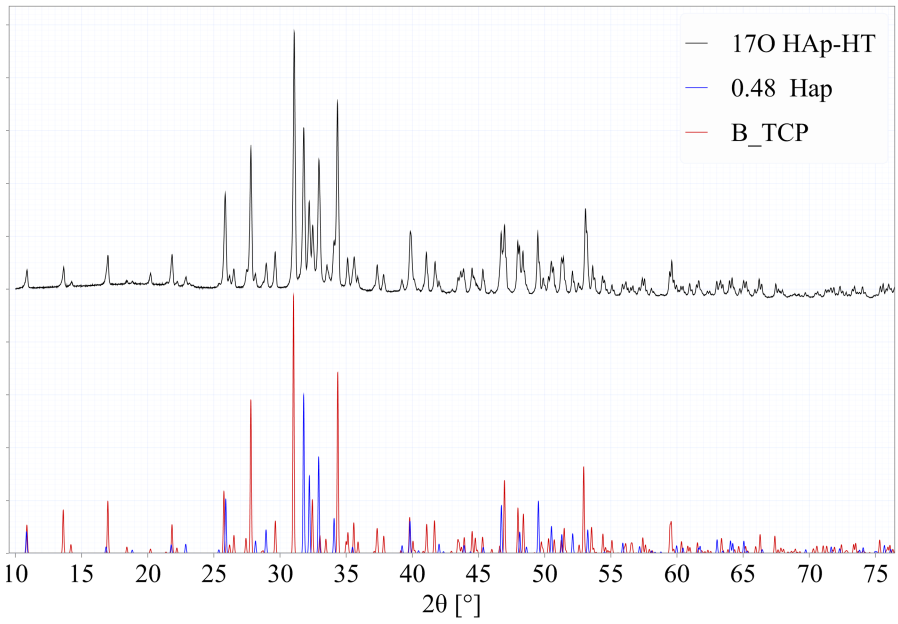

Figure 50: PXRD patterns of hydroxylapatite after heat treatment shown in black. In blue is a simulated hydroxylapatite pattern from Hughes et al.,[45] and in red is a simulated β-Tricalcium phosphate (TCP) pattern taken from Yashima et al.[92]

PXRD analysis of the ^{17}O-HAp after heat treatment under vacuum is shown in Figure 50, labeled ^{17}O HAp-HT. The experimental pattern, shown in black in Figure 50,

differs significantly from the patterns depicted in Figure 49. The simulated pattern shown in blue and red at the bottom of Figure 50 is a sum of those for HAp (blue) and β-tricalcium phosphate (β-TCP) (red). The close correspondence between the simulated composite pattern and the observed pattern indicates that a significant amount of HAp decomposed during the heat treatment, forming β-TCP. Presumably formation of TCP would proceed *via*:

$$2\ Ca_5(PO_4)_3OH \rightarrow 3\ Ca_3(PO_4)_2 + CaO + H_2O$$

However, neither CaO nor $Ca(OH)_2$ (possibly formed by hydration of CaO under ambient conditions) were observed to correspond to any experimental reflections. It is possible that the Ca-rich phase formed as a result of HAp decomposition is amorphous.

Sample	*a* (Å)	*c* (Å)	*Vol* (Å^3)	*Chisq*	*wRp*	*FWHM 002* (2θ)
HAp	9.4203(2)	6.8727(2)	528.19(2)	8.31	0.07	0.162
^{17}O HAp	9.41661(7)	6.88661(9)	528.83(1)	2.38	0.032	0.084
HAp-HT	9.4183(2)	6.8847(2)	528.89(2)	27.5	0.107	

Table 21: Results of LeBail refinements for HAp before and after ^{17}O enrichment, Rietveld refinement of heat-treated HAp

The results of LeBail refinements of HAp before and after enrichment and Rietveld refinement of the heat-treated, ^{17}O-enriched HAp (HAp-HT) are shown in Table 21. Rietveld refinement provides fits of intensity, and offered better resolution of overlapping reflections from HAp and β-TCP phases in HAp-HT. The quality of the fit is poor for HAp-HT, but despite the poor resolution, it is apparent that the lattice parameters of the apatite phase do not change significantly as a result of heat treatment. Trombe and Montel [77] reported a 0.007 Å reduction in the *a* lattice parameter and a 0.023 Å increase in the *c* lattice parameter between HAp and Oxyapatite. The lattice parameter changes in the present results oppose those of the previous work and are of smaller magnitude; the *a* lattice parameter increases 0.0017 Å, and the *c* lattice parameter

decreases 0.0019 Å upon heating, suggesting that the structural changes reported by Trombe and Montel [77] differ from those observed here. Refinement of the relative contribution of the HAp and β-TCP phases reveals a molar ratio of HAp:TCP of 1:1.

5.4.2 ^{17}O NMR Spectroscopy

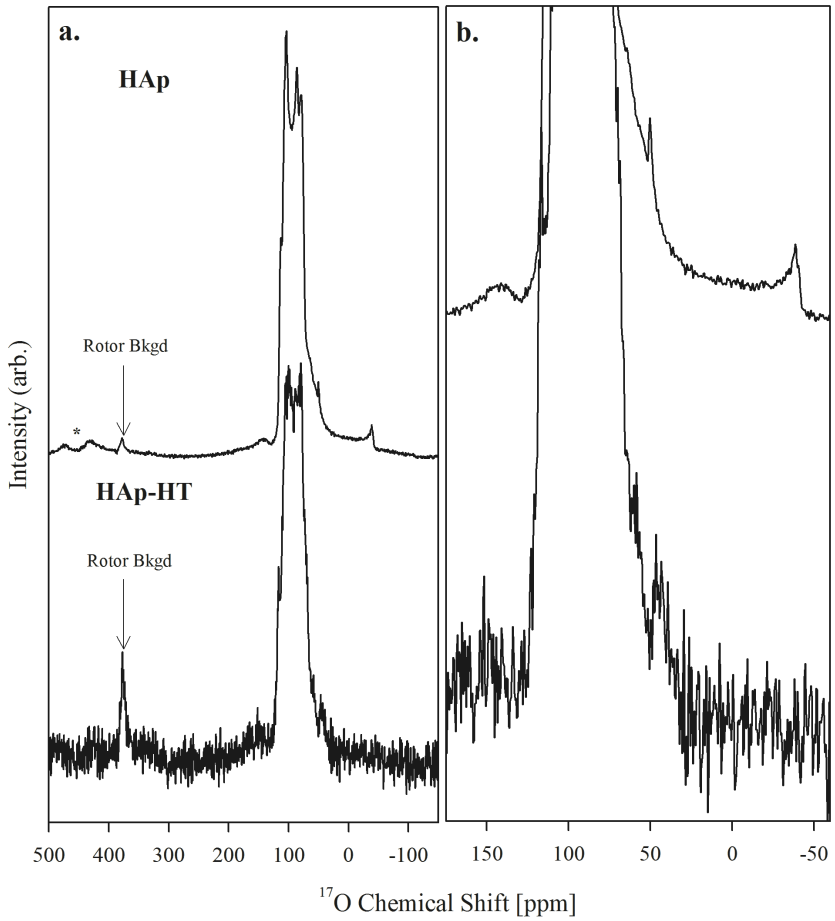

Figure 51: ^{17}O SP MAS NMR Spectra of HAp and HAp-HT. Spinning side-bands (SSBs) denoted with an asterisk. Background due to natural ^{17}O abundance in ZrO_2 rotors was determined by running a blank rotor under identical acquisition conditions.

^{17}O single-pulse (SP) MAS NMR spectra of both HAp and heat-treated hydroxylapatite (HAp-HT) are shown in Figure 51. The ^{17}O NMR spectrum of HAp features a prominent set of signals between δ = 79 and 113 ppm, which have the appearance of two pairs of 'horns' from second-order quadrupolar powder patterns.

These signals appear at δ = 113, 104, 86 and 79 ppm. Another set of horns with much lower intensity are observed at lower chemical shifts, at 50 and -38 ppm, plus an edge feature at -100 ppm. These lower intensity signals are shown more clearly at expanded vertical scale in Figure 51b. Two broad shoulders are observed on either side of the signals between 79 and 113 ppm, at 65 and 143 ppm, and a set of spinning side bands from the signals between 79 and 113 ppm is observed between 400 and 500 ppm. A sharp signal is observed at 378 ppm, which also occurs in the spectrum of the empty rotor and is assigned to background signal from natural ^{17}O abundance in the ZrO_2 rotors used in this work. Similar ^{17}O chemical shifts have been previously reported for ZrO_2 rotors and comparable materials[93], [94]. Signal at 378 ppm due to ZrO_2 background may have also been inappropriately assigned to oxide ions in apatite by Panchmatia et al. [80], however these authors did not provide a description of rotor materials.

The ^{17}O NMR spectrum of HAp-HT also features a set of prominent signals in a comparable spectral region to that of HAp, between 116 and 79 ppm. However unlike in the ^{17}O NMR spectrum of HAp, the signals in this spectral region are much weaker and poorly resolved so distinct sets of horns cannot be identified. Additionally, the overall the signal to noise in the spectrum of HAp-HT is markedly worse than that in the spectrum of HAp. The features observed at lower chemical shift at 50 and -38 ppm in HAp are not present in the spectrum of HAp-HT. A very weak broad signal is apparent near 44 ppm (illustrated most clearly in the lower spectrum of Figure 51b), however due to the poor signal to noise it is difficult to identify this spectral feature definitively above noise. The broad signals observed at 65 and 143 ppm for HAp are also present for HAp-HT, at comparable chemical shifts. Spinning side bands are not apparent, probably due

to the poor signal to noise in this spectrum. The rotor background signal at +378 ppm is much more prominent in the spectrum of HAp-HT than for HAp. Assuming the amount of ^{17}O in each rotor is comparable, the increased intensity of the rotor background signal suggests that the signal due to the sample is much weaker in HAp-HT than in HAp, presumably due to a decline in isotopic enrichment from heating. Both rotors were completely filled with powder, so it is unlikely this difference is due to variation in amount of sample.

Pourpoint et al.[88] calculated ^{17}O NMR parameters for HAp and other biomaterials from first-principle calculations. The quadrupolar coupling paramters (C_Q and η) and isotropic chemical shifts for the 12 inequivalent phosphate oxygens and column hydroxyl gor HAp are reproduced in Table 22. Using a home-grown quadurpolar fitting program, a simulated spectrum was generated from these NMR parameters, shown in Figure 52. The twelve unique phosphate oxygen sites in the HAp crystal structure give ^{17}O signals with isotropic chemical shifts between 109 and 125 ppm, and C_Q values in a narrow range between 4.3 and 4.9 MHz. The large quadrupolar coupling constants of these sites should yield overlapping second order powder patterns. The sum of the signals from these sites is characterized by prominent horns at 96 and 78 ppm, and a broad shoulder at 60 ppm. The calculated parameters for the hydroxyl yield a well-resolved set of horns at 7 and -96 ppm, and an edge at -180 ppm. The intensity ratio of phosphate to hydroxyl reflects the 12:1 stoichiometric ratio, assuming uniform ^{17}O isotopic composition.

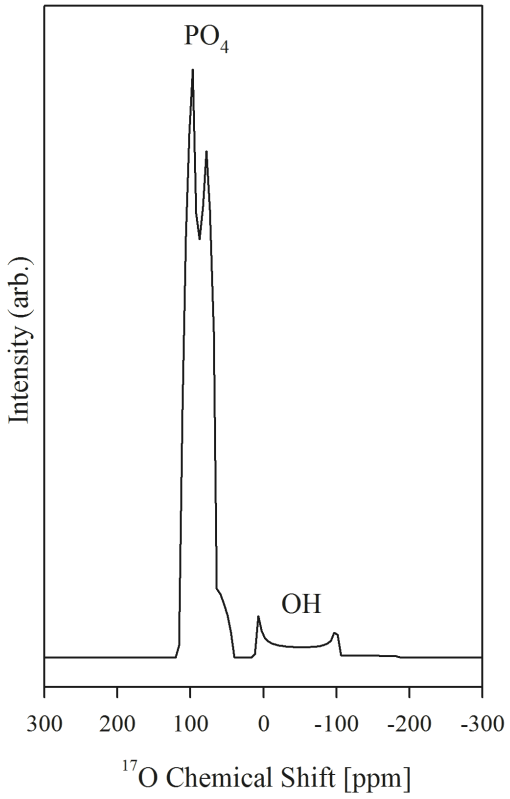

Figure 52: Simulated ^{17}O NMR spectrum of HAp from parameters published in Pourpoint et al.

δ_{ISO} (ppm)	C_Q (MHz)	η	*Assignment*
116.9	4.6	0.2	PO_4
119.5	4.7	0.2	
123.0	4.9	0.2	
121.6	4.5	0.1	
117.1	4.3	0.1	
124.5	4.7	0.1	
116.0	4.7	0.2	
109.7	4.5	0.1	
114.3	4.6	0.2	
109.7	4.4	0.1	
113.2	4.5	0.2	
113.0	4.6	0.1	
41.9	8.3	0.0	OH

Table 22: ^{17}O NMR Parameters reported by Pourpoint et al.[88]

The simulated spectrum based on the work of Pourpoint et al in Figure 52 closely resembles the ^{17}O NMR spectrum collected for HAp in Figure 51. We therefore assign the set of horns in the experimental NMR spectrum between 113 and 79 ppm to

phosphate oxygens, and the less-prominent set of horns observed at 50 and -38 ppm and edge at -100 ppm to hydroxyl oxygens. The shoulder observed experimentally at 65 ppm is attributed to the phosphate quadrupolar line shape, and the slight signal at 143 ppm is attributed to the center band of a satellite transition spinning side band manifold.

The overall shape and distance between the horns due to hydroxyl oxygens in the ^{17}O NMR spectrum of HAp is close to that in the simulated spectrum (88 and 89 ppm, respectively), which suggests that both the calculated quadrupolar coupling constant (C_Q) and the asymmetry parameter ($\eta = 0$) by Pourpoint et al.[88] are accurate. However, the positions of the horns observed experimentally appear 45 ppm higher than the calculated horns, which suggests the calculated isotropic chemical shifts may be inaccurate. Calculation of isotropic chemical shifts has proven a challenge in first principles calculations, owing to the strong dependence on excited states and thus on basis set selection on chemical shift.

The distance between the simulated and experimentally obtained horns due to the hydroxyl group exhibit some differences. In the experimental ^{17}O NMR spectrum these features are separated by ~34 ppm, however in the simulated spectrum they are only 18 ppm apart, suggesting significant differences in quadrupolar coupling constant between experiment and theory.

5.4.3 ^{31}P NMR Spectroscopy

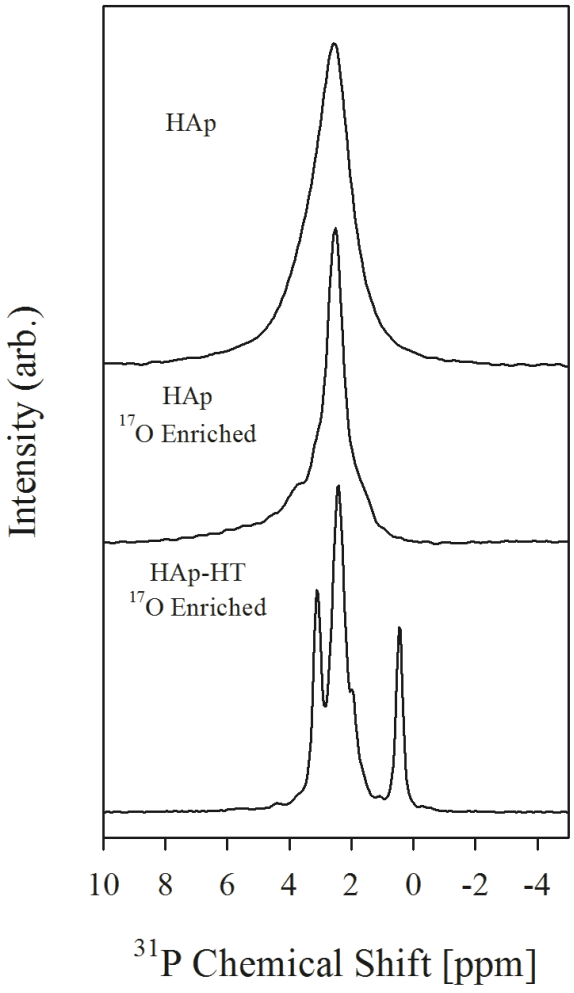

Figure 53: ^{31}P MAS NMR Spectra of HAp, ^{17}O enriched HAp, and heat-treated ^{17}O enriched HAp

HAp		
^{31}P Chemical Shift (ppm)	FWHM (ppm)	Relative Intensity
2.6	1.5	1
HAp ^{17}O enriched		
2.5	0.7	0.87(3)
4.0	1.5	0.13(7)
HAp-HT ^{17}O enriched		
0.4	0.3	0.16(5)
1.9	0.3	0.08(6)
2.4	0.5	0.55(3)
3.1	0.3	0.22(4)

Table 23: ^{31}P NMR Parameters

^{31}P single-pulse (SP) NMR spectra are shown in Figure 53, and results of least-squares fitting to a sum of Gaussian curves is shown in Table 23. The ^{31}P spectrum of HAp features a single, broad resonance at 2.6 ppm due to phosphate groups in HAp, in good agreement with the literature [34]. After hydrothermal ^{17}O enrichment, the peak position remains the same, however the width of the peak is reduced by a factor of two, and another signal is apparent at 4.0 ppm. The ^{31}P NMR spectrum of ^{17}O enriched HAp after heat treatment is markedly different. The signal tentatively assigned to phosphate groups within HAp is still present, at 2.4 ppm, and three additional peaks are now observed at 0.4, 1.9, and 3.1 ppm.

5.4.4 $^{1}H\{^{31}P\}$ REDOR NMR Spectroscopy

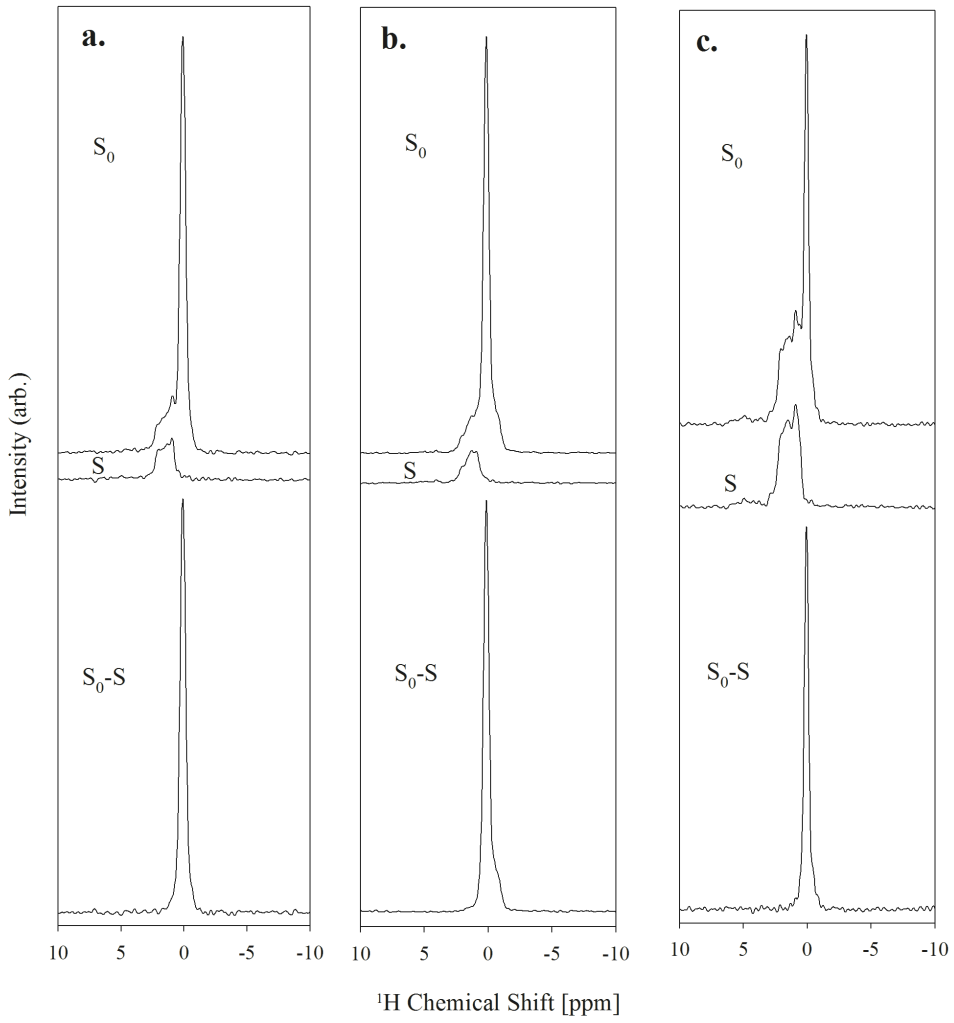

Figure 54: S_0, S, and S_0-S spectra from the $^1H\{^{31}P\}$ REDOR experiment. a. HAp b. HAp ^{17}O enriched and c. HAp-HT ^{17}O enriched

HAp		
^1H Chemical Shift (ppm)	FWHM (ppm)	REDOR Fraction $(S_0\text{-}S)/S_0$
0.1	0.5	1
0.9	0.6	0.12(2)
1.7	1.2	
HAp ^{17}O enriched		
-0.7	0.7	1
0.1	0.5	1
1.2	0.5	0.22(1)
2.1	1.3	
HAp-HT ^{17}O enriched		
0.1	0.4	1
0.8	0.5	0.06(1)

1.8	1.2	

Table 24: $^{1}H\{^{31}P\}$ REDOR Results

Figure 54a, b and c demonstrate the important components of the REDOR[18] experiment for the samples analyzed in the present work. The upper-most spectrum (S_0) is the result of a spin-echo experiment, which shows signal from all ^{1}H in the sample, with the exception of signals with short T_2 that are not refocused during the spin echo sequence. The middle spectrum (S) results from an identical ^{1}H spin-echo sequence, but ^{31}P pulses are applied every half-rotor period, which reintroduces heteronuclear ^{1}H-^{31}P dipolar coupling and attenuates those signals coupled to ^{31}P. Comparison of S_0 and S spectra provides resolution of those ^{1}H sites that are due to phosphate phases from impurities and background signal. The bottom spectrum (S_0-S) is the REDOR difference spectrum, obtained by subtracting the attenuated spin echo (S) from the unperturbed spin echo (S_0). This spectrum shows peaks only from ^{1}H environments that in close proximity to ^{31}P.

Three signals are resolved in the S_0 spectrum of HAp (Figure 54a), at 0.1, 0.9 and 1.7 ppm. The peak at 0.1 ppm closely resembles previous reports of hydroxyl groups in hydroxylapatite at 0.2 ppm[33], and the REDOR experiment indicates that this signal is indeed coupled to phosphorus nuclei. This signal is not present in the S spectrum, dominates the REDOR difference spectrum, and yields a REDOR fraction of unity (Table 24). The resolution between the other two peaks at higher chemical shift is poor, and as a result their intensities have been combined to mitigate errors associated with poor fitting. These signals are present in spectra of all three samples with minor variations in chemical

shift, and their intensities were combined similarly. The intensity from these signals is only 12% greater in the S_0 spectrum than in the S spectrum, shown in Table 24**.** The similar intensity of these peaks in the S_0 and S spectra indicates that they are probably not associated with phosphorus atoms.

The S_0 spectrum of the ^{17}O enriched HAp (upper-most spectrum in Figure 54b) features four peaks, the most prominent of which occurs at 0.1 ppm. As for the S_0 spectrum of HAp this signal is assigned to hydroxyl groups in hydroxylapatite. This resonance at 0.1 ppm is not present in the S spectrum and dominates the REDOR difference spectrum due to coupling to nearby phosphates. An additional signal occurs at -0.7 ppm that similar to the 0.1 ppm peak is completely attenuated in the S spectra, shown by a REDOR fraction = 1 in Table 24 and its appearance in the REDOR difference spectrum (Figure 54b, bottom). This result suggests strongly that the corresponding ^{1}H are associated with phosphorus atoms. Signals at greater chemical shift (1.2 and 2.1 ppm) similar to those of HAp are also observed in the ^{17}O enriched HAp S_0 spectrum with comparable intensity (12% vs 22%).

There are three signals in the S_0 spectrum of heat-treated ^{17}O enriched HAp, at 0.1, 0.8 and 1.8 ppm. This spectrum appears similar to that of HAp prior to ^{17}O enrichment, however the intensity ratio between the signal at 0.1 ppm (assigned to column hydroxyl groups and the two signals at greater chemical shift is much smaller than those of the previous samples. The signal at 0.1 ppm is not observed in the S spectrum, indicating that these ^{1}H nuclei are coupled to phosphorus atoms. The intensity signals at greater

chemical shift (0.8 and 1.8 ppm) in the S_0 and S spectra are comparable, differing only by 6% suggesting that these signals are not associated with phosphorus atoms.

5.5 Discussion

5.5.1 ^{17}O Enrichment

The present PXRD and ^{31}P results indicate that the hydrothermal ^{17}O isotopic enrichment of HAp involved dissolution and recrystallization. Improved crystallinity is evident from the 50% reduction in both width of the 002 PXRD reflection and the ^{31}P phosphate NMR line width. The ^{17}O NMR spectrum of HAp reveals ^{17}O signals from both phosphate oxygens and hydroxyl groups. The signal intensity ratio is in good agreement with the stoichiometric phosphate oxygen: hydroxyl oxygen ratio of 12:1. This observation indicates that isotopic enrichment is nearly uniform and did not preferentially enrich hydroxyl over phosphate oxygen, which might be expected if enrichment proceeded *via* a solid-state process. The experimental ^{17}O line shapes correspond reasonably well with calculated spectra based on the work from Pourpoint et al.[88], although there appear to be some differences in the detailed ^{17}O NMR parameters.

5.5.2 Effect of Heat-Treatment on HAp

PXRD analysis indicates that a significant fraction (~50% of total X-ray intensity) of β tricalcium phosphate (TCP) forms upon heat treatment at 850°C under vacuum. The most likely explanation for this result is decomposition of HAp into β-TCP and a Ca phase such as CaO or $Ca(OH)_2$. However the prominent PXRD reflections expected for

these phases (i.e. the 002 and 022 reflections for CaO at 37.3 and 53.7° 2θ respectively, and the 001 and $01\bar{1}$ reflections for portlandite, $Ca(OH)_2$, at 18.3 and 34.3° 2θ, respectively) were not observed indicating that this Ca phase may be X-ray amorphous. In addition, the lattice parameters for the remaining apatite phase did not change markedly upon heat treatment, which indicates that this phase is probably still hydroxylapatite, not oxyapatite.

Decomposition of HAp into β-TCP is further supported in the NMR data. The ^{17}O NMR spectrum of HAp after heat treatment reveals poorly defined features in the phosphate oxygen spectral region between 79 and 113 ppm, indicative of a greater number of phosphate oxygen environments than in HAp, which would be expected upon formation of β-TCP. The ^{31}P NMR spectrum of HAp-HT features three additional signals, which are not believed to be associated with HAp, at 0.4 , 1.9 and 3.1 ppm. The structure of β-TCP features three inequivalent phosphate sites, which were reported to have chemical shifts of 0.0, 1.3, and 4.5 ppm by Marchandise et al.[95], values comparable to the present signals. The multiplicities of the three sites in β-TCP are 3:3:1, which do not match the fitted intensity from the ^{31}P signals, which is roughly 2:1:2.75 for the 0.4, 1.9 and 3.1 ppm signals respectively. The difference between the observed and expected signal intensity for the ^{31}P signals attributed to β-TCP may be due in part to overlapping intensity from the prominent HAp phosphate signal. Combining the ^{31}P intensity for these three signals reveals that 45% of the ^{31}P intensity is due to β-TCP. By normalizing for stoichiometry (3 phosphorus atoms per formula unit (apfu) in HAp, 2 P apfu in β-TCP) the HAp: β-TCP molar ratio is then 1.2:1, which is comparable within

reasonable expectation of error to the 1:1 HAp: β-TCP molar ratio determined by Rietveld refinement.

The ^{1}H resonances in the S_0 $^{1}H\{^{31}P\}$ REDOR spectra at chemical shifts greater than that for column hydroxyl (0.8-1.2 and 1.7-2.1 ppm) are believed to be background signals, as they are not observed in REDOR difference spectra. The fact that the intensity of these signals in the S_0 and S spectra does not precisely match (REDOR fractions of 0.12, 0.22, and 0.06 for HAp, ^{17}O HAp and ^{17}O HAp-HT, respectively) is most likely due to poor fitting of trailing intensity of the hydroxylapatite ^{1}H signal toward higher chemical shift. This intensity is incorrectly attributed to the signals at greater chemical shift in the S_0 spectrum, therefore giving rise to the reported differences. The intensity of this background signal can be assumed to remain largely unchanged in the S_0 spectra between different samples. Therefore, the absolute intensity of the hydroxylapatite ^{1}H peak at 0.1 ppm can be approximated by comparison of its intensity to that of the signals at higher chemical shift. The result of this calculation is reported in Table 25, and demonstrates that the intensity of the hydroxylapatite ^{1}H signal at 0.1 ppm remains constant before and after hydrothermal ^{17}O enrichment. However the hydroxyl peak intensity is significantly reduced as a result of heat treatment under vacuum. This observation suggests that the amount of HAp present is reduced as a result of heat treatment, presumably due to the decomposition of HAp into β-TCP and an amorphous Ca phase.

Sample	Intensity ratio 0.1 ppm : 0.8-1.7 ppm
HAp	3.6
^{17}O HAp	3.7
^{17}O HAp-HT	0.9

Table 25: Intensity ratio of hydroxylapatite:background signal in S_0 spectra

In addition to the possibility of HAp decomposition into β-TCP and an amorphous Ca phase, it is apparent that heat treatment also reduces ^{17}O isotopic enrichment, particularly for hydroxyl oxygens, which could not be detected in the ^{17}O NMR spectrum. Decomposition of HAp and formation of TCP should not affect the phosphate ^{17}O signal intensity, because signals from both phases appear in a comparable spectral region. However, the signal to noise ratio for the phosphate oxygens is markedly poorer in HAp-HT, suggesting that in addition to HAp decomposition, loss of isotopic ^{17}O enrichment has occurred as well. It is unlikely that isotopic enrichment was to ambient, given that both heat treatment of the sample and temperature ramp up and cool down were all performed under vacuum. The most probable explanation is oxygen exchange with the quartz glass tubing encapsulating the sample.

5.5.3 Formation of Oxyapatite (OAp)

The presence of oxide ion (O^{2-}) in apatite could not be definitively identified, owing principally to the decomposition of HAp upon heating into β-TCP and loss of ^{17}O via exchange with surrounding materials. The concentration of hydroxyl ^{1}H approximated by ^{1}H NMR suggests that the loss of OH is greater than the extent of decomposition of HAp into β-TCP (75% loss of hydroxyl vs 50% decomposition into β-TCP), which may be the result of a small amount oxy-component in the remaining apatite.

5.5.4 Future work

The present results show that hydrothermal treatment is a viable means of ^{17}O enrichment in HAp. The ^{17}O NMR spectrum of hydrothermally-treated ^{17}O HAp shows

distinct resonances for both phosphate and hydroxyl oxygens, whose relative intensities match that the stoichiometric ratio, indicating that enrichment is uniform for both sites. Heat-treatment under vacuum resulted in the formation of a significant amount of β-TCP, presumably due to decomposition of HAp. Loss of ^{17}O enrichment was also a consequence of heat-treatment, as indicated in the poor signal to noise in the ^{17}O NMR spectrum of heat-treated HAp. Enrichment was presumably lost by exchange with surrounding quartz glass.

The presence of oxyapatite could be more definitively addressed if decomposition of HAp into β-TCP could be prevented. Future efforts performing heat-treatment at lower temperature should minimize this process, thereby providing a more simple comparison of sample before and after heat treatment. Preventing oxygen exchange with the surrounding quartz glass tubing is more difficult, although the extent of exchange will presumably be diminished at lower temperature.

In the present work ^{1}H NMR intensity was approximately quantified by comparison of hydroxyl signal to that of rotor background. More precise quantitative ^{1}H NMR methods (such as those described by Vaughn et al.[61]) would provide a more accurate measure of HAp decomposition than the present method, by approximating hydroxylapatite ^{1}H signal relative to background.

The isotopic enrichment of the starting material (30% ^{17}O H_2O) used in this work was far less than that used in Panchmatia et al. (90% ^{17}O H_2O), so repetition of the above

experiments with higher starting ^{17}O content may provide definitive detection of the oxide ion in Oxyapatite. Additionally heat treatment at a lower temperature should minimize both the extent of decomposition of HAp into TCP and loss of enrichment.

Chapter 6: Conclusions and future work

6.1 Concluding remarks

In the realm of structural analysis, today's research frontiers cannot be sufficiently explored as they often were in decades past, using only a laboratory X-ray diffractometer. There exists no singular, 'silver bullet' characterization technique – scientists investigating atomic arrangements in materials pertinent to 2016 must utilize a suite of techniques of ever-increasing complexity. Mastery of several characterization techniques by an individual is simply not feasible; therefore collaboration with different specialists is more important than ever. In this thesis I believe I have investigated atomic arrangements in apatite in such a fashion, utilizing not only solid-state NMR as it is my focus, but also X-ray diffraction methods and vibrational spectroscopy. As a result I am very grateful to Bill Woerner and Michael Thorpe for their assistance in collection and interpretation of PXRD and vibrational spectroscopy data.

Every major finding in this work was either dependent upon or bolstered by results from other analytical methods. In Chapter 2, the presence of AB-type carbonate apatite in 13CHAP-1.43 and 13CHAP-1.67(2x) was evident not only from the $^{13}C\{^{1}H\}$ cross-polarization spectra, but also from changes in lattice parameters determined via Lebail refinement of PXRD data, and vibrational spectroscopy. In Chapter 3 the absence of oxyapatite component and relatively minimal variation in hydroxyl concentration across samples was demonstrated by linear variation in lattice parameters from PXRD. Showing these samples to be dominantly F,Cl and feature nominal oxy and hydroxyl component was crucial to further investigation in Chapter 4. The major finding from

Chapter 4 was calculation of fluorine atomic positions from ^{19}F chemical shifts, and the metal-fluoride distances in the alkaline fluoride standards used to calculate atomic positions were determined by X-ray diffraction. In chapter 5, definitive identification of β-TCP (and identification of the three corresponding ^{31}P NMR signals) would not be possible without PXRD.

Solid-state NMR has proven to be a viable characterization method for the complex types of atomic substitutions found in apatite. Such atomic substitutions and associated structural changes, whether they be disordered fluorine atomic positions or minor concentrations of carbonate, are important to bulk structure and properties. While conventional characterization techniques could not provide the level of insight that solid-state NMR analysis has provided here, it is important to emphasize that interpretation of solid-state NMR data is also dependent upon these other methods of characterization.

6.2 Future work

Brian mentioned while we were discussing the ^{17}O NMR work in Chapter 5 that he "wished we had another year". While I *personally* do not want to delay my postdoctoral position another year and stay at Stony Brook, I agree with Brian's assessment that this work is incomplete, and would like to see a second iteration of experiments. Definitive assessment of the presence of oxyapatite, whether positive or negative, has far-reaching impact for the biomaterials community that utilizes sintered HAp powders and for the geochemistry community interested in accurate chemical analysis of binary or ternary apatites. This could be done by starting with a laboratory-synthesized HAp, which would be more crystalline and could be assured to be

stoichiometric, and by performing control heating experiments without ^{17}O enrichment in order to determine the optimal conditions for HAp conversion into OAp while minimizing formation of β-TCP.

In addition, I believe the work pertaining to carbonate hydroxylapatite and its relation to bone mineral could be investigated further. Melinda Duer recently published a discussion on the application of solid-state NMR applied to bone and related bone materials[96], and highlighted many of the triumphs of solid-state NMR spectroscopy in this field. Solid-state NMR analysis of both native bone and its synthetic analogues could yield very impactful work, relevant to both the medical and biomaterials communities. With regard to the present work, synthesis of identical hydroxylapatite samples without carbonate would indicate whether the ^{1}H NMR signals with higher chemical shifts are due to carbonate substitutions, or simple variation of Ca:P ratio. In addition, collection of REDOR and cross polarization spectra at a greater number of dephasing and contact periods would allow for kinetic analysis, which could provide interatomic distances.

Chapter 8: References

[1] P. M. Piccoli and P. A. Candela, "Apatite in Igneous Systems," *Reviews in Mineralogy and Geochemistry*, vol. 48, no. 1, pp. 255–292, Jan. 2002.

[2] K. A. Farley and D. F. Stockli, "(U-Th)/He Dating of Phosphates: Apatite, Monazite, and Xenotime," *Reviews in Mineralogy and Geochemistry*, vol. 48, no. 1, pp. 559–577, 2002.

[3] T. M. Harrison, E. J. Catlos, and J. M. Montel, "U-Th-Pb Dating of Phosphate Minerals," *Reviews in Mineralogy and Geochemistry*, vol. 48, no. 1, pp. 524–558, 2002.

[4] Y. Pan and M. E. Fleet, "Compositions of the Apatite-Group Minerals: Substitution Mechanisms and Controlling Factors," *Reviews in Mineralogy and Geochemistry*, vol. 48, no. 1, pp. 13–49, 2002.

[5] J. Xu, X. Wang, H. Fu, C. M. Brown, X. Jing, and F. Liao, "Solid-State 29Si NMR and Neutron-Diffraction Studies of Sr0. 7K0. 3SiO2. 85 Oxide Ion Conductors," *Inorganic Chemistry*, vol. 53, no. 13, pp. 6962–6968, 2014.

[6] S. Chen and Y. Wu, "New opportunities for transparent ceramics," *American Ceramic Society Bulletin*, vol. 92, no. 2, pp. 32–38, 2013.

[7] H. Li, T. Baikie, S. S. Pramana, J. F. Shin, P. R. Slater, F. Brink, J. Hester, K. Wallwork, and T. J. White, "Synthesis and characterisation of vanadium doped alkaline earth lanthanum germanate oxyapatite electrolyte," *Journal of Materials Chemistry*, vol. 22, no. 6, pp. 2658–2669, 2012.

[8] L. Malavasi, C. A. J. Fisher, and M. S. Islam, "Oxide-ion and proton conducting electrolyte materials for clean energy applications: structural and mechanistic features," *Chemical Society Reviews*, vol. 39, no. 11, p. 4370, 2010.

[9] S. Warner, R. F. Martin, A.-F. M. Abdel-Rahman, and R. Doig, "Apatite as a Monitor of Fractionation, Degassing, and Metamorphism in the Sudbury Igneous Complex, Ontario," *The Canadian Mineralogist*, pp. 981–999, 1998.

[10] R. A. Young, W. V. D. Lugt, and J. C. Elliott, "Mechanism for Fluorine Inhibition of Diffusion in Hydroxyapatite," *Nature*, vol. 223, no. 5207, pp. 729–730, 1969.

[11] R. K. Harris and M. J. Duer, *NMR Crystallography*. 2012, pp. 1–524.

[12] D. D. Laws, H.-M. L. Bitter, and A. Jerschow, "Solid-State NMR Spectroscopic Methods in Chemistry," *Angewandte Chemie International Edition*, no. 41, pp. 3096-3129, 2002.

[13] J. Feng, "Intrinsic hydrated defects in $CaCO_3$: a solid state NMR spectroscopic study," *Ph.D thesis*, Stony Brook Univeristy, 2009.

[14] G. E. Pake, "Nuclear Resonance Absorption in Hydrated Crystals: Fine Structure of the Proton Line," *Journal of Chemical Physics*, vol. 16, no. 4, pp. 327–11, 1948.

[15] S. E. Ashbrook, "Introduction To Quadrupolar NMR," 2008, pp. 1–41, http://www.solidstatenmr.org.uk/lectures_files/pdfs/QuadrupolarNMR.pdf.

[16] T. Bräuniger and M. Jansen, "Solid-state NMR Spectroscopy of Quadrupolar Nuclei in Inorganic Chemistry," *Zeitschrift für anorganische und allgemeine*

Chemie, vol. 639, no. 6, pp. 857–879, 2013.
[17] N. E. Jacobsen, *NMR spectroscopy explained: simplified theory, applications and examples for organic chemistry and structural biology*. 2007.
[18] T. Gullion and J. Schaefer, "Rotational-echo double-resonance NMR," *Journal of Magnetic Resonance*, vol. 213, no. 2, pp. 413–417, 1989.
[19] M. E. Fleet, *Carbonated Hydroxyapatite*. CRC Press, 2015.
[20] L. M. Miller, V. Vairavamurthy, and M. R. Chance, "In situ analysis of mineral content and crystallinity in bone using infrared micro-spectroscopy of the v_4 PO_4^{3-} vibration," *Biochimica et Biophysica Acta*, vol. 1527, no. 1, pp. 11–19, 2001.
[21] J. S. Nyman, A. Roy, X. Shen, R. L. Acuna, J. H. Tyler, and X. Wang, "The influence of water removal on the strength and toughness of cortical bone," *Journal of Biomechanics*, vol. 39, no. 5, pp. 931–938, 2006.
[22] L. T. Kuhn, M. D. Grynpas, C. C. Rey, Y. Wu, J. L. Ackerman, and M. J. Glimcher, "A Comparison of the Physical and Chemical Differences Between Cancellous and Cortical Bovine Bone Mineral at Two Ages," *Calcified Tissue International*, vol. 83, no. 2, pp. 146–154, 2008.
[23] I. R. Gibson and W. Bonfield, "Novel synthesis and characterization of an AB-type carbonate-substituted hydroxyapatite," *Journal of Biomedical Materials Research*, vol. 59, no. 4, pp. 697–708, 2001.
[24] G. Bonel, "Contribution a l'etude de lar carbonation des apatites These," *Annali di Chimica*, vol. 7, pp. 65–87, 1972.
[25] H. E. Mason, A. Kozlowski, and B. L. Phillips, "Solid-State NMR Study of the Role of H and Na in AB-Type Carbonate Hydroxylapatite," *Chemistry of Materials*, vol. 20, no. 1, pp. 294–302, 2008.
[26] B. H. Toby, "EXPGUI, a graphical user interface for GSAS," *Journal of Applied Crystallography*, vol. 34, no. 2, pp. 210–213, 2001.
[27] M. Wojdyr, "Fityk: a general-purpose peak fitting program," *Journal of Applied Crystallography,* vol. 43, no. 5, pp. 1126-1128, 2010.
[28] R. Z. LeGeros, "Effect of Carbonate on the Lattice Parameters of Apatite," *Nature*, vol. 206, pp. 403–404, 1965.
[29] R. M. Wilson, J. C. Elliott, and S. E. P. Dowker, "Rietveld refinement of the crystallographic structure of human dental enamel apatites," *American Mineralogist*, pp. 1406–1414, 1999.
[30] S. Liao, F. Watari, G. Xu, M. Ngiam, S. Ramakrishna, and C. K. Chan, "Morphological effects of variant carbonates in biomimetic hydroxyapatite," *Materials Letters*, vol. 61, no. 17, pp. 3624–3628, 2007.
[31] A. Krajewski, M. Mazzocchi, P. L. Buldini, A. Ravaglioli, A. Tinti, P. Taddei, and C. Fagnano, "Synthesis of carbonated hydroxyapatites: efficiency of the substitution and critical evaluation of analytical methods," *Journal of Molecular Structure*, vol. 744, pp. 221–228, 2005.
[32] C. Rey, B. Collins, T. Goehl, I. R. Dickson, and M. J. Glimcher, "The carbonate environment in bone mineral: A resolution-enhanced fourier transform infrared spectroscopy study," *Calcified Tissue International*, vol. 45, no. 3, pp. 157–164, 1989.
[33] J. P. Yesinowski and H. Eckert, "Hydrogen environments in calcium

phosphates: proton MAS NMR at high spinning speeds," *Journal of the American Chemical Society,* vol. 109, no. 21, pp. 6274–6282, 1987.

[34] W. P. Rothwell, J. S. Waugh, and J. P. Yesinowski, "High-resolution variable-temperature 31P NMR of solid calcium phosphates," *Journal of the American Chemical Society,* vol. 108, no. 8, pp. 2637-2643 1993.

[35] R. M. Wilson, S. E. P. Dowker, and J. C. Elliott, "Rietveld refinements and spectroscopic structural studies of a Na-free carbonate apatite made by hydrolysis of monetite," *Biomaterials*, vol. 27, no. 27, pp. 4682–4692, 2006.

[36] A. K. Cheetham, N. J. Clayden, C. M. Dobson, and R. J. B. Jakeman, "Correlations between ^{31}P NMR chemical shifts and structural parameters in crystalline inorganic phosphates," *Journal of the Chemical Society, Chemical Communications*, no. 3, pp. 195-197, 1986.

[37] K. Beshah, C. Rey, M. J. Glimcher, M. Schimizu, and R. G. Griffin, "Solid State Carbon-13 and Proton NMR Studies of Carbonate-Containing Calcium Phosphates and Enamel," *Journal of Solid State Chemistry*, vol. 84, pp. 71–81, 1990.

[38] E. E. Wilson, A. Awonusi, M. D. Morris, D. H. Kohn, M. M. J. Tecklenburg, and L. W. Beck, "Three Structural Roles for Water in Bone Observed by Solid-State NMR," *Biophysical Journal*, vol. 90, no. 10, pp. 3722–3731, 2006.

[39] R. M. Wilson, J. C. Elliott, S. E. P. Dowker, and L. M. Rodriguez-Lorenzo, "Rietveld refinements and spectroscopic studies of the structure of Ca-deficient apatite," *Biomaterials*, vol. 26, no. 11, pp. 1317–1327, 2005.

[40] C. H. Yoder, J. D. Pasteris, K. N. Worcester, and D. V. Schermerhorn, "Structural Water in Carbonated Hydroxylapatite and Fluorapatite: Confirmation by Solid State 2H NMR," *Calcified Tissue International*, vol. 90, no. 1, pp. 60–67, 2012.

[41] F. M. McCubbin, A. Steele, E. H. Hauri, H. Nekvasil, S. Yamashita, and R. J. Hemley, "Nominally hydrous magmatism on the Moon," *Proceedings of the National Academy of Sciences U.S.A.*, vol. 107, no. 25, pp. 11223–11228, 2010.

[42] E. Kendrick, M. S. Islam, and P. R. Slater, "Developing apatites for solid oxide fuel cells: insight into structural, transport and doping properties," *Journal of Materials Chemistry*, vol. 17, no. 30, pp. 3104-3111, 2007.

[43] J. Chen, Z. Yu, P. Zhu, J. Wang, Z. Gan, J. Wei, Y. Zhao, and S. Wei, "Effects of fluorine on the structure of fluorohydroxyapatite: a study by XRD, solid-state NMR and Raman spectroscopy," *Journal of Materials Chemistry B: Materials for biology and medicine*, vol. 3, no. 1, pp. 34–38, 2014.

[44] R. C. Ewing and L. Wang, "Phosphates as Nuclear Waste Forms," *Reviews in Mineralogy and Geochemistry*, vol. 48, no. 1, pp. 673–699, Jan. 2002.

[45] J. M. Hughes, M. Cameron, and K. D. Crowley, "Structural Variations in natural F, OH, and Cl apatites," *American Mineralogist*, vol. 74, pp. 870–876, 1989.

[46] J. M. Hughes and J. Rakovan, "The Crystal Structure of Apatite, $Ca_5(PO_4)_3(F,OH,Cl)$," *Reviews in Mineralogy and Geochemistry*, vol. 48, no.

1, pp. 1–12, 2002.
[47] R.D. Shannon, "Revised Effective Ionic Radii and Systematic Studies of Interatomic Distances in Halides and Chalcogenides," *Acta Crystallographica,* no. 32, pp. 751–767, 1976.
[48] F. M. McCubbin, H. E. Mason, H. Park, B. L. Phillips, J. B. Parise, H. Nekvasil, and D. H. Lindsley, "Synthesis and characterization of low-OH fluor-chlorapatite: A single-crystal XRD and NMR spectroscopic study," *American Mineralogist*, vol. 93, no. 1, pp. 210–216, 2008.
[49] "Crystal Structures of Natural Ternary Apatites: Solid solution in the $Ca_5(PO_4)_3X$ (X = F, OH, Cl) system," *American Mineralogist* vol. 75, pp. 295–304, 1990.
[50] J. C. Stormer, M. L. Pierson, and R. C. Tacker, "Variation of F and Cl X-ray intensity due to anisotropic diffusion in apatite during electron microprobe analysis," *American Mineralogist*, vol. 78, pp. 641–648, 1993.
[51] S. R. Levitt and R. A. Condrate, "The Polarized Infrared Spectra of Hydroxyl Ion in Fluorapatite," *Applied Spectroscopy*, pp. 288–289, 1970.
[52] J. M. Hughes, H. Nekvasil, G. Ustunisik, D. H. Lindsley, A. E. Coraor, J. Vaughn, B. L. Phillips, F. M. McCubbin, and W. R. Woerner, "Solid solution in the fluorapatite-chlorapatite binary system: High-precision crystal structure refinements of synthetic F-Cl apatite," *American Mineralogist*, vol. 99, no. 2, pp. 369–376, 2014.
[53] J. P. Yesinowski, H. Eckert, and G. R. Rossman, "Characterization of Hydrous Species in Minerals by High Speed 1H MAS-NMR," *Journal of the American Chemical Society,* no. 110, 1988.
[54] P. E. Mackie and R. A. Young, "Fluorine-Chlorine Interaction in Fluor-Chlorapatite," *Journal of Solid State Chemistry*, vol. 11, pp. 319–329, 1974.
[55] G. Schettler, M. Gottschalk, and D. E. Harlov, "A new semi-micro wet chemical method for apatite analysis and its application to the crystal chemistry of fluorapatite-chlorapatite solid solutions," *American Mineralogist*, vol. 96, no. 1, pp. 138–152, 2010.
[56] C. Rey, J. C. Trombe, and G. Montel, "Some features of the incorporation of oxygen in different oxidation states in the apatitic lattice—III Synthesis and properties of some oxygenated apatites," *Journal of Inorganic and Nuclear Chemistry*, vol. 40, no. 1, pp. 27–30, 1978.
[57] P. Alberius Henning, S. Lidin, and V. Petricek, "Iodo-oxyapatite, the first example from a new class of modulated apatites," *Acta Crystallographica,* vol. 55, no. 2, pp. 1–5, 1999.
[58] J. S. Prener, "The Growth and Crystallographic Properties of Calcium Fluor- and Chlorapatite Crystals," *Solid State Science*, pp. 77–83, 1967.
[59] K. L. Wang, Y. Zhang, and F. U. Naab, "Calibration for IR measurements of OH in apatite," *American Mineralogist*, vol. 96, no. 8, pp. 1392–1397, 2011.
[60] R. Z. LeGeros, "Calcium Phosphate-Based Osteoinductive Materials," *Chemical Reviews*, vol. 108, no. 11, pp. 4742–4753, 2008.
[61] J. S. Vaughn, W. R. Woerner, and D. H. Lindsley, "Hydrogen Environments In Low-OH, F, Cl Apatites Revealed By Double Resonance Solid-State NMR," *The Journal of Physical Chemistry C*, vol. 119, no. 51, pp. 28605–

28613, 2015.
[62] D. L. Bryce, G. M. Bernard, G. Myrlene, M. D. Lumsden, K. Eichele, and R. E. Wasylishen, “Practical Aspects of Modern Routine Solid-State Multinuclear Magnetic Resonance Spectroscopy: One-Dimensional Experiments,” *Canadian Journal of Spectroscopy*, pp. 1–40, 2004.
[63] C. P. Grey and A. J. Vega, “Determination of the Quadrupole Coupling Constant of the Invisible Aluminum Spins in Zeolite HY with 1H/27Al TRAPDOR NMR,” *Journal of the American Chemical Society,* vol. 117, no. 31, pp. 8232–8242, 1995.
[64] M. Braun and C. Jana, “^{19}F NMR spectroscopy of fluoridated apatites,” *Chemical Physics Letters*, vol. 245, no. 1, pp. 19–22, 1995.
[65] M. Braun, P. Hartmann, and C. Jana, “^{19}F and ^{31}P NMR Spectroscopy of Calcium Apatites,” *Journal of Materials Science Materials in Medicine*, vol. 6, pp. 150–154, 1995.
[66] M. D. O’Donnell, R. G. Hill, R. V. Law, and S. Fong, “Raman spectroscopy, ^{19}F and ^{31}P MAS-NMR of a series of fluorochloroapatites,” *Journal of the European Ceramic Society*, vol. 29, no. 3, pp. 377–384, 2009.
[67] F. M. McCubbin, H. E. Mason, H. Park, B. L. Phillips, J. B. Parise, H. Nekvasil, and D. H. Lindsley, “Synthesis and characterization of low-OH fluor-chlorapatite: A single-crystal XRD and NMR spectroscopic study,” *American Mineralogist*, vol. 93, no. 1, pp. 210–216, 2008.
[68] D. L. Bryce and G. D. Sward, “Solid-state NMR spectroscopy of the quadrupolar halogens: chlorine-35/37, bromine-79/81, and iodine-127,” *Magn. Reson. Chem.*, vol. 44, no. 4, pp. 409–450, 2006.
[69] J. M. Hughes, M. Cameron, and K. D. Crowley, “Crystal Structures of Natural ternary Apatites: solid solution in the $Ca_5(PO_4)_3X$ (X= F,OH,Cl),” *American Mineralogist*, vol. 75, pp. 295–304, 1990.
[70] T. J. Kiczenski and J. F. Stebbins, “Fluorine sites in calcium and barium oxyfluorides: F-19 NMR on crystalline model compounds and glasses,” *Journal of Non-Crystalline Solids*, vol. 306, no. 2, pp. 160–168, 2002.
[71] H. E. Swanson and E. Tatge, *Standard X-ray Diffraction Powder Patterns.* 1953.
[72] B. P. Sobolev, E. G. Ippolitov, and B. M. Zhigarnovskii, "Phase composition of the systems CaF_2—YF_3, SrF_2—YF_3, and BaF_2—YF_3, *Izvestiya Akademii Nauk SSSR, Neorganicheskie Materialy,* vol. 1, no. 3, pp. 362-368, 1965.
[73] L. G. Schulz, “Oriented Overgrowths of Alkali Halides on Silver Substrates,” *Acta Crystallographica*, vol. 5, no. 2, pp. 266–268, 1952.
[74] L. Kolditz, W. Wilde, and W. Hilmer, “Röntgenographische Phasenbestimmungen zur thermischen Dissoziation und das Hydrolyseverhalten von Alkalihexafluorogermanaten bei höheren Temperaturen,” *Zeitschrift für anorganische und allgemeine Chemie*, vol. 512, no. 5, pp. 48–58, 1984.
[75] W. P. Davey, “Precision measurements of crystals of the alkali halides,” *Physical Review*, vol. 21, no. 2, pp. 143-162, 1923.
[76] P. Alberius Henning, A. R. Landa-Canovas, A. K. Larsson, and S. Lidin, “Elucidation of the crystal structure of oxyapatite by high-resolution electron

microscopy," *Acta Crystallographica,* vol. B55, pp. 170-176, 1999.
[77] J. C. Trombe and G. Montel, "Some Features of the Incorporation of Oxygen in Different Oxidation States in the Apatitic Lattice - I," *Journal of Inorganic and Nuclear Chemistry*, vol. 40, pp. 15–21, 1978.
[78] C.-J. Liao and J.-S. Sun, "Thermal decomposition and reconstitution of hydroxyapatite in air atmosphere," *Biomaterials*, pp. 1–7, 1999.
[79] R. H. Jones, F. M. McCubbin, L. Dreeland, Y. Guan, P. V. Burger, and C. K. Shearer, "Phosphate minerals in LL chondrites: A record of the action of fluids during metamorphism on ordinary chondrite parent bodies," *Geochimica et Cosmochimica Acta*, vol. 132, no. C, pp. 120–140, 2014.
[80] P. M. Panchmatia, A. Orera, G. J. Rees, M. E. Smith, J. V. Hanna, P. R. Slater, and M. S. Islam, "Oxygen Defects and Novel Transport Mechanisms in Apatite Ionic Conductors: Combined ^{17}O NMR and Modeling Studies," *Angewandte Chemie International Edition*, vol. 50, no. 40, pp. 9328–9333, 2011.
[81] P. Berastegui, S. Hull, F. J. Garcı Garcı, and J. Grins, "A Structural Investigation of $La_2(GeO_4)O$ and Alkaline-Earth-Doped $La_{9.33}(GeO_4)_6O_2$," *Journal of Solid State Chemistry*, vol. 168, no. 1, pp. 294–305, 2002.
[82] S. E. Ashbrook, S. E. Ashbrook, M. E. Smith, and M. E. Smith, "Solid state ^{17}O NMR—An introduction to the background principles and applications to inorganic materials," *Chemical Society Reviews,* vol. 35, pp. 718-735, 2006.
[83] V. Lemaître, M. E. Smith, and A. Watts, "A review of oxygen-17 solid-state NMR of organic materials—towards biological applications," *Solid State Nuclear Magnetic Resonance*, vol. 26, no. 3, pp. 215–235, 2004.
[84] P. J. Grandinetti, J. H. Baltisberger, and I. Farnan, J. F. Stebbins, U. Werner, A. Pines, "Solid-state ^{17}O magic-angle and dynamic-angle spinning NMR study of the SiO_2 polymorph coesite," *The Journal of Physical Chemistry C*, vol. 99, pp. 12341-12348, 1995.
[85] K. T. Mueller, Y. Wu, and B. F. Chmelka, "High-resolution oxygen-17 NMR of solid silicates," *Journal of the American Chemical Society.* vol. 113, no. 1, pp. 32–38, 1991.
[86] H. Timken, S. E. Schramm, and R. J. Kirkpatrick, "Solid-state oxygen-17 nuclear magnetic resonance spectroscopic studies of alkaline earth metasilicates," *Journal of Physical Chemistry,*vol 91, pp 1054-1058, 1987.
[87] J. F. Stebbins and Z. Xu, "NMR evidence for excess non-bridging oxygen in an aluminosilicate glass," *Nature*, no. 390, pp. 1–4, 1997.
[88] F. Pourpoint, C. Gervais, L. Bonhomme-Coury, T. Azaïs, C. Coelho, F. Mauri, B. Alonso, F. Babonneau, and C. Bonhomme, "Calcium Phosphates and Hydroxyapatite: Solid-State NMR Experiments and First-Principles Calculations," *Applied Magnetic Resonance*, vol. 32, no. 4, pp. 435–457, 2007.
[89] Z. Lin, J. R. Jones, J. V. Hanna, and M. E. Smith, "A multinuclear solid state NMR spectroscopic study of the structural evolution of disordered calcium silicate sol–gel biomaterials," *Physical chemistry chemical physics*, vol. 17, no. 4, pp. 2540–2549, 2015.
[90] H. Kiyono, Y. Matsuda, T. Shimada, M. Ando, I. Oikawa, H. Maekawa, S.

Nakayama, S. Ohki, M. Tansho, T. Shimizu, P. Florian, and D. Massiot, "Oxygen-17 nuclear magnetic resonance measurements on apatite-type lanthanum silicate ($La_{9.33}(SiO_4)_6O_2$)," *Solid State Ionics*, vol. 228, pp. 64–69, 2012.

[91] A. C. Larson and R. B. Von Dreele, "GSAS - General Structure Analysis System" LAUR 86-748, Dec. 2000.

[92] M. Yashima, A. Sakai, T. Kamiyama, and A. Hoshikawa, "Crystal structure analysis of β-tricalcium phosphate Ca3(PO4)2 by neutron powder diffraction," *Journal of Solid State Chemistry*, vol. 175, no. 2, pp. 272–277, 2003.

[93] J. L. Palumbo, L. Peng, T. A. Schaedler, C. G. Levi, C. P. Grey, and C. P. Grey, "^{17}O NMR studies of local structure and phase evolution for materials in the $Y_2Ti_2O_7$–$ZrTiO_4$ binary system," *Journal of Solid State Chemistry*, vol. 180, no. 7, pp. 2175–2185, 2007.

[94] H. R. X. Pimentel, D. L. M. Aguiar, R. A. S. San Gil, A. R. Ferreira, E. F. Souza, R. B. Alencastro, A. A. Leitão, S. M. C. Menezes, and S. S. X. Chiaro, "^{17}O MAS NMR and first principles calculations of ZrO_2 polymorphs," *Chemical Physics Letters*, vol. 555, pp. 96–100, 2013.

[95] X. Marchandise, P. Belgrand, and A. P. Legrand, "Solid State ^{31}P NMR Spectroscopy of Bone and Bone Substitutes," *Magnetic Resonance in Medicine*, vol. 28, p. 1, 1992.

[96] M. J. Duer, "The contribution of solid-state NMR spectroscopy to understanding biomineralization: Atomic and molecular structure of bone," *Journal of Magnetic Resonance*, vol. 253, no. C, pp. 98–110, 2015.